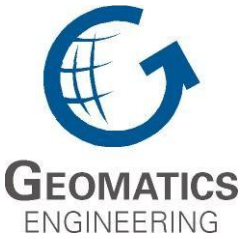

UCGE Reports
Number 20363

Department of Geomatics Engineering

Second Generation Multi-Resolution Techniques for Edge Detection and Feature Extraction from 8-Bands High Resolution Satellite Imagery

(URL: http://www.geomatics.ucalgary.ca/graduatetheses)

by

AHMED SHAWKY KHALIL ELSHARKAWY

November, 2012

UNIVERSITY OF CALGARY

Second Generation Multi-Resolution Techniques for Edge Detection and Feature Extraction from 8-Bands High Resolution Satellite Imagery

by

AHMED SHAWKY KHALIL ELSHARKAWY

A THESIS

SUBMITTED TO THE FACULTY OF GRADUATE STUDIES

IN PARTIAL FULFILMENT OF THE REQUIREMENTS FOR THE

DEGREE OF DOCTOR OF PHILOSOPHY

Department of Geomatics Engineering

CALGARY, ALBERTA

November, 2012

Abstract

Urban mapping is one of the most important tasks in military and civilian applications. Since the launching of high resolution satellite imagery; such as IKONOS, QUICKBIRD, WorldView-2 and their high spatial and high spectral resolution are much appreciated for urban mapping, as high spatial resolution provides better geometric quality while high spectral resolution provides better object identification. If we add the reliability and unmatched coverage area, compared to other sensors, with the previous advantages so we are using the optimum tool for urban planning and mapping purposes.

Current scientific efforts in image and signal processing fields have led to more powerful and reliable tools for fast and efficient analysis and handling of large amounts of data sets currently available from the new satellite missions. This thesis contributes to this development by introducing an innovative combination of various methods from image processing and the new eight bands from the WorldView-2 to derive reliable information for land use and land cover types.

In this thesis, data from WorldView-2 satellite for Ismailia city, EGYPT, is used. The study area was selected to cover the main necessary classes to produce an urban classification map. A new multi-layer classification algorithm using the traditional NDVI and two new NDVI like ratio were used to separate between six main classes; water, vegetation, shadow, bare soil, asphalt and buildings.

A new technique based on second generation curvelet transforms was used to detect edges and was compared with wavelet and traditional canny operator. Both approaches; the multi-layer classification algorithm and curvelet transforms, were integrated to enhance the quality of the classification. A calibration process preceded the proposed algorithms and succeeded together in

extracting the desired classes with a high accuracy in an almost automatic procedure without user intervention.

Shorelines were also extracted using the new algorithm and the relative bathymetry of the water way of the Suez Canal and the Temsah Lake were derived using innovated band ratios with the new spectral bands.

Acknowledgements

Praise is to Allah, the Almighty, on whom ultimately we depend for sustenance and guidance.

First and foremost, I would like to thank my supervisor Dr. Naser El-Sheimy for the valuable guidance and advice. Dr. El-Sheimy inspired me greatly to work in this thesis. His willingness to motivate me contributed tremendously to this work. I appreciate his professional supervision, strong support, guidance and abundant cooperation. Really, I was honored to work under his supervision.

I wish to express my gratitude to Dr. Mohamed Elhabiby, who was abundantly helpful and offered invaluable assistance, support, valuable discussions, constructive suggestions and guidance. This research would not have been possible without the support of Dr. Elhabiby.

I would like to extend my appreciation to my supervising committee Dr. Ayman Habib for his professional teaching and valuable discussion. He was always there for help and assistance.

I would like to thank all my friends in the Mobile Mapping Sensor System research group for their wonderful friendship, support and valuable discussion: Adel Moussa, Mohamed Attia, Abd Elrahman Ali, Ahmed El-Ghazouly, Mazen El-sadat, Naief, Hussien, Kelly, Sara, Siddharth, Dr. Yigiter. It was my pleasure to work with them in this wonderful working environment.

I can’t find words to express my gratitude to my MTC colleagues, Dr. Hassan Elhifnawy, Dr. Ahmed Mohsen, Dr. Walid Elthalabawy, Bassem Sheta and Essam Hamza for their wonderful friend ship and great time we spent together with ourselves and with our families, I really enjoyed each and every moment.

I also give a great thanks to my wife Hend, my son Mohamed and my two daughters Nariman and Nouran. You are the best thing happen in my life, may ALLAH bless you all.

Dear mother (may ALLAH bless your soul), Dear father, it is all because of your prayers. Please keep praying for me. I love you and thank you for everything.

Dear brothers, Mohamed and Wael thanks for your support, encouragement and help along the way.

Finally I would like thank my country, Egypt, for funding and supporting my research, specially the Egyptian Armed Forces, my sponsor, for the unwavering support. I also would like to thank my supervisor Dr. Naser El-Sheimy for the additional funding from his Canada Research Chair and TECTERRA funding.

Dedication

To My Beloved Family
My father,
My Brothers,
My Wife, My Son and My Daughters

(Thank You So Much)

Table of Contents

List of Tables

List of Figures and Illustrations

List of Symbols, Abbreviations and Nomenclature

**	Convolution Operation
$\tilde{V}_j(\omega)$	Cartesian Angular window in the frequency domain
$\widetilde{W}_j(\omega)$	Cartesian Radial window in the frequency domain
$\hat{f}_m$	Image function approximated by largest *m* coefficients
$E_{sun\lambda_{band}}$	WorldView-2 Band-Averaged Solar Spectral Irradiance
K_{band}	The absolute radiometric calibration factor
$L_{\lambda_{pixel,band}}$	Top-of-atmosphere spectral radiance image pixels
$\widetilde{U}$	Cartesian Window
$q_{pixel,band}$	The given radiometrically corrected image pixels
θ_s	The average solar zenith angle
$\rho_{\lambda_{pixel,band}}$	The ToA reflectance values
$\nabla I_{x,y}$	Magnitude of the gradient in x,y direction
µm	Micrometer
2D FDCT	2-D Fast Discrete Curvelet Transforms
A_d	The upwelling spectral radiance
AU	Astronomical Units
B	Blue band
BPF	Band-pass filter
BRDF	Bi-directional reflectance distribution function
C	Coastal Blue band
C_i	The covariance matrix of signature i

CZMIL	Coastal zone mapping and imaging LiDAR
D	Diagonal detail image in wavelet decomposition operation
DCTG2	Second Generation Discrete Curvelet Transforms
DEM	Digital Elevation Model
d_{ES}	Earth-Sun distance
D_{ij}	Divergence value
DN	Digital Number
DWT	Discrete Wavelet Transforms
E(m,n)	Object-based classification results.
$F(k_x,k_y)$ and $H(k_x,k_y)$	Fourier transforms of the 2-D functions
f(m,n)	Final classification results.
$f(x,y)$ and $h(x,y)$	Two 2-D functions
FFT	Fast Fourier Transforms
FT	Fourier transforms
FWHM	Full Width at Half Maximum
G	Green band
$G(x,y)$	2-D Isotropic Gaussian equation
GIS	Geographic Information System
GMT	Greenwich Mean Time
H	Horizontal detail image in wavelet decomposition operation
HBF	High-Boost filter
HPF	High-Pass filter
j	Radial variable represents the scale

k	Translation parameter
l	Angular variable represents the direction
$L(\lambda_i)$	The remote sensing radiance after atmospheric and sun-glint corrections for spectral band λ_i
L_∞	Deep water radiance
LADS	Laser Airborne Depth Sounder.
L_b	The bottom radiance.
LiDAR	Light Detection And Ranging
LL	Approximation image in wavelet decomposition operation
L_p	Atmospheric path radiance.
LPF	Low-Pass filter
L_s	Specular radiance.
L_t	The total upwelling radiance.
L_v	Subsurface volumetric radiance.
m_0, m_1	The interception and slope values for Sumpf model respectively
m^{-2}	Per Unit area
MLC	Maximum Likelihood Classification
n	Number of scales
N	The largest number of pixels in column/row in an image
NDVI	Normalized Difference Vegetation Index
NIR1	Near-infrared 1 band
NIR2	Near-infrared 2 band
OIF	Optimum Index Factor

$p(m,n)$	The pixel-based classification results.
$p(x)$	The probability of finding a pixel from any class at location x
$p(\omega_i)$	The probability that class ω_i occurs in the image and also called *a priori* or prior probabilities
$p(\omega_i\|x)$	The probability of the correct class ω_i for a certain pixel at location x.
PAN	Panchromatic band
PCA	Principal Component Analysis
PIF	Pseudo Invariant Features
R	Red band
R^2	Confidence level
R-E	Red Edge Band
r_j	Correlation coefficient between any two bands
RVI	Ratio Vegetation Index
S/N	Signal-to-noise ratio
S_k	Standard deviation of band-k
sr^{-1}	Steradian is the SI unit of solid angle
SRRVI	Square Root of Ratio Vegetation Index
SWIR	Short-Wave Infrared
Symbol	Definition
T	The transposition function
TD_{ij}	The transformed divergence
TH and TL	Canny operator high and low thresholds
ToA	Top of Atmosphere

tr	The trace function (matrix algebra)
U_j	Polar wedge window
USFFT	Unequally Spaced Fast Fourier Transform
USGS	United States Geological Survey
UV	Ultra violet
V	Vertical detail image in wavelet decomposition operation
V(t)	Angular window in the frequency domain
VNIR	Visible and near-infrared bands
W	Radiant energy per unit time, also called radiant power.
W(r)	Radial window in the frequency domain
WQI	Water quality index
Y	Yellow band
z	Absolute bathymetric depth
$\Delta\lambda_{band}$	The effective bandwidth [μm] for a given band
μ_i	The mean vector of signature *i*
ρ_{nir} and ρ_{red}	Reflectance values in near-infrared and red bands
$C(i,j,k)$	Discrete Curvelet Coefficient at certain scale and orientation.
JD	Julian day
UT	Universal Time
$sunEL$	Average sun elevation angle

Chapter One: **Introduction**

For many years, satellite-based remote sensing has been a highly invaluable tool for urban planning as no other platform can reliably and repeatedly revisits an area on such a broad scale. Generally, satellite-based remote sensing can be considered a cost-effective alternative to aerial photography or LiDAR, especially in the acquisition of land cover and land use information (Ouma et al. 2010).

Since the launching of many high resolution satellite imagery in the first decade of this century, remote sensing has undergone a rapid development, boosting the possibility of many new and improved applications (Ünsalan and Boyer 2011). Ongoing scientific efforts in image and signal processing fields have led to more powerful and reliable tools for fast and efficient analysis and handling of large amounts of data currently available from new satellite missions.

This thesis contributes to this development, by introducing an innovative combination of various methods from image processing and the new eight bands from the WorldView-2 to derive reliable information for land use and land cover types.

1.1 Motivation

Recent advances in satellite imagery have resulted in the availability of high-resolution multispectral imagery with, meter and sub meter resolution. Before WorldView-2, high spatial resolution images were usually of low spectral resolution, typically containing only three or four spectral data bands, red, green, blue and infrared, as in the case of IKONOS or Quickbird. This shortage of mid-infrared bands limit the ability of traditional classifiers to accurately detect detailed land-cover types (Thomas et al. 2003). Geo-Eye-1 is considered the most comparable satellite to WorldView-2 in the spatial details perspective because it provides sub-meter accuracy for the panchromatic sensor and 1.65 m for the multispectral sensor. However, in terms of its

spectral resolution, its capabilities remain far from those of the WorldView-2 since it only provides four spectral bands like IKONOS and Quickbird imagery. Although medium resolution satellites such as Landsat Thematic Mapper introduced eight spectral bands ranging from the visible to infra-red, and also include two thermal bands, they did not provide the required spatial details necessary for many urban planning applications. Additionally, automated image classification techniques relied entirely on the pixel characteristics such as the digital number or colour, leaving behind key characteristics of texture, shape and context (Sharma and Sarkar 1998).

The previous limitation could be accepted in low or medium resolution satellite imagery as the pixel is relatively large and already contains texture information. However, in high-resolution satellite imagery, the pixel is relatively small and the texture information occurring in the relationship between pixels is quite meaningful. Therefore, the use of a pixel-approach alone for classification is not enough, and the use of contextual information in addition to spectral features for image classification will result in an improved level of accuracy (Ouma et al. 2010)

The main objective of this research thesis is to introduce a mapping solution for urban, agricultural, marine classification, and coastal edge detection including shallow water depth estimation using the enhanced capability of the new satellite mission, WorldView-2. Achieving this objective first requires the application of supervised classification techniques through Maximum Likelihood Classification (MLC). In addition, some traditional and innovative band ratios are used in a decision tree to evaluate the contribution of each of the new bands into the quality of classification. Then as a new technique, the second generation curvelet transform (DCTG2) is applied for edge detection of coastal lines, buildings, and road networks and compared to the traditional edge detectors such as Canny edge detector and wavelet transform.

Finally, the two approaches are combined to produce an efficient urban and coastal classification technique that can be later used in change detection or any further process.

1.2 Thesis Objectives

The main objective of this study is to introduce a classification and edge detection solution for classifying urban, vegetation, desert and coastal areas utilizing second-generation multi-resolution techniques combined with traditional edge detection operators and the enhanced capability of the new satellite mission WorldView-2.

The workflow is summarized in Figure 1-1, first, supervised classification techniques are applied by maximum likelihood classification (MLC) and parallelepiped methods using innovative band ratios that are combined to introduce an efficient classification and identification technique with a detailed evaluation that tests the quality of the resulting classification. Next, the second generation curvelet transform (DCTG2) will be implemented for edge detection of different features and regions, mainly coastal lines, buildings and road networks which will then be compared to the traditional edge detectors results such as Canny edge detector and discrete wavelet transform (DWT). A comparison between the application of a curvelet transform as a standalone technique or a combination with Canny is developed to achieve the most efficient combination of the three techniques for edge detection.

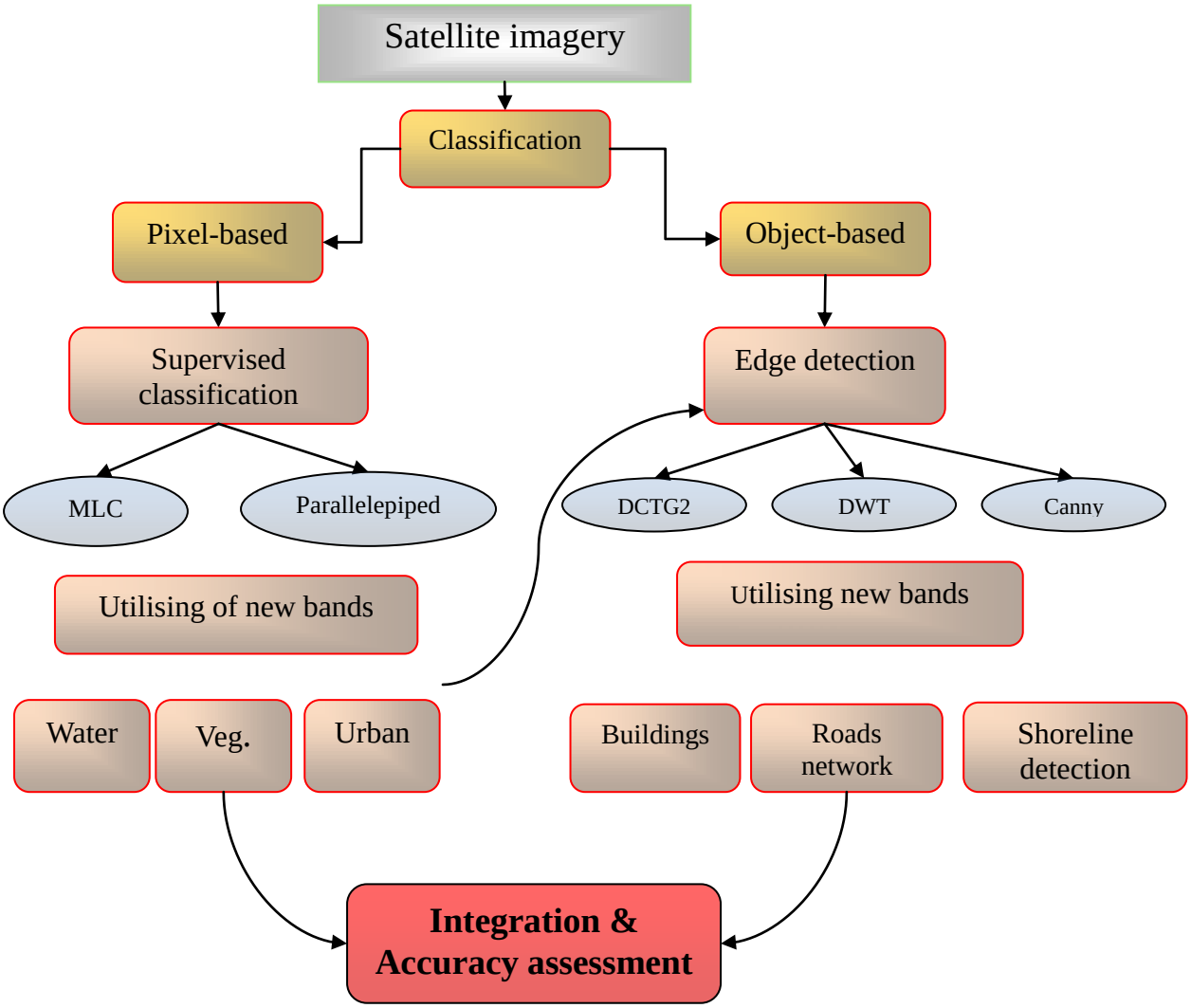

Figure 1-1 Research Workflow

This thesis also includes the following sub-objectives that will contribute to the achievement of the main objective:

- Validating of the improvement in classification accuracy attributable to the new spectral bands versus the traditional visible and near-infrared (VNIR) bands used for a broad range of land cover types, by implementing only traditional spectral classifiers and without using any textural information.

- Developing of a detailed assessment of the predictive role of each of the new bands, coastal-blue (C), yellow (Y), red edge (R-E) and near-infrared 2 (NIR2), with a quality assessment and an analysis of their contribution to the classification process.
- Developing new band ratios specially designed to detect shadow, bright surface and asphalt.
- Modifying the parallelepiped method and solving some of its drawbacks and disadvantages (misclassified and overlapped pixels) without affecting its simplicity and minimum calculation time.
- Implementing second-generation curvelet transforms as an edge detector of shorelines and buildings with the aid of the 8-bands and assessing its efficiency in comparison to the traditional first generation multi-resolution analysis techniques.
- Assessing the accuracy of edge detection using DCTG2, compared to the accuracy obtained from classical techniques (Canny and wavelet transformation) regarding building and shorelines extraction.
- Methodology to incorporate spatial and spectral approaches to enhance classification quality.
- Estimating the bathymetry of shallow water through the use of red edge (R-E) and coastal-blue (C) bands respectively.

1.3 Thesis Outlines

The thesis consists of six chapters; chapter two covers the necessary background about image spectrometry and the behaviour of the main four features, water, vegetation, manmade objects

and barren, on the earth surfaces when it is subjected to light. Also, chapter two describes the data used and the required pre-processing and data handling steps.

Chapter three deals with the implementation of three edge detection techniques; wavelet, canny and curvelet transforms, and why the conversion from spatial to frequency domain is recommended. In this chapter a detailed comparison between the three techniques and their implementation with high resolution satellite imagery were introduced in addition to the new method (curvelet - canny approach) for edge detection.

Chapter four covers the techniques used for urban classification in both approaches pixel and object bases separately. A new multi-layer classification algorithm is introduced to effectively separate between six main classes; water, vegetation, shadow, bare soil, buildings and asphalt. Second generation curvelet transforms will be implemented for edge detection to enhance the classification results especially for the buildings class. Then the integration process between the two approaches takes place.

Chapter five deals with the shoreline extraction and bathymetry problems. First curvelet transforms with the new band ratios are introduced to separate shorelines. Then, the new bands; coastal blue, yellow, near-infrared 2 and red edge will be used to extract the relative depths of the water way of the Suez Canal and the Temsah lake. Figure 1-2, illustrates the thesis outlines and the purpose of each chapter. Finally, chapter six includes the conclusion, recommendations and future work.

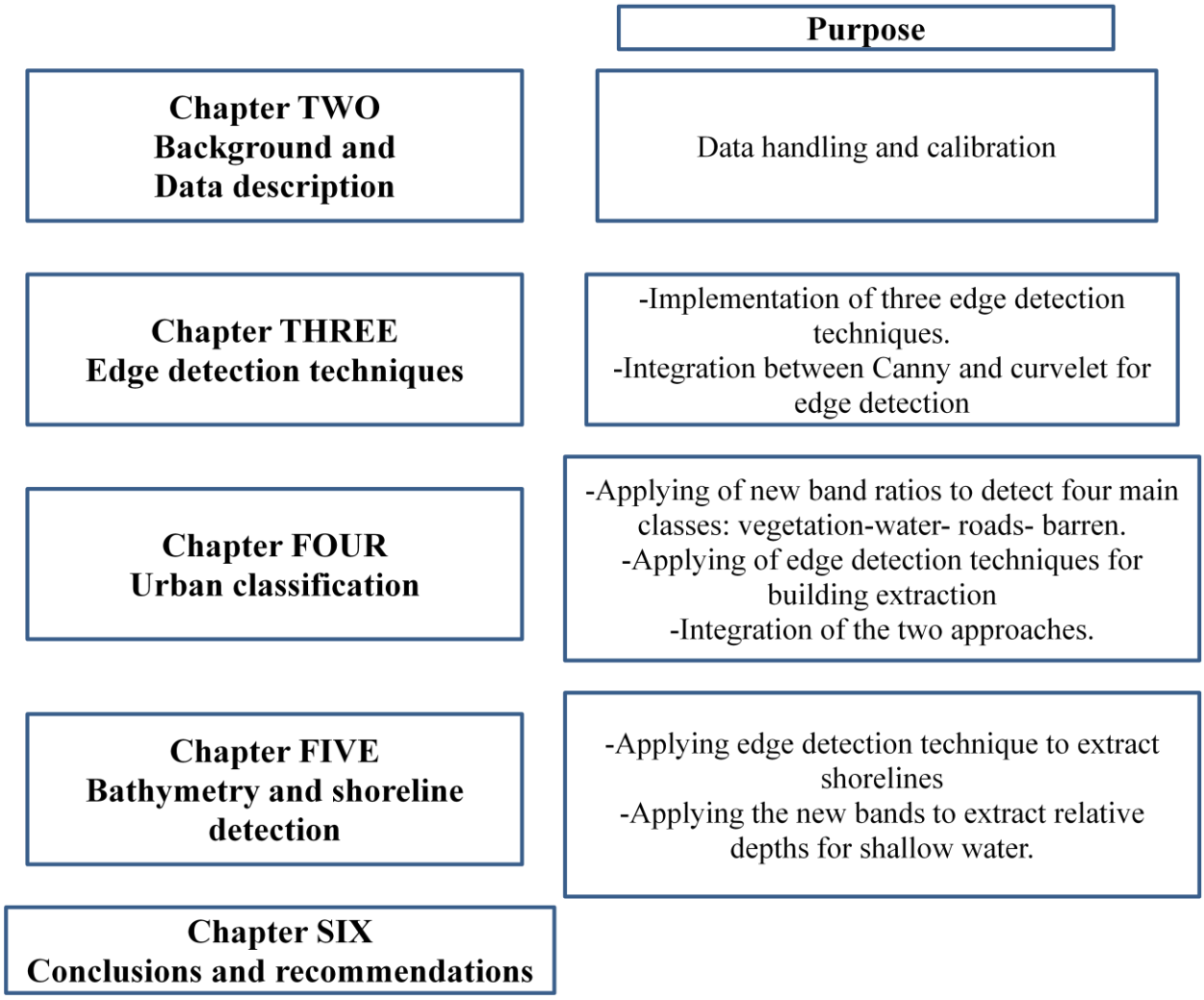

Figure 1-2 Thesis outlines

Chapter Two: **Multi-spectral Image Processing and Feature Extraction**

2.1 Imaging Spectrometry

Spectral reflectance in visible and near-infrared offers a rapid and inexpensive technique for determining the physical properties of samples and obtaining information on their chemical composition. *Spectroscopy is the study of light as a function of wavelength that has been emitted, reflected or scattered from a solid, liquid, or gas* (Clark 1999). This concept will be discussed in this chapter for four main objects; water, vegetation, soil, man-made objects. Although it is quite difficult to cover this topic adequately in a single chapter, a reasonable effort has been done to introduce an exhaustive and complete overview.

2.1.1 Absorption and Scattering

When light interacts with an object on the ground, light of certain wavelengths may be absorbed or transmitted through the substance while at other wavelengths, it may be reflected or refracted (scattered) as in Figure 2-1. The scattered portion may be scattered away from the surface, so they may or may not be detected and measured by the sensor. Reflectance may be defined as the ratio of the intensity of light reflected from an object to the intensity of the light incident on it. This light beam interacts with the object and the intensity of the reflected light at various wavelengths is measured by a detector. This detector is usually calibrated to a reference standard (surface) of known reflectance, enabling a continuous reflectance spectrum of the detected object in the measured wavelength region (Meer 2001).

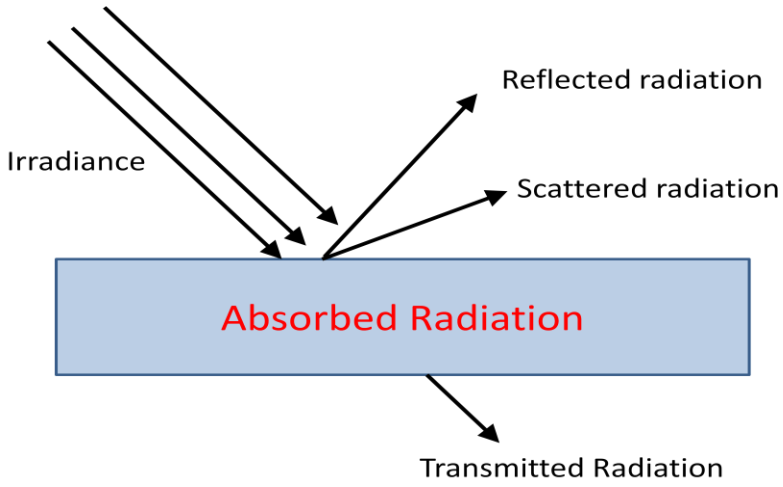

Figure 2-1 Forms of light interactions with objects

Photons (light) interact with objects by several processes. The variety of absorption processes and their wavelength dependence allows us to derive information about this feature from its reflected or emitted light. Our eyes and brain can be considered as a natural reflectance spectrometer where the wavelength-dependent scattering of visible-light photons are processed to reveal some information about what we are observing, like the red color of hematite or the green color of leaves. However, current spectrometers can measure finer details over a wider wavelength range and with greater precision (Clark 1999).

Before we go through the interaction of light with the four objects on the ground; water, vegetation, soil, man-made objects, we will give a brief explanation for some of spectrometry terms.

2.1.2 Spectroscopy Terms

Generally, to describe the capability of a spectrometer, 4 parameters are used:

- Spectral range,
- Spectral bandwidth,

- Spectral sampling,
- Signal-to-noise ratio (S/N).

Spectral range is an important index to describe the spectral absorption characteristics. According to the Canada Centre for Remote Sensing, (CCRS 2012), there are four spectral ranges that are in common use, a) ultraviolet (UV): 0.001 to 0.4 µm, b) visible: 0.4 to 0.7 µm, c) infrared : 0.7 µm to 100 µm ; and e) microwaves : 1mm to 1m. These ranges are illustrated in Figure 2-2.

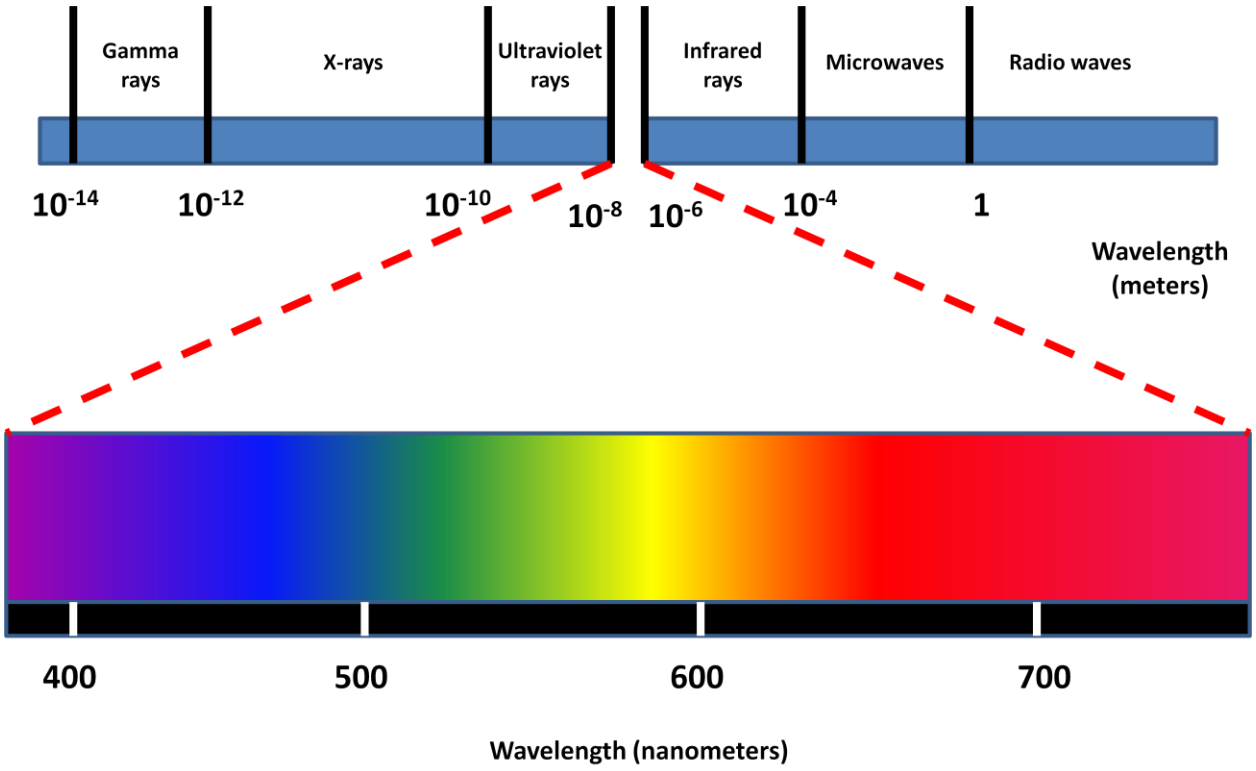

Figure 2-2 Different spectral ranges, after (CCRS 2012)

Spectral bandwidth is the width of an individual spectral channel in the spectrometer. The narrower the spectral bandwidth, the narrower the absorption feature the spectrometer will accurately measure. Figure 2-3 shows the spectra for the mineral alunite, sample HS295.3B from the USGS spectral library (Clark 1999), that could be obtained by different spectrometer

systems; each spectrum is offset upward 0.6 units from the one below it for clarity. Notice the increase of the level of details with the decrease of the spectral band width. Generally, bandwidths and sampling greater than 25 nm rapidly lose the ability to resolve important mineral absorption features (Meer 2001).

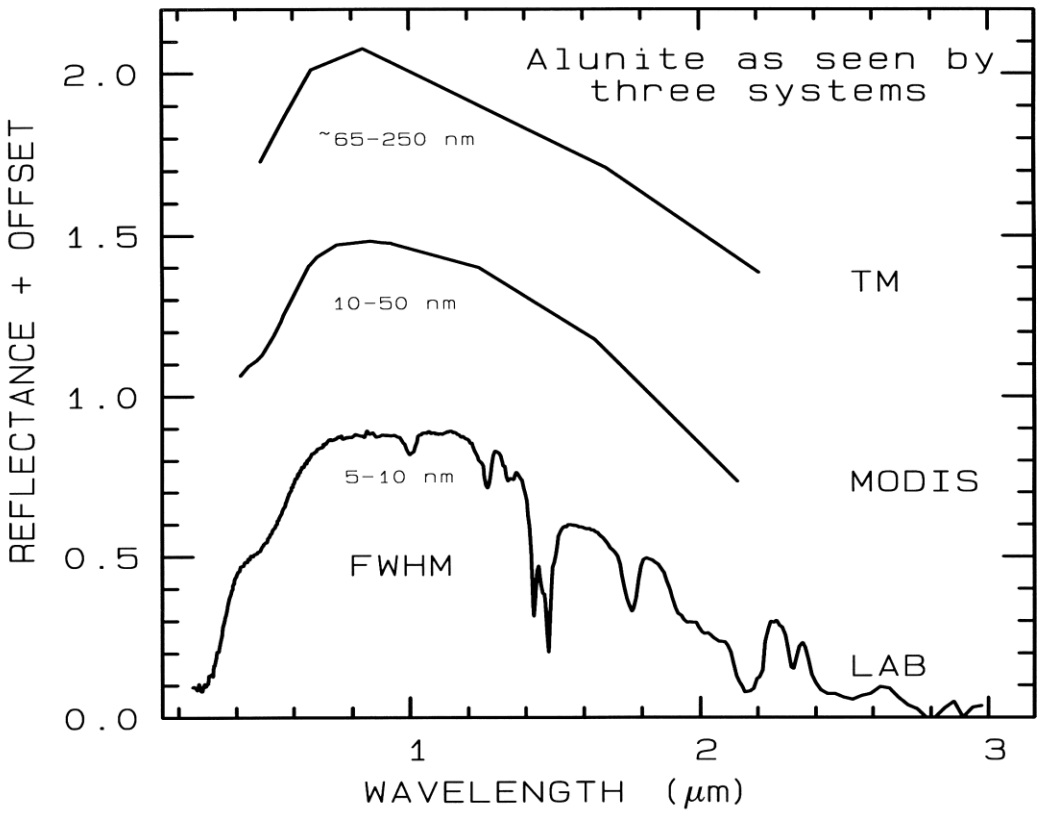

Figure 2-3 Alunite spectra as seen by three different systems (Clark 1999)

Note that the FWHM is the Full Width at Half Maximum, defined in Figure 2-4.

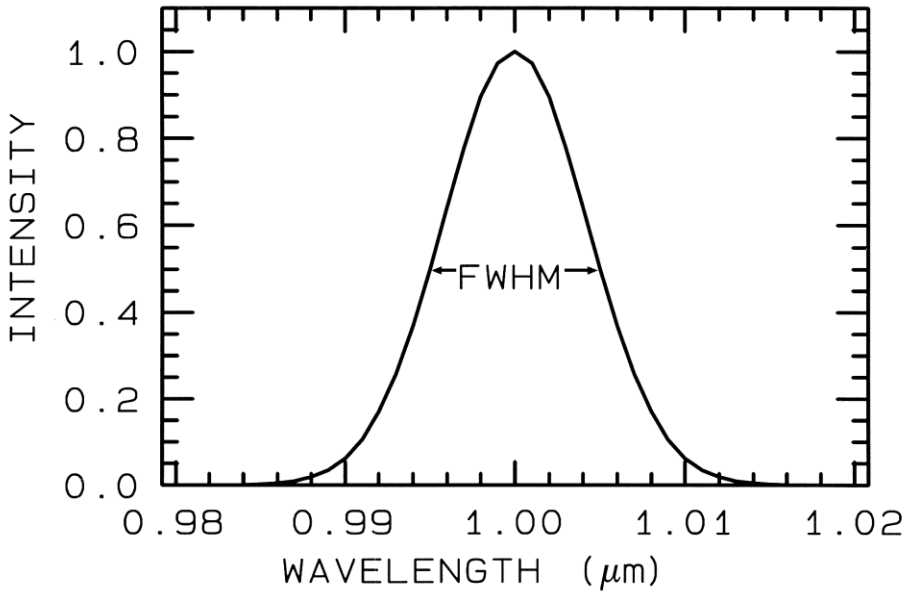

Figure 2-4 A Gaussian profile with a Full Width at Half Maximum (FWHM) of 10 nm (Clark 1999)

Spectral sampling is the distance in wavelength between the spectral band pass profiles for each channel in the spectrometer as a function of wavelength (Clark 1999).

Figure 2-5 illustrates different types of spectral sampling in spectrometers. **Nyquist's sampling** occurs when the band pass (BP) is double the sampling interval (SI), then, **Critical sampling** occurs when the BP and the SI are comparable. **Detector limited critical sampling** occurs when the optical response bandwidth is narrower than the spectral width of the detectors resulting in flat-topped band passes. Finally, **under sampling** occurs when the BP is less than the SI. The implication in under sampling is that light is being wasted between adjacent spectral channels. The spectrometer BP is the convolution of the optical response bandwidth and the spectral width of a detector (Swayze et al. 2003).

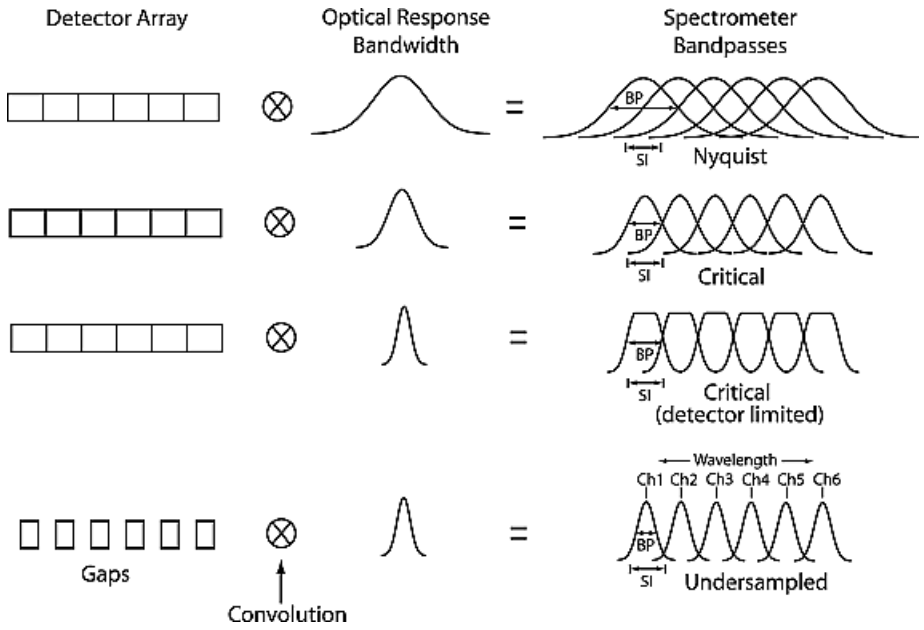

Figure 2-5 Different types of spectral sampling in spectrometers (Swayze et al. 2003)

Signal-to-noise ratio, (S/N) is dependent on the detector sensitivity, the spectral bandwidth, and intensity of the light reflected or emitted from the surface being measured. This parameter is usually required to determine the strength of the spectral response of features under study. A S/N ratio of about 10 will be adequate to identify an object, the higher (several hundred), are often required for better feature identification.

2.2 Spectral Reflectance of various features

2.2.1 Spectral Reflectance of vegetation

Generally, the studies of vegetation reflectance are limited to the green leaf part of the plants giving little consideration to the non-green dry vegetation components (Meer 2001). The chlorophyll, chemical compound in leaves, strongly absorbs radiation in the red and blue wavelengths but reflects green wavelengths. When chlorophyll content is at its maximum level, in summer, leaves appear greener than any other season. While, in autumn, the chlorophyll level decreases, so less absorption and proportionately more reflection of the red wavelengths occurs,

making the leaves appear red or yellow (CCRS 2012). This is why the best false-color combination for emphasizing the presence of vegetation must include the near-infrared band, usually in place of the red band. In fact, measuring and monitoring the near-infrared reflectance is one way to determine how healthy or unhealthy vegetation may be. The spectral responses of healthy vegetation pixels were staked, Figure 2-6, over a small agriculture parcel in the area of study, the different colors of the broken lines signifies different pixels spectral curves. The horizontal axis represents the wavelength in micrometer and the vertical axis represents the reflectance value.

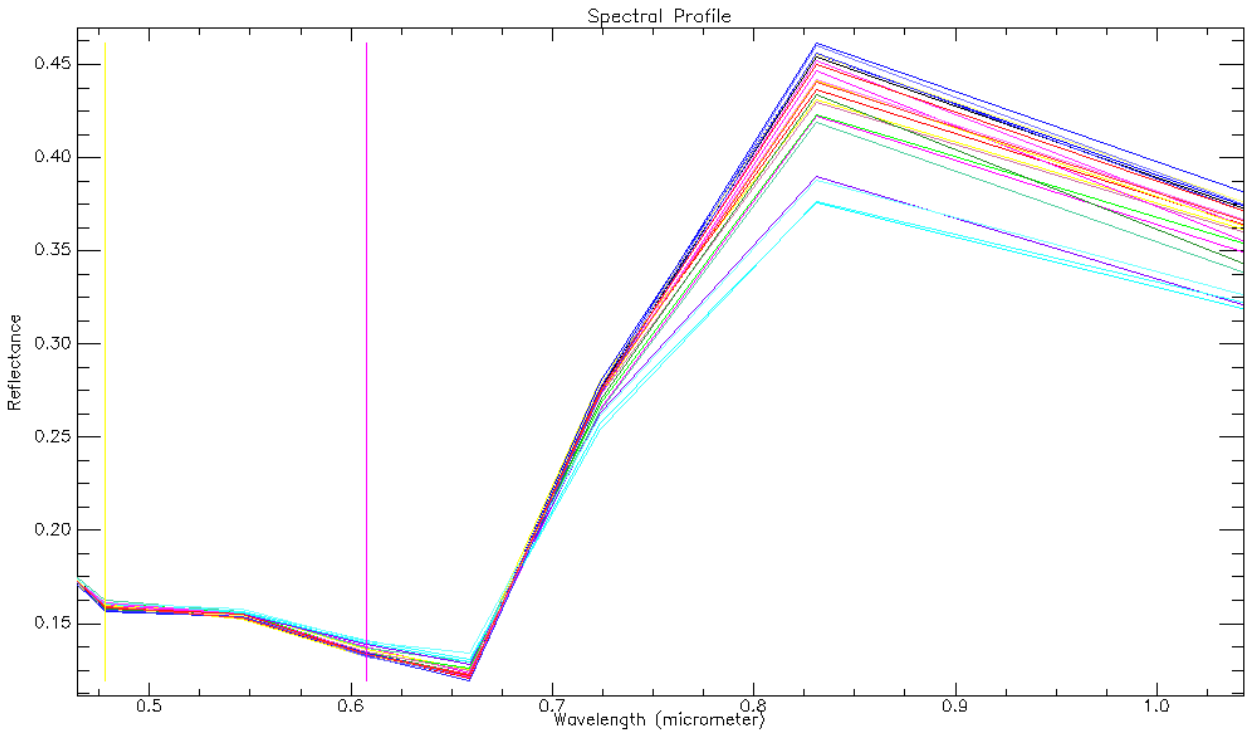

Figure 2-6 Characteristics of the Spectral response of green vegetation

Vegetation indices are ratios of single-band or linear combined reflectance their purpose is to minimize the effect of factors like optical properties of the soil background, illumination and variation of sensor-earth-sun geometry as well as wind, cloud and haze effect. The vegetation

index must be sensitive to the green part and not to the soil. Generally, Ratio-based vegetation indices can be computed from radiance values instead of reflectance values, if radiances are measured in the same irradiance conditions (Hoffer 1978).

The red band, which is related to the chlorophyll light absorption, Figure 2-6, and the near-infrared one, which is related to the green vegetation density, are the most used spectral bands to calculate vegetation indices, because these bands contain more than 90% of the information on a plant canopy. Also, in red and near-infrared bands, the contrast between vegetation and soil is maximal. In the next sections, examples will be given to some of the vegetation indices.

2.2.2 Spectral Reflectance of Soil

Spectral reflectance characteristics of soils are largely affected by the compositional nature of soils in which main components are inorganic solids, organic matter, air and water. As a result of this compound nature, the spectral reflectance also inhibits the same complexity with the varying of their physical and chemical properties (Meer 2001). Due to the electronic transition of the iron, the visible and near-infrared is the main part of the spectrum in which the main features of soil are characterized. The characteristics of soil reflectance can be summarized in the following points:

- The majority of absorption features diagnostic for mineral composition occurs in the short-wave infrared (SWIR) portion of the wavelength spectrum ranging from 2.0 to 2.5 μm.
- Layered silicates such as clays and micas and also of carbonates absorption occur in the SWIR region.
- Organic matter has a vital influence on the spectral reflectance properties of soils, where amounts exceeding 2% will cause reducing of the overall reflectivity of the soil, due to

masking effect, and reducing (and sometimes completely obscuring) the diagnostic absorption features (Meer 2001). Thus, soils with a high amount of organics appear dark throughout the 0.4 to 2.5 μm range.

- Less decomposed soils have higher reflectance in the near-infrared region and enhanced absorption features.
- Major absorption features near 1.4 and 1.9 μm due to bound and unbound water are typical for soil reflectance.
- Less water absorption features can be found at 0.97, 1.20 and 1.77 μm.
- Increasing moisture content generally decreases the overall reflectance of the soil.
- Similar effect results from increasing the particle size resulting in a decrease in reflectivity and contrast between absorption features (Meer 2001).

Some studies on the spectral reflectance characteristics of soils and attempts to make classifications can be found in (Condit 1970; Stoner and Baumgardner 1981; Baumgardner et al. 1985; Irons et al. 1989; Singh and A 1994). Following the same procedure as in Figure 2-6, a small parcel in the area of study was chosen, the different colors of the broken lines signifies different pixels spectral curves. The horizontal axis represents the wavelength in micrometer and the vertical axis represents the reflectance value, Figure 2-7.

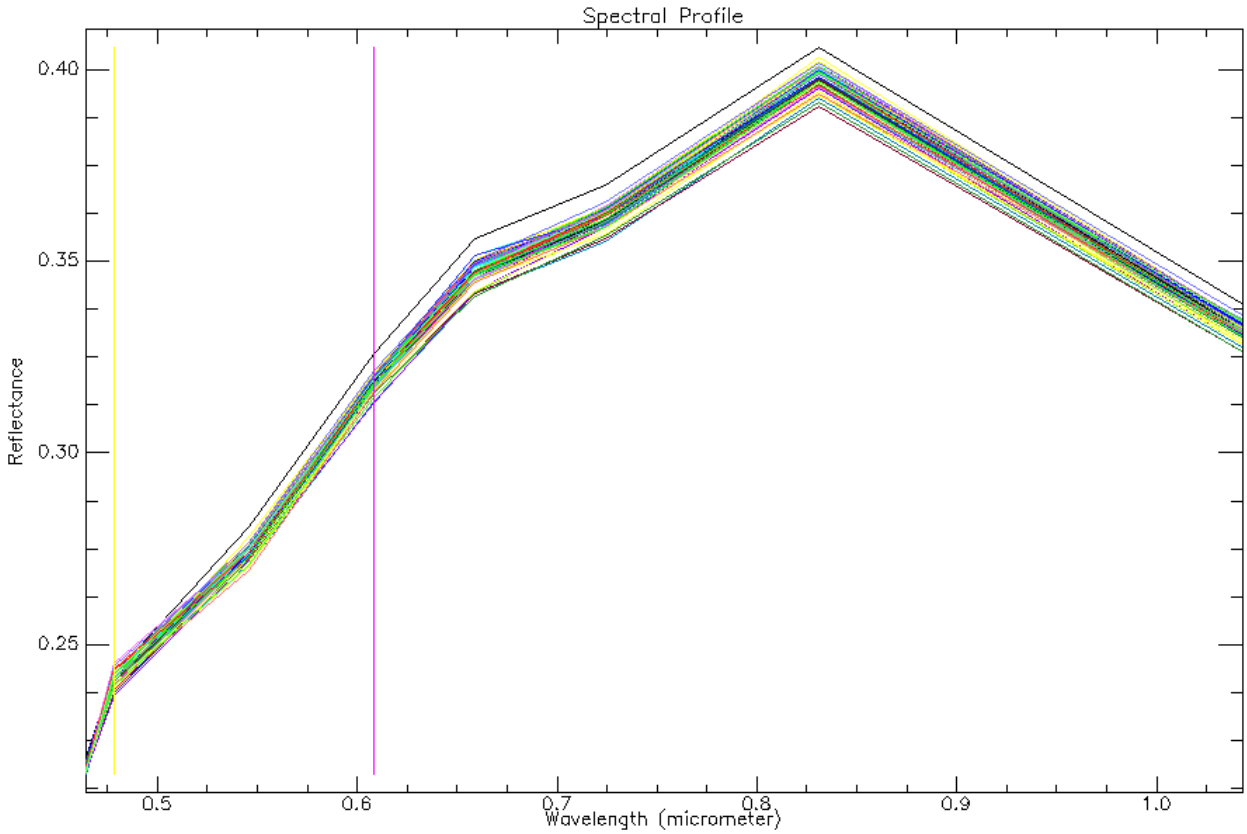

Figure 2-7 Reflectance spectra of soils

2.2.3 Spectral Reflectance of Water

Water absorbs longer wavelength, green, red and near-infrared radiation, more than shorter visible wavelengths, blue and coastal blue. This is why water typically looks blue or blue-green in a natural color image, due to a stronger reflectance at these shorter wavelengths, and darker if viewed at red or near-infrared wavelengths. However, suspended sediment, in the upper layers of water body causes increased reflectance in the visible portion of the spectrum (CCRS 2012). Figure 2-8 illustrates the spectral response of a collection of water pixels.

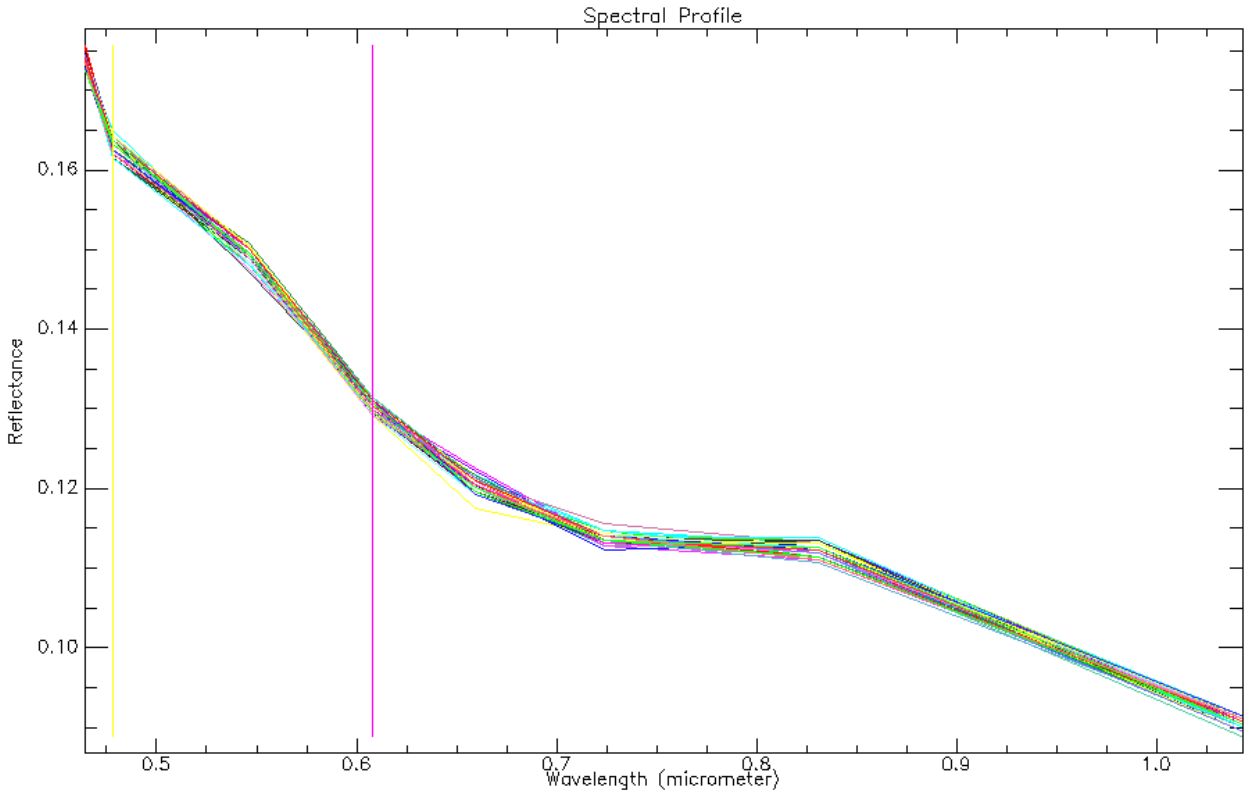

Figure 2-8 Spectral response of a collection of water pixels

Figure 2-9 represents the superposition of typical reflectance curves for the three aforementioned features, soil, vegetation and water.

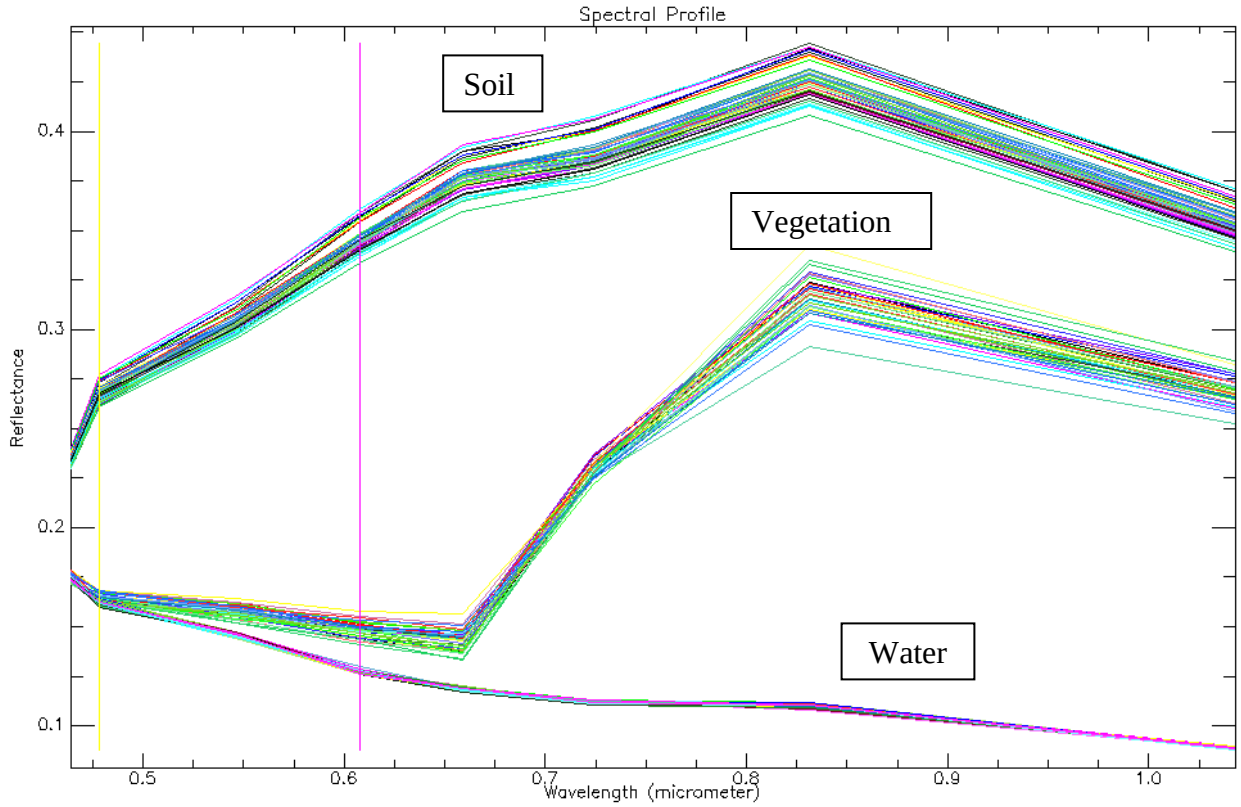

Figure 2-9 Typical reflectance curves for soil, vegetation and water

2.2.4 Spectral Reflectance of Man-made Objects

Being aware of the physical nature of different materials covering the earth surface is a prerequisite to thoroughly understand the various spectral reflectance's of man-made objects. In the following sections two main man-made objects will be targeted, asphalt and concrete, as they are the main constituent for many of well-known features; road network, buildings, rooftops, and parking lots. Figure 2-10 illustrates the spectral response for concrete, red roofs and asphalt.

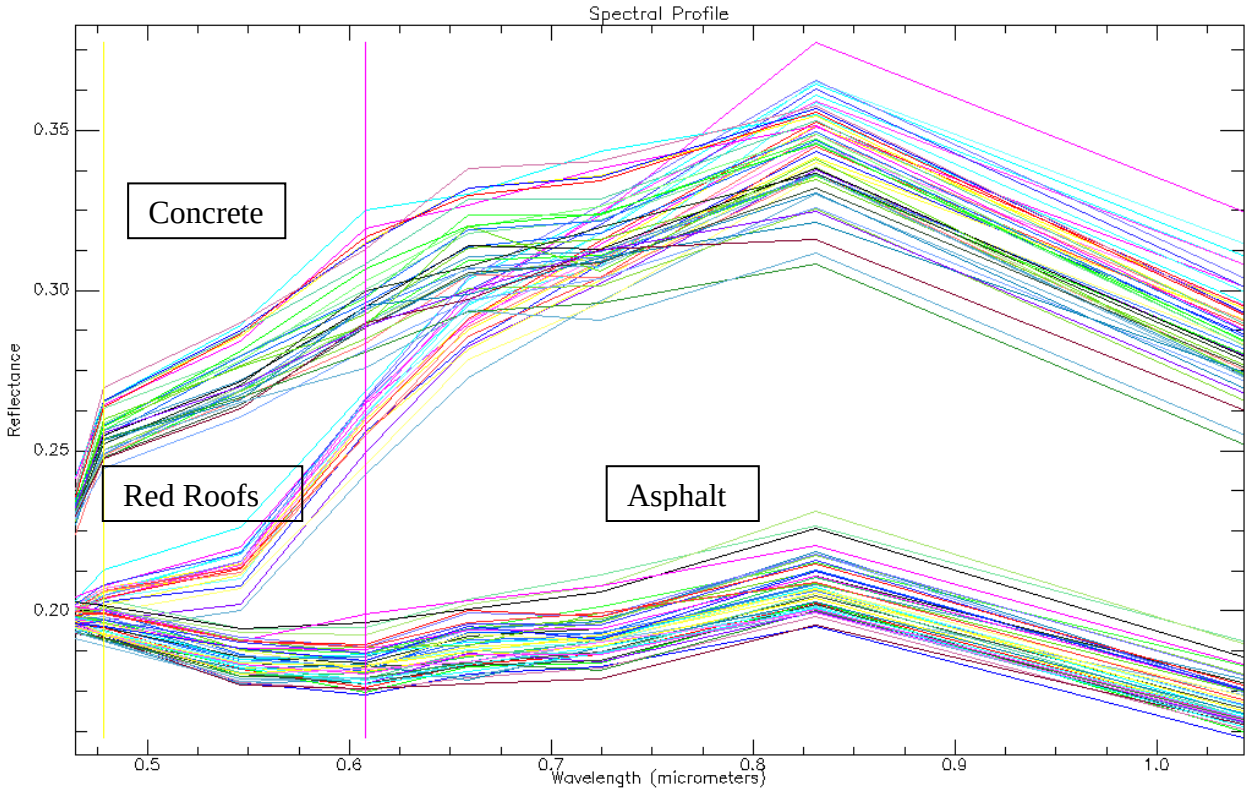

Figure 2-10 Typical reflectance curves for concrete, red roofs and asphalt

2.3 Radiometric Calibration

Multi-temporal High resolution satellite imagery is one of the most important tools for urban planning, change detecting and analyzing trends (El Hajj et al. 2008). In order to obtain accurate quantitative information from multispectral satellite data, such as WorldView-2, conversion of raw digital numbers (DN) to reflectance values is required.

The fact that a uniform scene does not create a uniform image in terms of raw (DN), therefore relative radiometric calibration and correction are necessary. Major causes of non-uniformity include variability in detector response, variability in electronic gain and offset, lens falloff, and particulate contamination on the focal plane (Updike and Comp 2010). The apparent effects of this non-uniformity on the final product will be of the form of:

- Random bad pixels.
- Line start/end problems.
- Full or partial line-column drop-outs.
- Line or column striping.

Normally, as commercial prerequisite, WorldView-2 products are delivered free of the aforementioned deficiencies. However, in case of dealing with multi-temporal data coming from the same or different satellite and to ensure a reliable use of this kind of data, a further radiometric normalization step is required. This step of normalization should include accounting for earth-sun distance, azimuth angle, and relative/absolute atmospheric correction for each of the images in the time series. The main problem here is the difficulty of obtaining an atmospheric characterization at a given acquisition date as it requires the knowledge of the atmospheric properties at the time of acquisition, which is a difficult task even when planned and of course for most historic satellite data (Jensen 1994). In this section, we investigate the quality of the calibration factors provided by the service provider through a process of radiometric calibration which starts with converting DN's to radiance then to reflectance and finally, a relative atmospheric correction takes place. A multi-layer classification scheme will be used as a measure of the quality of the radiometric calibration process. Two scenes for the area of Ismailia, Egypt, captured on the 7^{th} and 16^{th} of April, 2011will be used, the first as a master scene and the second as a slave. Then, a selection of pseudo invariant features will be done to normalize the slave scene to the master scene through a linear regression process. The classification results will be compared and used as a quality control measure for the provided radiometric calibration parameters from the given Meta data file provided by data service provider. In the following

section the calibration parameters and the atmospheric normalization step are evaluated (Elsharkawy et al. 2012).

2.3.1 Data Used

WorldView-2 is the first commercial high-resolution satellite to provide eight spectral sensors in the visible to the near-infrared range, multi-spectral bands come with 2 meters spatial resolution, and a panchromatic band comes with 0.5 meter spatial resolution. Each sensor is closely focused on a particular range of the electromagnetic spectrum, which is sensitive to a specific feature on the ground. Together, they are designed to improve the segmentation and classification of land and marine features (Globe 2009). Figure 2-11 shows a comparison between QuickBird, IKONOS, GeoEye-1 and WorldView-2 in terms of their spectral and panchromatic bands coverage in the spectrum.

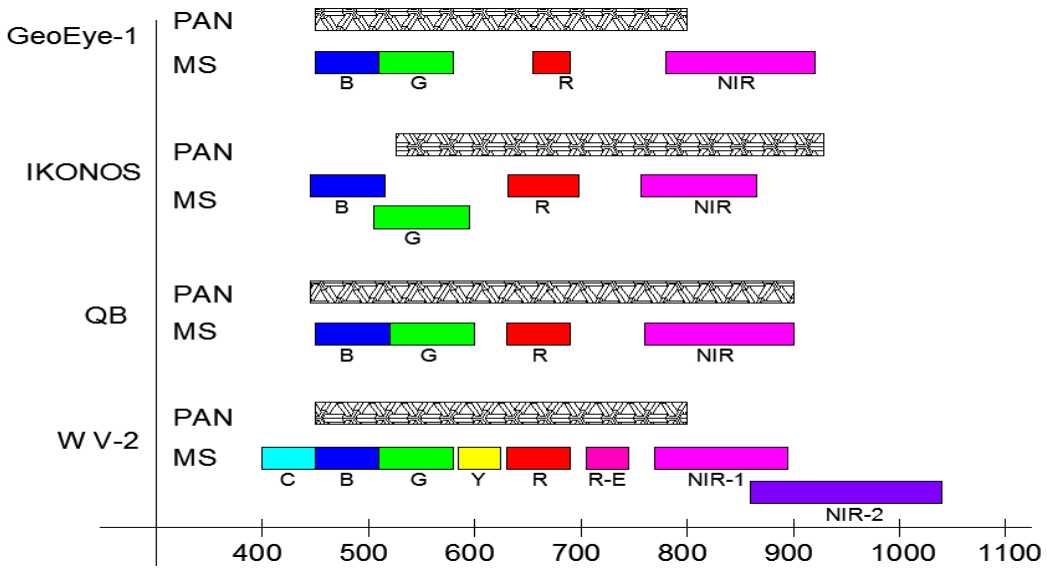

Figure 2-11 Panchromatic and multispectral wavelengths for different satellites, (Elsharkawy et al. 2011)

Generally, The new spectral bands in WorldView-2, Coastal blue, Yellow, Red edge and NIR-2, are targeting costal and vegetation land cover types with applications in plant species identification, mapping of vegetation stress and crop types, wetlands, coast water quality, and bathymetry (Marchisio et al. 2010). Table 2-1, summarizes the range of the spectrum and the characteristics of each band of the WorldView-2 satellite.

Table 2-1 Spectral range and characteristics for each of the eight band (Globe 2009)

Band	*Spectral Resolution*	*Characteristics*
Coastal Blue	(400-450 nm)	New band /least absorbed by water/ Absorbed by chlorophyll in healthy plants
Blue	(450-510 nm)	Provides good penetration of water/ Less affected by atmospheric scattering and absorption.
Green	(510-580 nm)	Ideal for calculating plant vigour and plants types when used in conjunction with the Yellow band
Yellow	(585-625 nm)	New band/Very important for feature classification
Red	(630-690 nm)	Very important band for vegetation Discrimination/Very useful in classifying bare soils, roads, and geological features
Red-Edge	(705-745 nm)	New band/Very valuable in measuring plant health and aiding in the classification of vegetation
NIR1	(770-895 nm)	Separates water bodies from Vegetation/ identifies types of vegetation / discriminates between soil types
NIR2	(860-1040 nm)	New band/ less affected by atmospheric influence/Enables broader vegetation analysis.

As noted in Figure 2-11 and Table 2-1, the Yellow and Red edge bands are filling important gaps in the spectrum that relate to the ability of capturing vegetation (Shafri et al. 2006). Moreover, Coastal blue and NIR2 bands are very helpful to discriminate among different types of vegetation and many man-made objects (Herold et al. 2002).

2.3.2 Area of study

The study area is a residential area in Ismailia city about 120 Kms to the north east direction from Cairo the capital of EGYPT. The study area is mostly urban, vegetation, and desert area with a large mass of a water body. The data was provided by Digital Globe. The images were captured on April 7th and 16th, 2011 at 9:11 AM and 8:40 AM respectively. Figure 2-12 illustrates the study area in false-color composite, NIR-1, G and B.

Figure 2-12 Area of Study

2.3.3 Relative Normalization Process

Generally, any imagery will be used in a radiometric/spectral analysis must be converted to spectral radiance at a minimum, or top of atmosphere reflectance in order to account for the variation in the relative positions between the sun, the Earth and the satellite to obtain absolute values for the NDVI ratios can be applied in any other scene (Updike and Comp 2010). Converting the Digital Numbers (DN) to Top of Atmosphere (ToA) reflectance is a two-step process. First DN's are converted to ToA radiance values. Then these radiance values are then converted to reflectance values (Observation 2010).

2.3.3.1 Conversion to Top-of-Atmosphere Spectral Radiance

According to (Globe 2009), WorldView-2 products are delivered to the customer as radiometrically corrected image pixels. The values of these pixels are calculated as a function of the amount of the spectral radiance enters the telescope aperture and the instrument conversion of that radiation into a digital signal. Therefore, image pixel data are unique to WorldView-2 and should not be directly compared to imagery from other sensors in a radiometric/spectral sense. Instead, image pixels should be converted to a top-of-atmosphere spectral radiance at a minimum. Top-of-atmosphere spectral radiance is defined as the spectral radiance entering the telescope aperture at the WorldView-2 altitude of 770 kms. The conversion from radiometrically corrected image pixels to spectral radiance uses equation 2-1 for each band of a WorldView-2 product (Updike and Comp 2010):

$$L_{\lambda_{pixel,band}} = \frac{K_{band} \cdot q_{pixel,band}}{\Delta\lambda_{band}} \qquad \textbf{2-1}$$

Where, $L_{\lambda_{pixel,band}}$ are the top-of-atmosphere spectral radiance image pixels [$W.m^{-2}.sr^{-1}.\mu m^{-1}$],

K_{band} is the absolute radiometric calibration factor [$W.m^{-2}.sr^{-1}.count^{-1}$] for a given band,

$q_{pixel,band}$ are the given radiometrically corrected image pixels [counts] and

$\Delta\lambda_{band}$ is the effective bandwidth [μm] for a given band

Both K_{band} and $\Delta\lambda_{band}$ can be found in the image metadata files (*.IDM), attached with the WorldView-2 product, see appendix B, under the names (absCalFactor) and (effectiveBandwidth) respectively. The following table summarizes both of these quantities for both the panchromatic and the eight multi-spectral bands.

Table 2-2 Absolute Radiometric Calibration and Effective Bandwidth for the Given Bands

Band name	K_{band}	$\Delta\lambda_{band}$
	$W.m^{-2}.sr^{-1}.count^{-1}$	μm
C	9.30E-03	4.73E-02
B	1.78E-02	5.43E-02
G	1.36E-02	6.30E-02
Y	6.81E-03	3.74E-02
R	1.10E-02	5.74E-02
R-E	6.06E-03	3.93E-02
NIR1	1.22E-02	9.89E-02
NIR2	9.04E-03	9.96E-02

2.3.3.2 Conversion to Top-of-Atmosphere Spectral reflectance

Right now, we have the ToA spectral radiance. However, this top-of-atmosphere spectral radiance varies with Earth-Sun distance, solar zenith angle, topography, bi-directional reflectance distribution function (BRDF-the target reflectance varies depending on the illumination and observation geometry), and atmospheric effects (absorption and scattering) (Updike and Comp 2010). As mentioned earlier that converting multispectral data into reflectance before performing spectral analysis techniques such as band ratios, Normalized Difference Vegetation Index (NDVI), matrix transformations, etc., is a must. For each scene the distance between the sun and earth in astronomical units, the day of the year (Julian date), and solar zenith angle must be known.

$$JD = int[356.25.(year + 4716)] + int[30.6001.(month + 1)] + day + \frac{UT}{24} + (2 - int(\frac{year}{1000}) + int\left(\frac{int(\frac{year}{1000})}{4}\right)) - 1524.5 \quad \textbf{2-2}$$

$$D = JD - 2451545.0 \quad \textbf{2-3}$$

$$g = 357.529 + 0.98560028 * D \quad \textbf{2-4}$$

$$d_{ES} = 1.00014 - 0.01671.cos(g) - 0.00014.cos(2g) \quad \textbf{2-5}$$

The Earth-Sun distance will be in astronomical units (AU) and should have a value between 0.983 and 1.017, equation 2-2. To calculate the distance between earth and sun, equation 2-5, the

constant D, equation 2-3, and the constant g, equation 2-4, must be calculated first. For the WorldView-2 launch date, October 8, 2009 at 18:51:00 GMT corresponds to the Julian Day 2455113.285; the Earth-Sun distance is 0.998987 AU. At least six decimal places should be carried in the Earth-Sun distance for use in radiometric balancing or top-of atmosphere reflectance calculations (Updike and Comp 2010). The average solar Zenith angle has to be calculated for the whole scene at the time of acquisition according to the following equation:

$$\theta_s = 90.0 - sunEL \qquad \textbf{2-6}$$

Where, *sunEl* value can be found in the same file *.IDM. Now we can convert the radiance values to ToA reflectance values using the following equation.

$$\rho_{\lambda_{pixel,band}} = \frac{L_{\lambda_{pixel,band}} . {d_{ES}}^2 . \pi}{E_{sun\lambda_{band}} . cos\ (\theta_s)} \qquad \textbf{2-7}$$

Where $\rho_{\lambda_{pixel,band}}$ are the ToA reflectance values

$L_{\lambda_{pixel,band}}$ are the ToA radiance values

d_{ES} is the Earth-Sun distance in Astronomical Units (AU)

$E_{sun\lambda_{band}}$ WorldView-2 Band-Averaged Solar Spectral Irradiance (Updike and Comp 2010)

θ_s The average solar Zenith angle

The next step involves the relative calibration of the atmospheric effect by normalizing the reflectance values of the second scene (the slave) to the first scene (the master) using regression

line. Pseudo invariant features (PIF's) points were selected in both scenes covering the entire reflectance values and have the following properties:

- be spectrally homogenous; near lambertian and flat surfaces;
- minimal amount of vegetation;
- cover an area greater than three times the pixel size of the sensor;
- And the most important is to exhibit minimum change in spectral characteristics through time.

Good examples of PIF's are: open water points, concrete slabs, sport field grass, bare soil. Figure 2-13, demonstrate examples of the chosen PIF's and their values in the two scenes, for the coastal blue band, before and after regression.

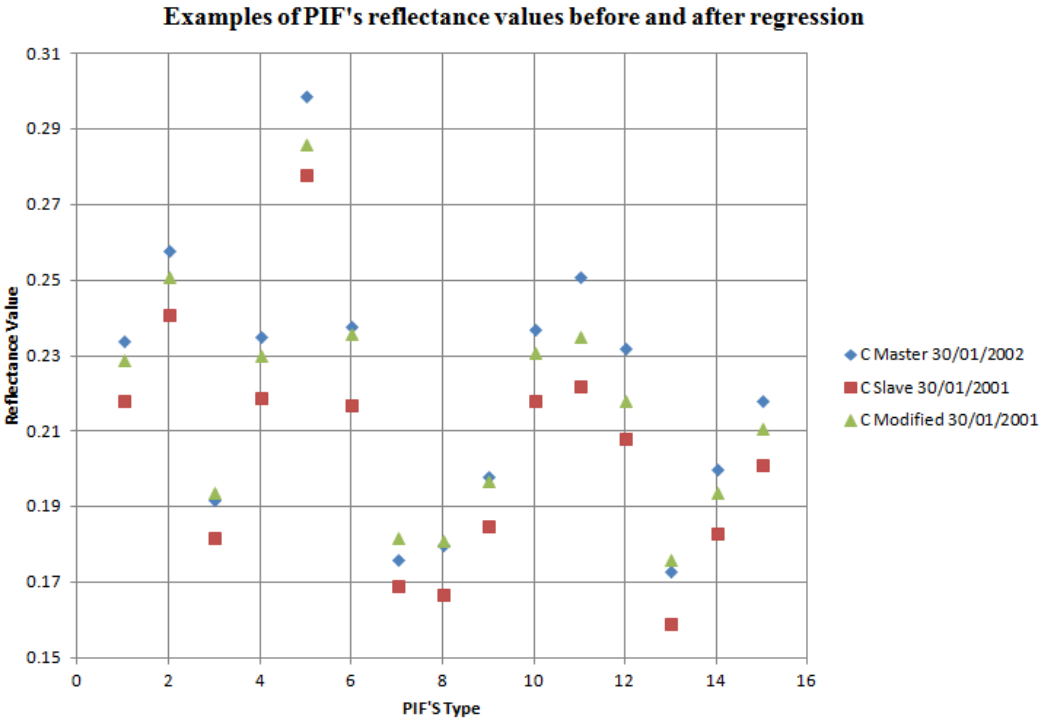

Figure 2-13 Examples of PIF's reflectance values before and after regression

And Table 2-3 lists the eight regression line parameters with their confidence level R^2.

Table 2-3 Regression line parameters for the 8-bands

	Interception	***Slope***	***Confidence level*** R^2
C-band	- 0.0045	1.1048	0.9844
B-band	+ 0.0124	1.0254	0.9824
G-band	+ 0.0147	1.0012	0.9838
Y-band	+ 0.0194	0.9745	0.9865
R-band	+ 0.0225	0.9697	0.9856
R-E-band	+ 0.0314	0.9575	0.9923
NIR-1-band	+ 0.0425	0.9281	0.9933
NIR-2-band	+ 0.0362	0.9233	0.9925

The intercept and slope values were applied against the slave scene to normalize the atmospheric effects with respect to the master scene. The next step will include applying of a multi-layer classification algorithm as shown in Figure 2-14. More details about this algorithm can be found in chapter four. This algorithm will be applied to the master scene and to the slave scene before and after relative atmospheric calibration.

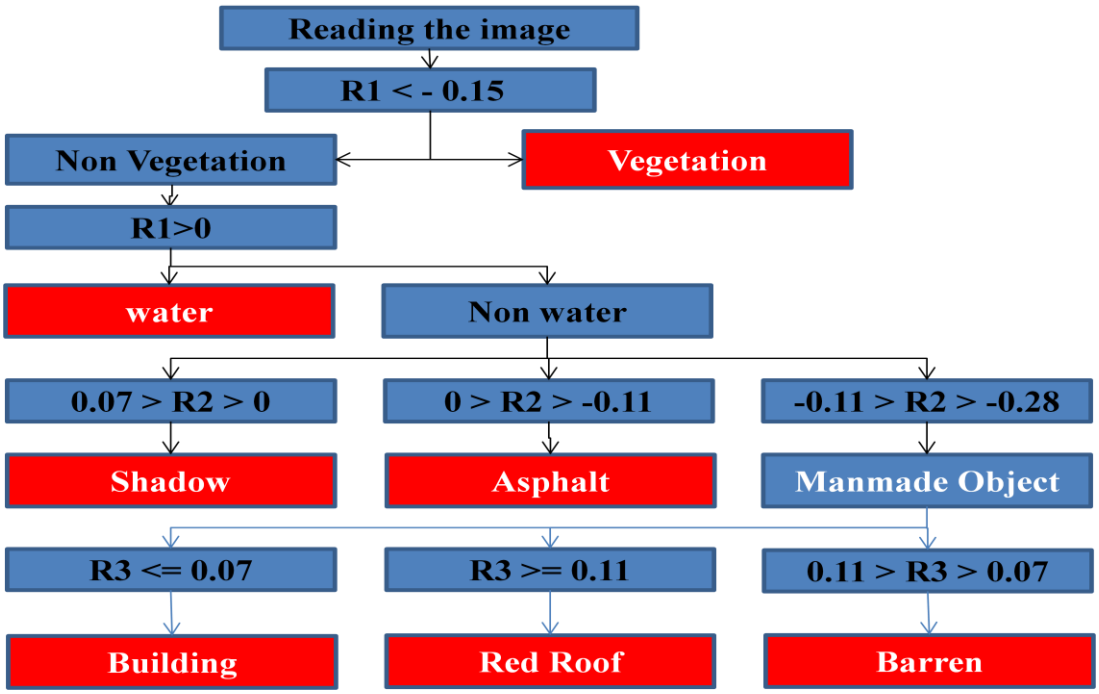

Figure 2-14 Applying the band ratios with the proposed thresholds (Elsharkawy et al. 2012)

2.3.4 Results and Analysis of the relative calibration process

The classification results from the previous multi-layer classification step were then compared with ground truth pixels and the confusion matrices are given in Table 2-4, Table 2-5 and Table 2-6. Note that, all values in these tables are in percentages, an example of Table 2-4 in pixels values will be given in appendix A, and also the definitions of the confusion matrix terms and the calculation procedures will be explained.

Table 2-4 Confusion matrix of the master scene 30-1-2 with the ground truth pixels

Overall Accuracy = 99.2889%
Kappa Coefficient = 0.9885

Class	*water*	*vegetation*	*Bare Soil*	*Asphalt*	*Shadows*	*Red Roof*	*Buildings*	*Total*	*Prod. Acc. (%)*	*User Acc. (%)*
water	100.00	0.00	0.01	0.00	9.15	0.00	0.00	45.21	100.00	99.93
vegetation	0.00	99.30	0.00	0.24	0.12	0.00	0.00	14.07	99.30	99.99
Bare Soil	0.00	0.26	99.50	21.46	0.16	32.16	27.66	39.44	99.50	99.26
Asphalt	0.00	0.27	0.03	62.35	4.44	0.00	7.27	0.42	62.35	78.94
Shadows	0.00	0.10	0.05	13.11	86.13	0.00	1.00	0.36	86.13	70.07
Red Roof	0.00	0.07	0.09	1.95	0.00	67.84	0.00	0.12	67.84	52.80
Buildings	0.00	0.00	0.32	0.89	0.00	0.00	64.07	0.38	64.08	65.38
Total	100%	100%	100%	100%	100%	100%	100%	100%		

Table 2-5 Confusion matrix of the slave scene 30-1-1 without relative atmospheric correction with the ground truth pixels

Overall Accuracy = 97.9841%
Kappa Coefficient = 0.9676

Class	*water*	*vegetation*	*Bare Soil*	*Asphalt*	*Shadows*	*Red Roof*	*Buildings*	*Total*	*Prod. Acc. (%)*	*User Acc. (%)*
water	99.75	0.67	0.05	4.68	90.62	0.00	0.38	44.42	99.75	98.85
vegetation	0.04	98.20	0.00	1.86	0.00	2.51	0.00	13.54	98.20	99.75
Bare Soil	0.00	0.20	98.38	19.99	0.73	70.01	32.15	40.39	98.38	99.10
Asphalt	0.02	0.22	0.01	47.22	2.33	1.08	12.93	0.41	47.22	77.29
Shadows	0.19	0.69	0.01	23.42	5.05	0.47	1.44	0.37	5.05	5.56
Red Roof	0.00	0.02	1.06	1.06	0.04	25.93	0.00	0.48	25.93	7.05
Buildings	0.00	0.00	0.49	1.77	1.23	0.00	53.10	0.39	53.10	44.13
Total	100%	100%	100%	100%	100%	100%	100%	100%		

Table 2-6 Confusion matrix of the slave scene 30-1-1 after relative atmospheric correction with the ground truth pixels

Overall Accuracy = 97.3187%
Kappa Coefficient = 0.9572

Class	*water*	*vegetation*	*Bare Soil*	*Asphalt*	*Shadows*	*Red Roof*	*Buildings*	*Total*	*Prod. Acc. (%)*	*User Acc. (%)*
water	97.00	0.18	0.04	0.07	49.31	0.00	0.00	42.94	97.00	99.44
vegetation	0.04	98.80	0.00	1.93	0.00	2.15	0.00	13.62	98.81	99.74
Bare Soil	0.00	0.25	98.97	24.45	1.34	74.07	48.82	40.72	98.97	98.96
Asphalt	0.03	0.32	0.02	62.15	3.22	0.60	11.39	0.55	62.15	78.76
Shadows	2.93	0.43	0.01	9.14	45.29	0.24	0.82	1.60	45.29	11.52
Red Roof	0.00	0.02	0.80	1.68	0.04	22.94	0.00	0.37	22.94	8.08
Buildings	0.00	0.00	0.16	0.58	0.8	0.00	38.97	0.20	38.97	63.61
Total	100%	100%	100%	100%	100%	100%	100%	100%		

A careful study of the results showed that four classes, highlighted in green, were improved when applying the relative atmospheric correction to the slave scene, Table 2-4, compared to the results from the slave scene without applying the relative atmospheric correction, Table 2-5. Also, the producer and user's accuracies, highlighted in green, were improved for almost all classes. It was notable that the overall accuracy and K coefficient was reduced in Table 2-5 compared to Table 2-4 as the red roofs and buildings' classes give comparatively low percentages.

The same procedure was applied for different study areas over the globe; Brisbane, Cairo, Miami, Rio de Janeiro, San Francisco and Ismailia. The first five scenes were normalized to the scene of Ismailia city. The results of this investigation show very good potentials for the use of the calibration parameters after applying the relative atmospheric normalization (Elsharkawy et al. 2012).

2.4 Linearized Vegetation and shadow Indices

As discussed in section 2.2.1, multispectral bands are extremely important to detect various objects in the image. Most remote sensing satellite sensors offer multispectral images besides panchromatic images. In this section, we summarize various vegetation and shadow–water indices. These indices and other innovated ones will be used in chapter four to extract water, vegetation, shadow, roads network and building classes.

2.4.1 Linearized Vegetation Indices

The primary concept of vegetation indices is that rationing two spectral bands can ultimately cancel the effect of any irrelevant multiplicative factors in sensor data that act equally in the analyzed wave bands (Lillesand and kiefer 2001). The ratio images have two major advantages:

- Large differences in the intensities of the spectral response of different features are well displayed in rationed images if selected properly.
- Ratios can suppress the topographic effects and normalized differences in irradiance when using multi-data images.

This method was originally developed for vegetation studies, commonly known as vegetation indices. For example, the NIR aspect of the spectrum is highly absorbed by water and highly reflected by vegetation, while the red part of the spectrum has the same reflective properties for both of water and vegetation. Therefore, it is expected for the NIR band to exhibit a low DN value in the body of water areas and high DN values in vegetation areas.

As explained in section 2.2.1, and following (Ünsalan and Boyer 2011) in his survey, the aforementioned characteristics of chlorophyll are usually used to create indices to detect the presence and the density of vegetation in multispectral satellite or airborne imagery.

In 1969, (Jordan 1969) introduced the ratio vegetation index (*RVI*) to estimate the vegetation density in a given region. Jordan designed his ratio based on the high absorption in the red band and low absorption in the near-infrared, as follows:

$$RVI = \frac{\rho_{nir}}{\rho_{red}} \qquad \textbf{2-8}$$

Where: $\boldsymbol{\rho_{nir}}$ and $\boldsymbol{\rho_{red}}$ are reflectance values in near-infrared and red bands, respectively.

(Colwell 1973), found that the RVI ratio diverges to infinity when $\boldsymbol{\rho_{red}}$ goes to zero. Later, (Nalepka et al. 1977) introduced more linearized index using the square root of the RVI, and generate the SRRVI as follows:

$$SRRVI = \sqrt{RVI} = \sqrt{\frac{\rho_{nir}}{\rho_{red}}} \qquad \textbf{2-9}$$

(Rouse et al. 1974) introduced the most popular vegetation indices among all the normalized difference vegetation indices (NDVI) as follows:

$$NDVI = \frac{\rho_{nir} - \rho_{red}}{\rho_{nir} + \rho_{red}} \qquad \textbf{2-10}$$

(Kauth and Thomas 1976) introduced another vegetation index using four Landsat MSS bands, (d_4, d_5, d_6, d_7), d_4 is the blue band, d_5 is the red band while, d_6 and d_7 are near-infrared.

$$\begin{bmatrix} b \\ g \\ y \\ n \end{bmatrix} = \begin{bmatrix} 0.433 & 0.632 & 0.586 & 0.264 \\ -0.290 & -0.562 & 0.600 & 0.491 \\ -0.829 & -0.522 & -0.039 & 0.194 \\ 0.223 & 0.012 & -0.543 & 0.810 \end{bmatrix} \times \begin{bmatrix} d_4 \\ d_5 \\ d_6 \\ d_7 \end{bmatrix} + \begin{bmatrix} 32 \\ 32 \\ 32 \\ 32 \end{bmatrix} \quad \textbf{2-11}$$

Where b stands for 'brightness', g stands for 'greenness', y stands for 'yellowness', and n stands for 'nonesuch'. Greenness is taken as a vegetation index from this transformation (Ünsalan and Boyer 2011).

Generally, NDVI continues to be one of the most effective indices indicating the presence and density of vegetation. All the comparison studies with other indices didn't declare a clear winner (Ünsalan and Boyer 2011). In this study, we will use NDVI in essence to differentiate between two main classes, vegetation and water, as they fall in the two far ends of the ratio range. Moreover, two new NDVI like ratios will be used to detect, shadow, asphalt, buildings and bare soil. The details of this algorithm will be discussed in chapter four.

2.4.2 Linearized Shadow Indices

Shadow effect is unavoidable phenomenon, and it is very difficult to classify shaded area as the radiance values drops significantly and gives a very close spectral response to water. However, this phenomenon may be very useful in determining other objects which are known to be associated with shadows such as buildings. In this study a new band ratio to detect shadow is introduced using the coastal-blue (C) and red (R) bands of the WorldView-2 imagery.

2.5 Land Use Classification

The term land use classification can be extended to cover many applications ranging from general land cover detection to detailing crop specifications.

In order to classify an image, we have to go through several steps; starting from handling the data by means of some pre-processing steps, then a feature extraction step, then a training phase and ending with a classification and labeling algorithm. Figure 2-15 illustrates the outlines of this process.

Handling the data is basically a series of pre-processing steps may include, but not limited to, the following:

- Increasing the spatial resolution by means of a data fusion technique between the panchromatic and multispectral bands,
- Converting the digital numbers, DN, values to top of atmosphere radiance or reflectance,
- Relative/absolute atmospheric corrections,
- Various geometric corrections.

Feature extraction step includes the transformation of the multi-spectral image to other domains (spatial-frequency) and applying certain filters to enhance, detect or extract a certain feature. Also feature extraction step involves data dimensionality reduction through PCA or data subsisting (Schowengerdt 2006).

Classifier step may be carried out using supervised or unsupervised classification techniques to determine the boundaries of each class. Finally, a **Labeling** process is carried out to label each group of pixels to a certain class; the output map should have a unique label for each class.

In the following two sections, two basic methods of land use classification will be emphasized. The first explored approach is the pixel-based classification method and the second one, is the object-based classification method. These two methods are among the earliest approaches to the land use classification problem. What characterizes these two methods is the simplicity in concept and in application compared to other feature extraction methods such as; Markov

Random Fields, artificial intelligence, rule based systems or Bayesian belief networks (Ünsalan and Boyer 2011).

In general, monitoring of urban environments is a challenging area of remote sensing because of different and excessive spatial and spectral diversity of surface matter (Herold et al. 2003). As discussed in (Taubenbock et al. 2010), the contrast of urban surfaces, particularly those in developing countries, is due mainly to their unstructured urban patterns which contain a complicated wide range of urban landscapes such as; bare soil, water, vegetation, roads, sidewalks and buildings with different patterns and alignments. As a result of the increase in spatial resolution individual pixels may only have a meaning in the context where they take place (Franklin and Wilson 1991). Therefore, both contextual and spectral attributes must be involved in the classification algorithm. In the next two sections pixel-based and object-based concepts will be emphasized and some of their techniques will be explained.

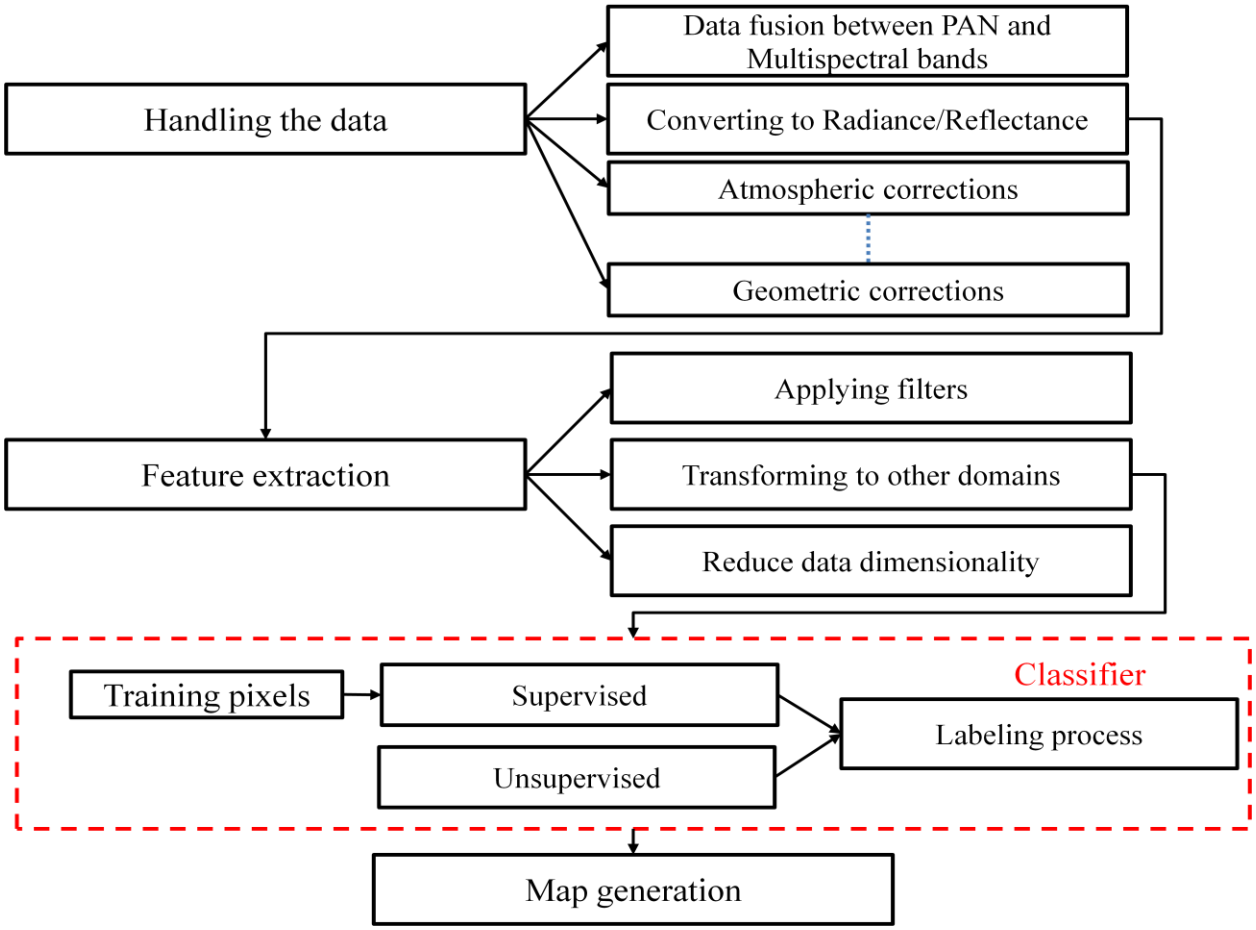

Figure 2-15 Outlines of data flow in a classification process, after (Schowengerdt 2006)

2.5.1 Pixel -based approach

A conventional pixel-based classification approach, based on statistical algorithms has been used for decades (Tso and Mather 2009). Generally, this approach is very useful in large scale images where a separation can be efficiently established between water, urban, and vegetation areas according to their spectral characteristics. However, in cases of similar spectral information the ability of this approach is limited (Yan 2003). The main assumption in using this approach is that the single pixel contains sufficient grey level information to be assigned to a certain class. Recent advances in satellite imagery provide sub meter spatial resolution as in IKONOS, GeoEye, Quickbird and WorldView-2. The challenge in using this approach, especially in urban areas, is

the heterogynous nature of objects in these areas, as the classification will be entirely depending on the spectral response to the objects on the earth surface, without looking into the spatial coherence between adjacent pixels. Moreover, many objects such as; buildings, concrete roads, sidewalks and parking lots will have a nearly identical spectral response as the main construction material is almost the same. Another example for spectral similarity is the resemblance of water with shadowed areas, which makes the classification process almost impossible due to this spectral confusion.

There are three popular pixel-based statistical classifiers commonly used in the supervised classification; the parallelepiped method, minimum distance classifier, and the maximum likelihood classifier.

In the three aforementioned methods the signatures generated by the training data will differ according to the classifier type used. "*For parallelepiped classification the class signatures will be the upper and lower bounds of brightness in each spectral band. For minimum distance classification the signatures will be the mean vectors of the training data for each class, while for maximum likelihood classification both class mean vectors and covariance matrices constitute the signatures*" (Richards and Jia 2006).

The primary difference between the unsupervised and supervised approaches is that for the unsupervised methods, only the number of clusters are entered without selecting any training data set, and the classifier automatically constructs the clusters by minimizing a predefined error function. However, in certain cases the number of clusters can be detected automatically by the classifier (Yiu-ming 2005). While the unsupervised classification approach is often more suitable in an automatic classification solution, where user interference is not required, in practice,

results are accepted or rejected based on whether they meet the user's expectations (Tso and Mather 2009). In the next subsections, the three popular techniques for the supervised pixel-based classifiers will be explained.

2.5.1.1 Parallelepiped method

In this method a parallelepiped-like (i.e., hyper-rectangle) subspace is defined for each class. Using the training data for each class the limits of the parallelepiped subspace can be defined either by the minimum and maximum pixel values in the given class, or by a certain number of standard deviations on either side of the mean of the training data for the given class (Tso and Mather 2009).

The pixels lying inside the parallelepipeds are tagged to this class. Figure 2-16 depicts this criterion in cases of two-dimensional feature space.

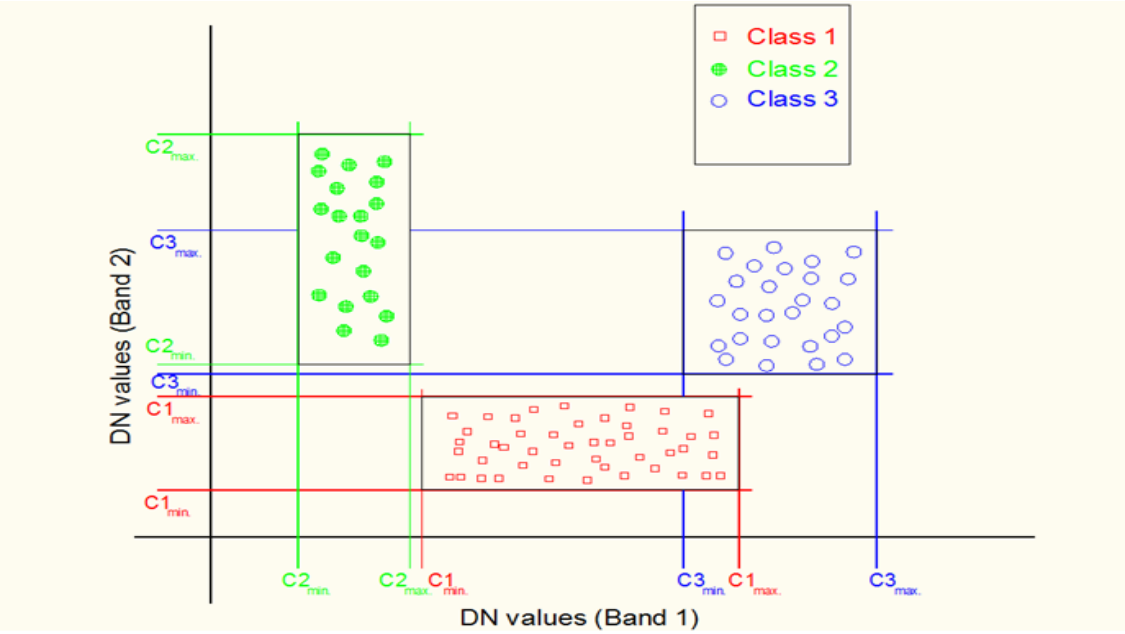

Figure 2-16 Implementation of the parallelepiped classification method for three classes using two spectral bands, after (Tso and Mather 2009).

Although this method is quick and easy to implement it is very difficult to grant a robust classification performance as a result of serious errors that may take place. These errors are originated from the possibility of having one or more pixels lying in more than one parallelepiped, or outside all parallelepipeds. Essentially, these errors are likely to occur with more complex feature space (Tso and Mather 2009). A modification to this method was introduced by (Elsharkawy et al. 2011). The proposed modification involves applying this method using only one pair of bands at a time to overcome the problem of finding one pixel in more than one class. On the other hand, many un-classified pixels will exist which will be classified later using another spectral characteristic.

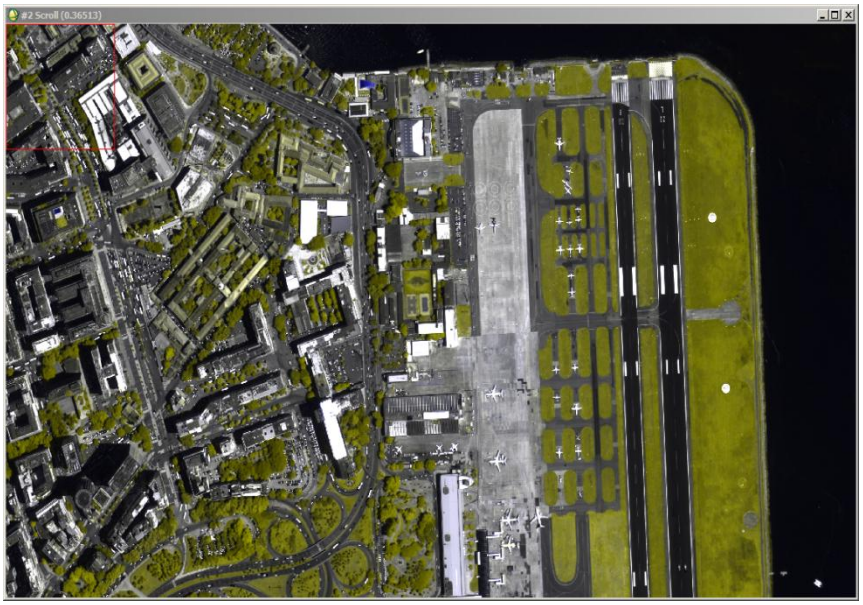

Figure 2-17 Study area for the modification of the parallelepiped method

Figure 2-18 and Figure 2-19 demonstrate the classification results for the proposed modification and one of the commercial software respectively, using the same training pixels.

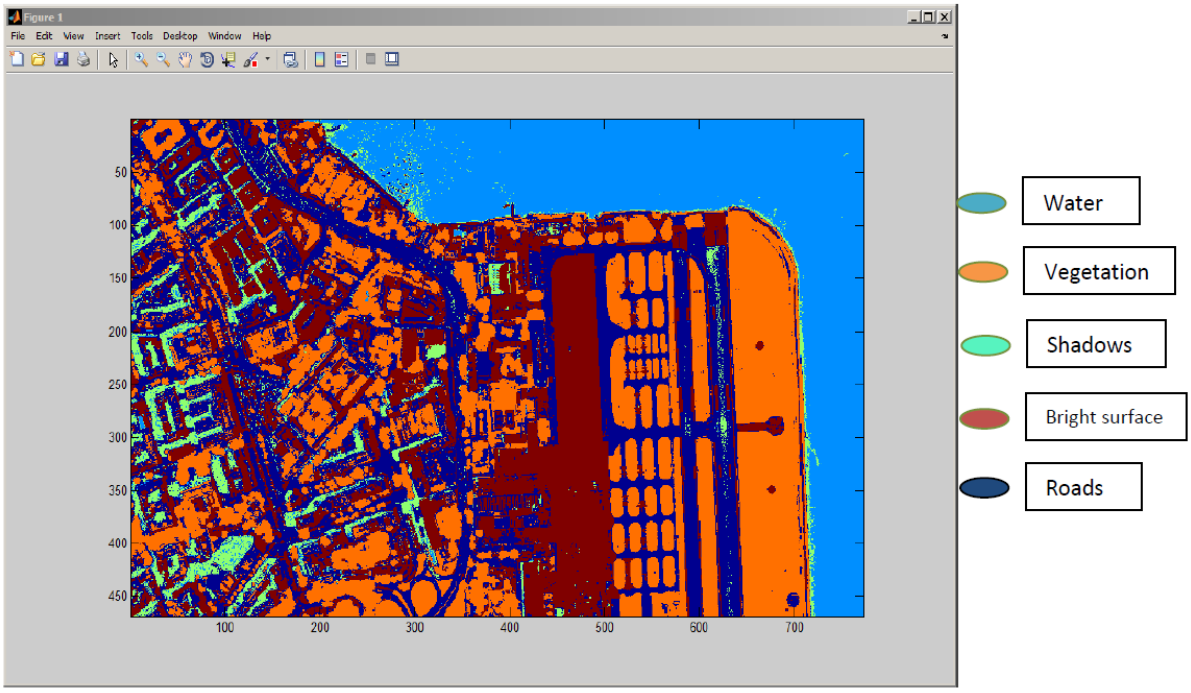

Figure 2-18 Classification results using the modified parallelepiped method

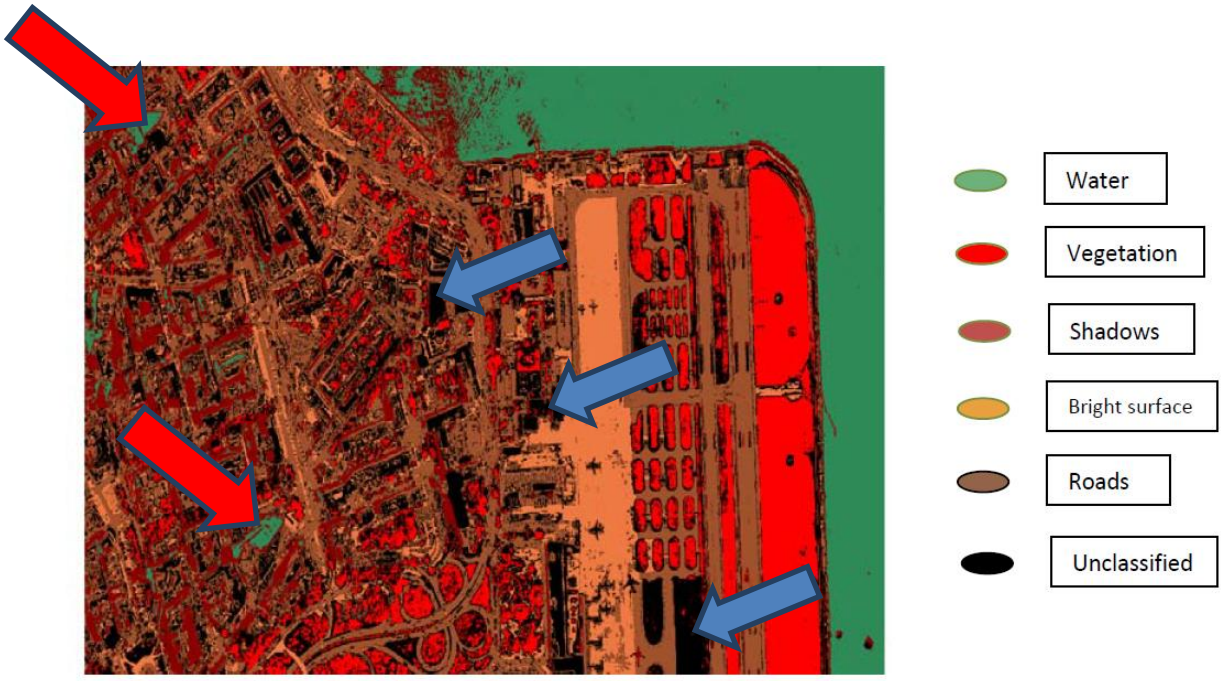

Figure 2-19 Classification results using commercial software

It was clear that the proposed modification yields better results than the commercial software, while blue arrows are pointing towards unclassified pixels and red arrows are pointing towards misclassified pixels. For more detail regarding this method please refer to (Elsharkawy et al. 2011). The proposed methodology showed a good result for distinguishing four main classes, namely; vegetation, water, shadow, and man-made objects. WorldView-2 eight band data will be used in the assessment and verification of the new approach.

2.5.1.2 Maximum Likelihood Classifier (MLC)

The maximum likelihood (ML) procedure is the most common supervised method used with remote sensing. It can be described as a statistical approach to pattern recognition where the probability of a pixel belonging to each of a predefined set of classes is calculated; hence the pixel is assigned to the class with the highest probability (Tso and Mather 2009). ML is based on the Bayesian probability formula.

Bayes' Classification:

The MLC decision rule is based on a normalized (Gaussian) estimate of the probability density function of each class (Pedroni 2003). Hence, under this assumption and using the mean vector along with the covariance matrix, the distribution of a category response pattern can be completely described (Yan 2003). Given these parameters, the statistical probability of a given pixel value can be computed for being a member of a particular class. The pixel would be assigned to the class with highest probability value or be labelled "unknown" if the probability values are all below a threshold set by the user (Lillesand and kiefer 2001).

Let the spectral classes for an image be represented by

$$\omega_i , \qquad i = 1, \ldots M$$

Where, M is the total number of classes.

In order to determine the class to which a pixel vector x belongs; the conditional probabilities of interest should be followed.

$$p(\omega_i/x), \qquad i = 1, \ldots M$$

The measurement vector x is a column of Digital Number's (DN) values for the pixel, where its dimension depends on the number of input bands. This vector describes the pixel as a point in multispectral space with co-ordinates defined by the DN's (Figure 2-20).

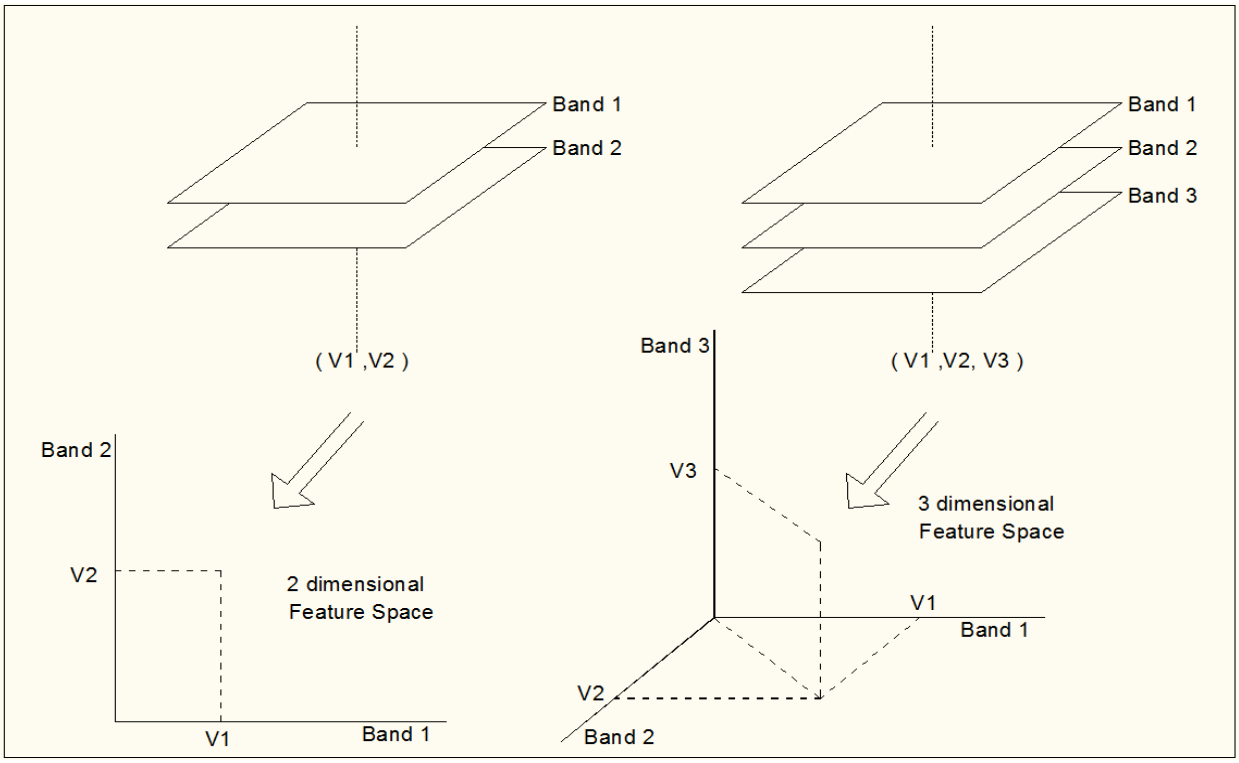

Figure 2-20 Feature space and how a feature vector is plotted in the feature space (Yan 2003)

The probability $p(\omega_i |x)$ gives the likelihood that the correct class is ω_i for a pixel at position x. Classification is performed according to:

$$x \in \omega_i \quad , \quad if\, p(\omega_i/x) > p(\omega_j/x) \qquad for\, all \quad j \neq i \qquad \textbf{2-12}$$

i.e., the pixel at x belongs to class ω_i if $p(\omega_i|x)$ is the largest. This general approach is called Bayes' classification which works as an intuitive decision for the Maximum Likelihood Classifier method (Richards and Jia 2006).

From this discussion one may ask how can the available $p(x|\omega_i)$ can be related from the training data set, to the desired $p(\omega_i|x)$ and the answer is again found in Bayes' theorem (Freund 1992).

$$p(\omega_i/x) = p(x/\omega_i)\, p(\omega_i)/p(x) \qquad \textbf{2-13}$$

Where $p(\omega_i)$ is the probability that class ω_i occurs in the image and also called *a priori* or prior probabilities. And p(x) is the probability of finding a pixel from any class at location x

Rewriting the classification rule, Eq.2-12, using Eq.2-13 and removing p(x) as a common factor results in:

$$x \in \omega_i, \; if \;\; p(x/\omega_i)\, p(\omega_i) > p(x/\omega_j)\, p(\omega_j) \quad for\, all \quad j \neq I \qquad \textbf{2-14}$$

The rule of Eq.2-14 is more acceptable than that of Eq.2-10 since the $p(x|\omega_i)$ are known from training data, and $p(\omega_i)$ are also known or can be estimated from the user's experience and the prior knowledge of the image (Richards and Jia 2006). A detailed comparison between two data sets, one with near-infrared and three visible and the other with the full 8-bands, was made to

emphasize the important role of the new bands for improving the separability measurement and the final classification results (Elsharkawy et al. 2012).

2.5.1.3 Minimum distance to mean classifier: (The Case of Limited Training Data)

To have an effective maximum likelihood classification one should have a sufficient number of training pixels for each class. This is because this method is entirely dependent on the quality of the estimation of the mean vector and the covariance matrix for each spectral class (Richards and Jia)**.** Contrastingly, when no sufficient training data is available the MLC will lead to poor classification. In this particular case, it will be better to use Minimum Distance rather than mean classifier. This classifier does not make use of covariance information but instead depends only upon the mean positions of the spectral classes (Richards and Jia).

The minimum distance between the pixel and the class centers, is the decision rule to determine a pixel's label (Tso and Mather 2009). Figure 2-21 depicts an example of minimum distance classification criteria.

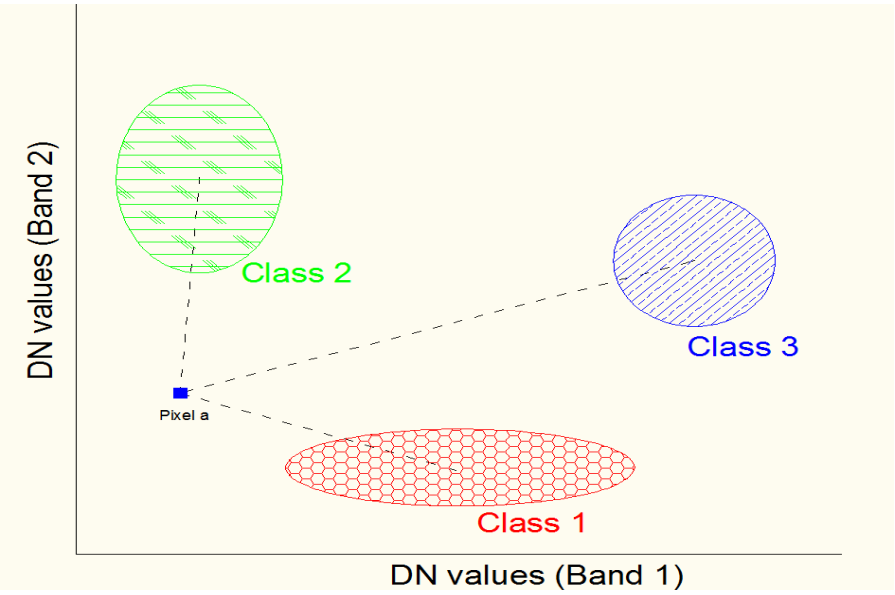

Figure 2-21 Example of minimum distance classification criteria, after (Tso and Mather 2009)

2.5.2 Object -based approach

In high-resolution satellite imagery, the pixel is relatively small and the texture information occurring within the relationship between pixels is quite meaningful. Therefore, the use of contextual information in addition to spectral features for image classification will result in an improved level of accuracy (Ouma et al. 2010). The assumption behind this approach is that the classification is based on pixel grouping that will devise set of objects; this devise a set of objects will be later classified using specific rule sets (Cu et al. 2009). The segmentation process is the most important step in the object-based process, where the segments are determined based on specific scale, shape and compactness factors. Most effort of researchers was towards generating innovative rule sets according to the nature of the input date, the detected objects and the targeted classes, or developing novel methods for integrating pixel and object-based techniques (Yan 2003; Bhaskaran et al. 2010; Ouma et al. 2010; Taubenbock et al. 2010; Elsharkawy et al. 2012). According to (Gonzalez and Woods 1992) segmentation can be done either two ways; **detecting similarity**, as in clustering pixels according to specific rules, or **detecting singularity** i.e edge detection. Most of the researches in the area of object-based classification are using the first method, detecting similarity**,** where the clustering of pixels being done according to their texture, intensity …etc. In this thesis the second generation curvelet transform will be used as an edge detection tool to start the segmentation part during the process of the object-based classification algorithm, as explained in chapter three.

Chapter Three: **Edge Detection Techniques**

3.1 Introduction

In this chapter, three edge detection techniques will be discussed; two in the frequency domain, curvelet and wavelet transforms and one in the spatial domain, the canny operator. First a brief introduction to the filtering in the frequency domain, section 3.2, will be introduced to emphasize the advantages of switching from the spatial domain to the frequency domain. Then in the following three sections, 3.3, 3.4 and 3.5, a theoretical background for the three techniques will be given. In section 3.6 the implementation of curvelet transform for edge detection of high resolution satellite imagery will be discussed with the results compared to the other two techniques. Finally, in section 3.7 a new approach for combining curvelet and canny for edge detection will be introduced with the corresponding results.

3.2 Filtering in the frequency domain

Filtering is one of the most fundamental digital image processing research fields. This significance comes from the fact that all imagery must undergo different types of texture and edges enhancement, images sharpening, etc., in order to highlight certain features to smooth the process of either classification or detection of objects (Liu and Mason 2009). Filtering can be done either using the concept of convolution, in the spatial domain, by studying the relatively small neighbourhood of a pixel or using the Fourier transforms, FT, by examining the global spatial content in the frequency domain (Schowengerdt 2006).

3.2.1 The convolution theorem

The process of convolution in the spatial domain is underlying the use of a moving window along the image pixels. A certain operation, a filter, is performed within this window and the calculated output, at the center of this window, then produce the output image. This process will

be repeated for every pixel in a row then for every row in an image (Schowengerdt 2006). Examples of the filters that may be implemented in the spatial domain using the convolution are given in Table 3-1.

Table 3-1 Examples for spatial domain filtering using convolution theorem, after (Schowengerdt 2006)

Type	Output	Examples	Applications
Linear	Weighted sum	Low-Pass filter (LPF) High-Pass filter (HPF) High-Boost filter (HBF) Band-pass filter (BPF)	Enhancement, sensor simulation and noise removal
Statistical	Given statistic	Minimum, maximum, median, standard deviation,……	Noise removal, feature extraction and S/N measurement
Gradient	Vector gradient	Sobel, Roberts,….	Edge detection

Thanks to the famous convolution theorem, the process of convolution has a particularly straightforward and convenient form, in the frequency domain. Consider two 2-D functions $f(x,y)$ and $h(x,y)$ having Fourier transforms respectively denoted by $F(k_x,k_y)$ and $H(k_x,k_y)$ (Solomon and Breckon 2011). F is denoting the operation of taking a 2-D Fourier transform, the convolution theorem states that:

$$F\{f(x,y)**h(x,y)\} = F(k_x,k_y)H(k_x,k_y) \qquad \textbf{3-1}$$

The previous equation indicates that, the processing of convolving two functions in the spatial domain can be equivalently carried out by simple multiplication of their transforms in the frequency domain. This form of the convolution theorem outlines the fundamental core for the powerful methods of frequency-domain filtering (Solomon and Breckon 2011).

Although, the FT is less computationally efficient for raster data, in terms of speed and computing resources, it is more flexible than convolution in accommodating many filtering functions (Liu and Mason 2009). In this research curvelet transforms will be implemented for edge detection, in the frequency domain, and will be compared to wavelet and the traditional Canny operator in the spatial domain. The following summarize the reasons of why frequency domain filtering is implemented in this research:

- Introducing an alternative description to the spatial representation.
- Filtering can be performed on selected frequencies which may decrease the computational burden.
- Hosting of more efficient and less sensitive to noise calculations.
- Designing of considerably flexible various filters such as; image enhancement, image restoration, image compression, image denoising (Solomon and Breckon 2011).

In the next three sections, the implementation of three techniques, curvelet transforms, wavelet transforms and canny operator, will be discussed addressing the edge detection problem in high resolution satellite imagery.

3.3 Curvelet transform

Curvelet transforms technique was originally introduced by Candes and Donoho in 1999 as a result of the increasing demand for an effective multi- resolution analysis that has the ability to overcome the drawbacks of wavelet analysis. The transform was designed to represent edges and other singularities along curves much more efficiently than traditional transforms, i.e. using significantly fewer coefficients for a given accuracy of reconstruction (Donoho and Duncan 2000). This transform used a complex series of steps involving the ridgelet analysis of the radon transform of an image. However, the performance was considered slow.

Later and based upon a frequency partition technique, the same authors, Donoho and Duncan, proposed a considerably simpler second-generation curvelet transform. This second-generation curvelet transform is meant to be simpler to understand and use. It is also faster and less redundant compared to its first-generation version (Ma and Plonka 2009). In the new version of curvelet, the ridgelet transforms was discarded, thus reducing the amount of redundancy in the transform and increasing the speed considerably. Curvelet transform is defined in both continuous and digital domain. Moreover, it can be used for multi-dimensional signals. Since the image-based feature extraction requires only 2D FDCT, the discussion will be focused on only two-dimensional applications and implementations (Candes et al. 2006).

3.3.1 Continuous-time Curvelet Transforms

The curvelet representation in two dimensions continuous space, i.e., R^2, will be through spatial variable x, with ω, a frequency-domain variable, and with r and θ, polar coordinates in the frequency domain. Then, a pair of windows function, *W(r)* and *V(t), i*s introduced, the "radial window" and "angular window" respectively. These windows will obey the admissibility conditions:

$$\begin{cases} \sum_{j=-\infty}^{\infty} W^2(2^j r) = 1 \quad , \quad r \in (\frac{3}{4}, \frac{3}{2}) \\ \sum_{l=-\infty}^{\infty} V^2(t-l) = 1, \quad t \in (-\frac{1}{2}, \frac{1}{2}) \end{cases} \qquad \textbf{3-2}$$

Where, *j* is a radial variable and *l* is an angular variable. The frequency window in the Fourier domain is defined by:

$$U_j(r,\theta) = 2^{-\frac{3j}{4}} W(2^{-j} r) V\left(\frac{2^{\lfloor j/2 \rfloor}\theta}{2\pi}\right) \qquad \textbf{3-3}$$

Where $\lfloor j/2 \rfloor$ is the integer part of *j*/2

In the spatial Cartesian domain, the scaling of the radial window introduces an angular window with short axis with 2^{-j}, and a long axis with $2^{-j/2}$. *T*herefore, the effective length and width obey the anisotropy scaling relation width ≈ length^2, and U_j is a polar wedge window, as shown in Figure 3-1.

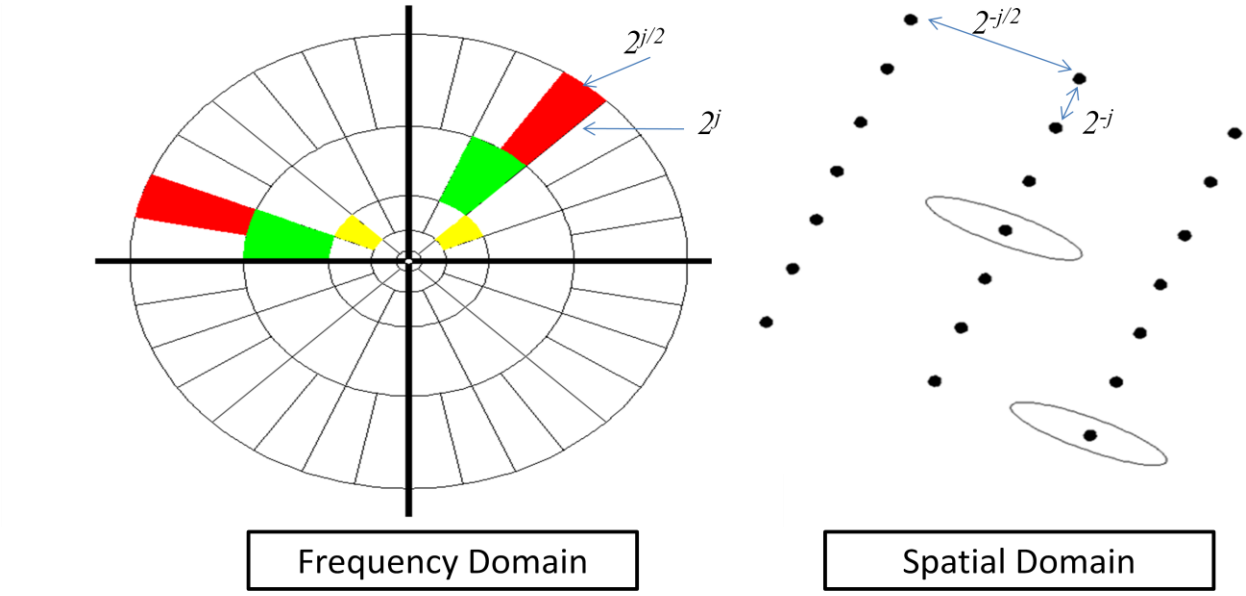

Figure 3-1 Curvelets in Fourier frequency (left) and spatial domain (right) after (Candes et al. 2006)

In the frequency domain, the curvelet coefficient, with the *j* scale, the *l* angle and the sequence of translation parameters $k = (k_1,k_2) \in Z^2$, is defined as:

$$C(i,j,k) := \frac{1}{(2\pi)^2} \int \hat{f}(\omega) U_j(R_\theta \omega) e^{i\left(x_k^{(j,l)},\omega\right)} d\omega \qquad \textbf{3-4}$$

Figure 3-1, illustrates the result of partitioning the Fourier plane into radial (concentric circles) and angular divisions. The concentric circles are responsible for the decomposition of an image into multiple scales, *j*, while the angular divisions partition the band passed image into different angles or orientations *l* (Zhenghai and Jianxiong 2009). For instance, the yellow wedges represent the maximum support of the curvelet function $\hat{\varphi}$ (3,3,k) and $\hat{\varphi}$ (13,3,k), while the green

wedges represent $\hat{\varphi}$ (2,4,k) and $\hat{\varphi}$ (13,4,k) and the red wedges represent $\hat{\varphi}$ (4,5,k) and $\hat{\varphi}$ (26,5,k). As a result, defining the scale *j* and angle *l* is the proper way to deal with a particular wedge. By assessing the spatial domain in Figure 3-1right, it was found that each of the wedges corresponds to a specific curvelet, shown as ellipses, at a given scale and angle. This indicates that the curvelet coefficients for that scale and angle can be determined by the inverse FFT of this particular wedge (Guha and Wu 2010). This is the main idea behind the implementation of curvelet transform. Generally, curvelets are well localized, needle-shaped in higher scales, and the wedges are longer and thinner with scale growing (Ma and Plonka 2009).

3.3.2 Discrete Curvelet Transform

Coronae and rotations, as in the continuous-time definition, are not especially adapted to Cartesian arrays, so it is convenient to replace these concepts by Cartesian equivalents; here, "Cartesian coronae" based on concentric squares (instead of circles) and shears.

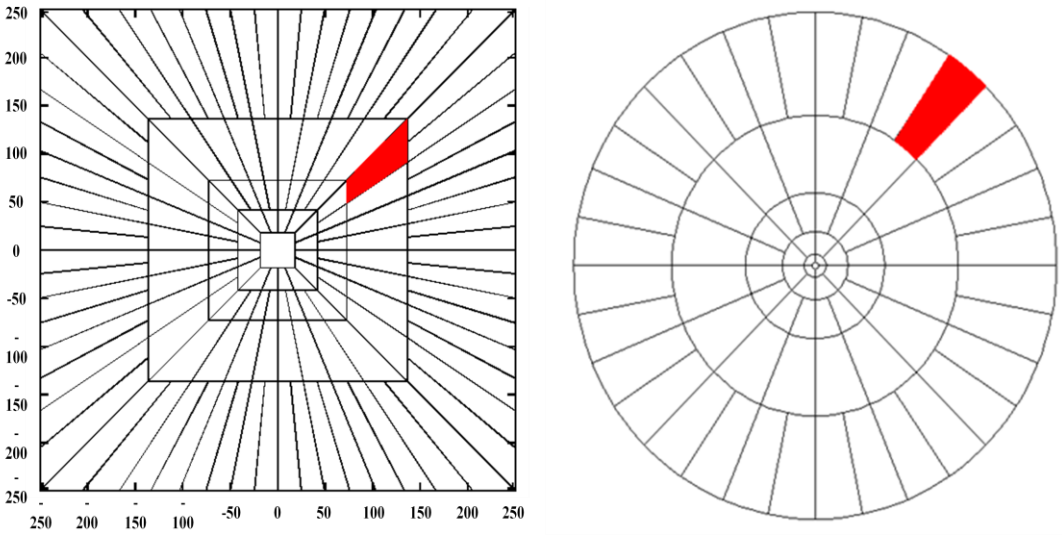

Figure 3-2 The transition from the continuous-time definition (right) to the discrete-time definition(left) after (Candes et al. 2006).

Figure 3-2 (left) illustrates the basic digital tiling where the windows ˜U$_j$` smoothly localize the Fourier transform near the sheared wedges obeying the parabolic scaling. The shaded region represents one such typical wedge. Now the Cartesian window $\widetilde{U}$ is defined as:

$$\widetilde{U}_{j,l}(\omega) \coloneqq \widetilde{W}_j(\omega)\widetilde{V}_j(S_{\theta l}\omega) \qquad \textbf{3-5}$$

Where:

$$\begin{cases} \widetilde{W}_j(\omega) = \sqrt{\phi_{j+1}^2(\omega) - \phi_j^2(\omega)}, \\ \widetilde{V}_j(\omega) = V\left(\dfrac{2^{\left\lfloor \frac{j}{2} \right\rfloor}\omega_2}{\omega_1}\right) \end{cases} \qquad \textbf{3-6}$$

Φ is defined as the product of low-pass one dimensional windows:

$$\phi_j(\omega_1, \omega_2) = \phi\left(2^{-j}\omega_1\right)\phi(2^{-j}\omega_2) \qquad \textbf{3-7}$$

And S_o is the shear matrix:

$$S_\theta \coloneqq \begin{pmatrix} 1 & 0 \\ -tan\theta & 1 \end{pmatrix} \qquad \textbf{3-8}$$

Hence, the discrete curvelet coefficients are defined as:

$$C(i,j,k) \coloneqq \int \hat{f}\,(\omega)\widetilde{U}_j(S_{\theta l}^{-1}\omega)e^{i(S_{\theta l}^{-T},\omega)}d\omega \qquad \textbf{3-9}$$

According to (Candes et al. 2006), there are two different digital implementations of FDCT:

- Curvelets via **USFFT** (Unequally Spaced Fast Fourier Transform), and
- Curvelets via **Wrapping**.

Both variants are linear and take a cartesian array as input to provide an output of discrete coefficients. The only difference is in the choice of the spatial grid where curvelets at each scale and angle are translated. As the FDCT wrapping is the fastest curvelet transform currently available (Candes and Donoho 2005), the wrapping version of curvelet transforms, will be used throughout the implementation. The FDCT wrapping algorithm may be summarized as follows:

1. Perform FFT of the image
2. Divide the FFT into collection of Digital Corona Tiles as shown in Figure 3-2
3. Perform the following for each corona tile:

- Translate the tile to the origin as in Figure 3-3.
- Wrap the parallelogram shaped support of the tile around a rectangle centered at the origin as in Figure 3-4.
- Take the inverse FFT of the wrapped support.
- Add the curvelet array to the collection of curvelet coefficients.

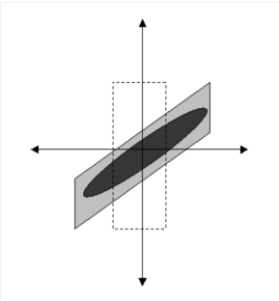

Figure 3-3 Support of wedge before Wrapping

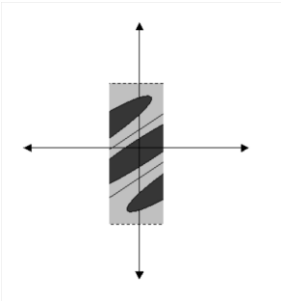

Figure 3-4 Support of wedge after Wrapping

The values of curvelet coefficients depend on how they are aligned in the real image. One can expect higher coefficient's values when the curvelet is accurately aligned to a given curve in an image. A clear explanation is provided in Figure 3-5. The curvelet named 'c' in the figure is almost perfectly aligned with the curved edge and therefore, has a higher coefficient value. Curvelets 'a' and 'b' will have coefficients close to zero as they are quite far from alignment with the curve (Guha and Wu 2010).

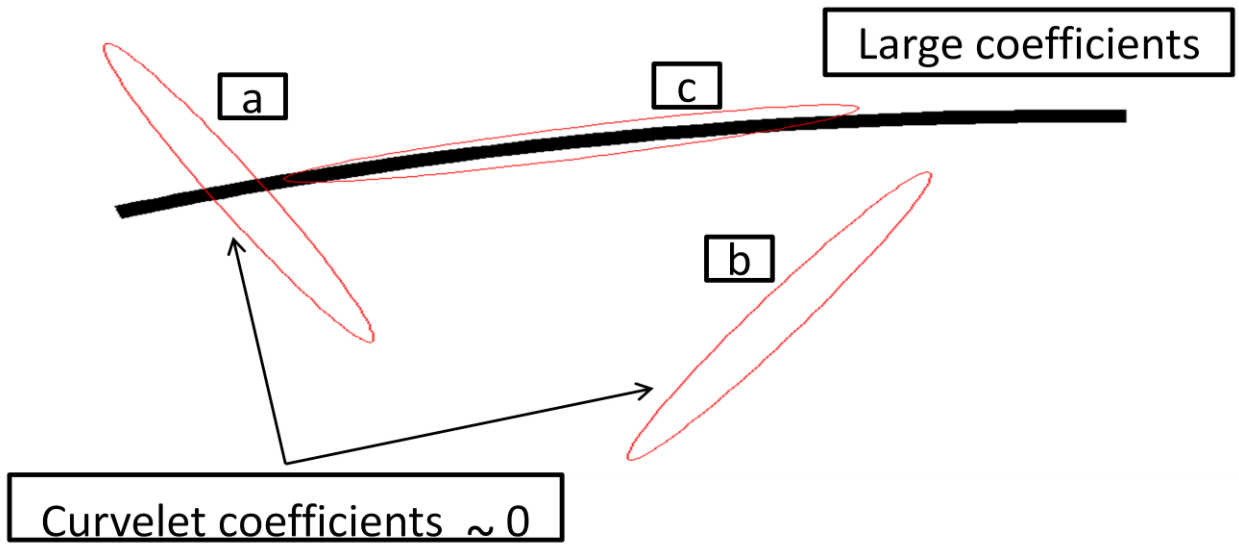

Figure 3-5 Alignment of curvelets along curved edges (Guha and Wu 2010)

From the previous discussion, it is clear that the curvelet transform provides a distinguished characteristic for the signals where they are better localized in both frequency and spatial domain compared to wavelet or any other transform. The unique mathematical property for representing curved singularities in a non-adaptive manner makes the Curvelet transform a higher-dimensional generalization of wavelets.

The major advantage of the curvelet transforms over the wavelet is that the edge discontinuity is better approximated by curvelets than wavelets. Curvelets can provide solutions to the limitations of wavelet transforms, which are:

- Limited curved singularity representation,
- Limited orientation (Vertical, Horizontal and Diagonal), and
- Absence of anisotropic element (isotropic scaling)

If an image function, f, is approximated by the largest m coefficients as $\hat{f}_m$, then the approximation errors are given by:

$$\left\| f - \hat{f}_m^F \right\|^2 \propto m^{\frac{-1}{2}}, m \to +\infty \qquad \text{Fourier transforms}$$

$$\left\| f - \hat{f}_m^W \right\|^2 \propto m^{-1}, m \to +\infty \qquad \text{Wavelet transforms}$$

$$\left\| f - \hat{f}_m^C \right\|^2 \propto m^{-2} \log(m^3), m \to +\infty \qquad \text{Curvelet transforms}$$

Figure 3-6 shows the edge representation capability of wavelet (left) and curvelet transform (right). More wavelets are required for an edge representation using the square shape of wavelets at each scale, compared with the number of required curvelets, which are of an elongated needle shape. The main idea here is that the edge discontinuity is better approximated by curvelets than

wavelets. Curvelets can provide solutions for the limitations (curved singularity representation, limited orientation and absence of anisotropic element) existing in the wavelet transform.

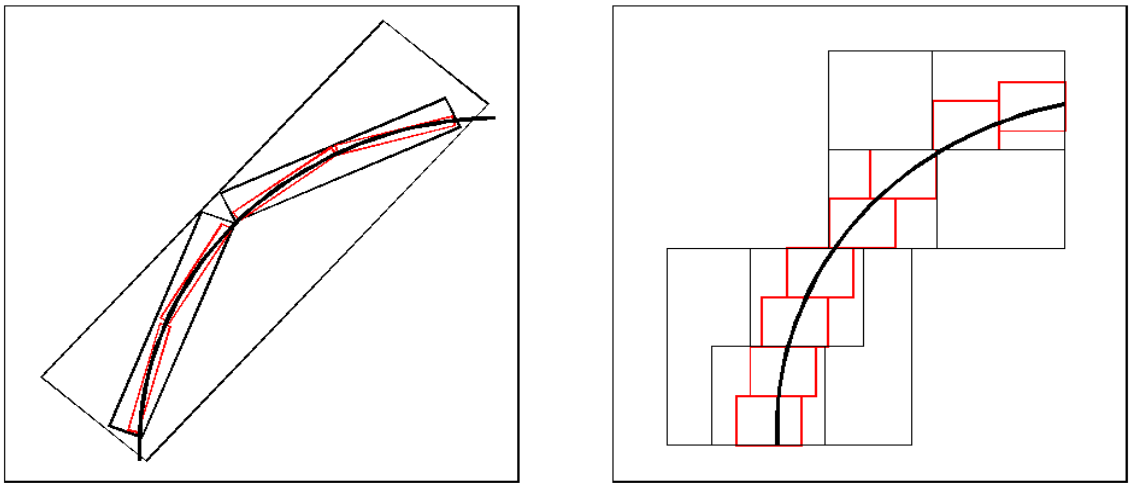

Figure 3-6 Representation of curved singularities using wavelets (right) and curvelets (left) after (Guha and Wu 2010).

3.4 Wavelet and edge detection

3.4.1 Wavelet image analysis and edge detection criteria

Multi-resolution techniques aim at transforming images into a representation where both spatial and frequency information can be identified (Livens et al. 1997). A wavelet transform decomposes images into a complete set of wavelet functions, which then form a basis, generally orthogonal. These functions are constructed by translating and dilating a single-mother wavelet which is localized in both spatial and frequency domain (Mallat 1989). Once this is completed in discrete steps, the discrete wavelet transform is obtained, for which there exists an efficient filtering implementation in the real space. Every wavelet corresponds to a high and low-pass filter. For the most common cases with dilations by a factor of two, the scheme is called "dyadic" wavelet transform and introduced in Figure 3-7, (Livens et al. 1997).

The procedure of decomposition in order to obtain the approximation, horizontal, vertical and diagonal details is as follows:

- **Approximation image (LL)**; convolving image rows by a one-dimensional low-pass filter (Lo-F), down-sampling of filtered signals to keep every other column, convolving the columns of resulting signals by another one-dimensional low-pass filter and down-sampling to keep every other row.
- **Horizontal detail image (H)**; convolving the image rows by one-dimensional low-pass filter, down sampling of filtered signals to keep one column out of two, convolving the columns of resulting signals by a high-pass filter (Hi-F) and keeping one row out of two.
- **Vertical detail image (V)**; performance of a high-pass filter on the original image followed by a low-pass filter with two down-sampling steps to keep every other column and row for each step respectively.
- **Diagonal detail image (D)**; in order to obtain the diagonal detail image, two high-pass filters with two steps of down sampling are carried out on the original image (Myint 2001; Daryaei 2003).

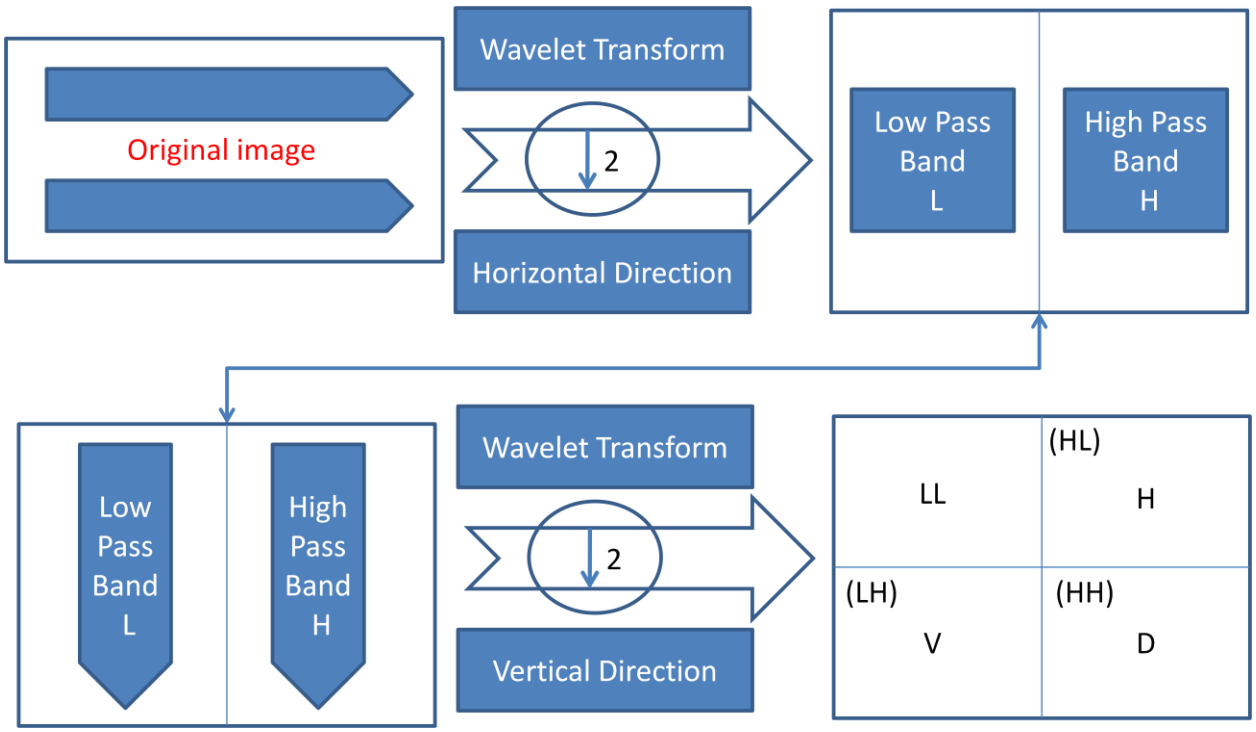

Figure 3-7 Example of wavelet transform for two-dimensional imagery, after (Tso and Mather 2009)

According to the above dyadic scale, if we take as an example a 256x256 pixels image, the resulting decomposed images will be eight images, representing the produced eight scales, and in two directions, the horizontal and vertical directions. At each scale level, the image is convolved with a 1-D wavelet to obtain the coefficients at that level vertically and horizontally.

Then the modulus maxima of the resulting images are calculated in each direction. In order to avoid plotting weak edges, only the maxima with a value above a certain threshold are taken and plotted.

3.4.2 Comparison with curvelet

Fourier's series require a large number of terms to reconstruct a discontinuity with acceptable accuracy. This is the well-known Gibbs phenomenon. Wavelets have the ability to solve the problem of Fourier's series as they are localized and multi-scaled. However, though wavelets do work well one-dimensionally, they fail to effectively represent higher-dimensional singularities (especially curved singularities, wavelets can handle point singularities quite well) due to limited orientation selectivity and isotropic scaling. Standard orthogonal wavelet transform has wavelets with primarily vertical, horizontal and diagonal orientations independent of scale.

Curvelet transform has drawn much attention lately because it can efficiently handle several important problems, while the traditional multi-scale transforms like wavelet fail. First, Curvelets can provide a sparse representation of the objects that exhibit 'curve punctuated smoothness', (Candes and Donoho 2004) i.e. objects that are smooth except along a general curve with bounded curvature. Curvelets can model such curved discontinuities so well that the representation becomes as sparse as if the object were not singular. From Figure 3-6, we identify the sparsity and efficiency of curvelet representation of curved singularities compared to wavelets. At any scale j, curvelets provide a sparse representation $O(2^{j/2})$ of the images compared to wavelets' $O(2^j)$.

3.5 Canny edge detector

Canny edge detection is an optimal method for **step edges'** detection in the spatial domain. Canny uses three criteria to design his edge detector. First, a reliable detection of edges with low probability of missing true edges, and a low probability of detecting false edges must be achieved. Second, the detected edges should have a minimum distance to the true location along the edge. Third, there should be only one response to a single edge (thin lines for edges).

Based on these criteria, the Canny edge detector first **smoothes** the image to eliminate any noise, then it finds the **image gradient** to highlight regions with high derivatives. The regions with high derivatives are tracked by the algorithm to suppress any pixel that is not at the maximum (non-maximum suppression). The remaining pixels are further reduced by two thresholds T1 and T2. If the magnitude is below T1, it is set to zero (none edge), if the magnitude is above T2, it is made an edge. And if the magnitude is between the two thresholds, then it is set to zero unless there is a path from this pixel to a pixel with a gradient above T2 (Canny 1986).

Step 1: Gaussian filtering to remove noise

The first step of canny edge detection is to filter out any noise in the original image before trying to locate and detect any edges. The Gaussian filter is used to blur and remove unwanted detail and noise. By calculating a suitable 5 X 5 mask, Gaussian smoothing can be performed using the standard convolution method. The larger the width of the Gaussian mask, the lower the detector's sensitivity to noise. By increasing the standard deviation the intensity of the noise is either reduced or blurred. An example of 2D Isotropic Gaussian equation is given below:

$$G(x,y) = \frac{1}{2\pi\sigma^2} e^{-\frac{x^2+y^2}{2\sigma^2}} \qquad \textbf{3-10}$$

Step 2: Gradient calculation

After smoothing the image and eliminating the noise, the next step is to find the edge strength by taking the gradient of the image –there are many ways and masks to perform the gradient calculation. One of these ways is to find the difference between the intensity value of the two consecutive pixels in both directions (x and y). When finding edges, we are looking for the

steepest descent as well as the steepest ascent since both represent a high change in the intensity of the image. Figure 3-8 depicts the gradient and orientation process.

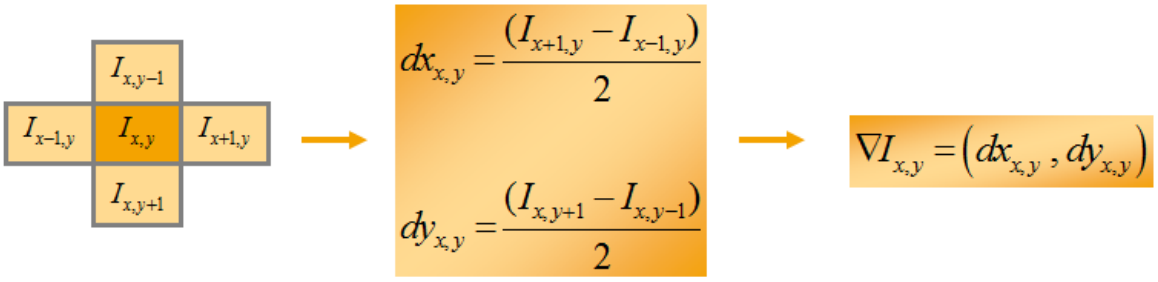

Figure 3-8 Illustration of gradient calculation in canny operator

Once we have the gradient value for each pixel we can get the **magnitude** of the gradient by:

$$|\nabla I_{x,y}| = \sqrt{(dx_{x,y})^2 + (dy_{x,y})^2} \qquad \textbf{3-11}$$

The main purpose of doing this is to highlight regions with high spatial derivatives. The **orientation** of the edge can be determined by the next equation:

$$\theta = arctan\left(\frac{dy_{x,y}}{dx_{x,y}}\right) \qquad \textbf{3-12}$$

Step 3: Non-Maximal Suppression

This step works with the magnitude and orientation of the gradient of the pixel under consideration and creates one pixel-width edge. However, we need to interpolate the values of

the pixels found at the neighborhood around the point under analysis. The pixel that has no local maximum gradient magnitude is now eliminated and the comparison is made between the actual pixel and its neighbors along the direction of the gradient as in Figure 3-9.

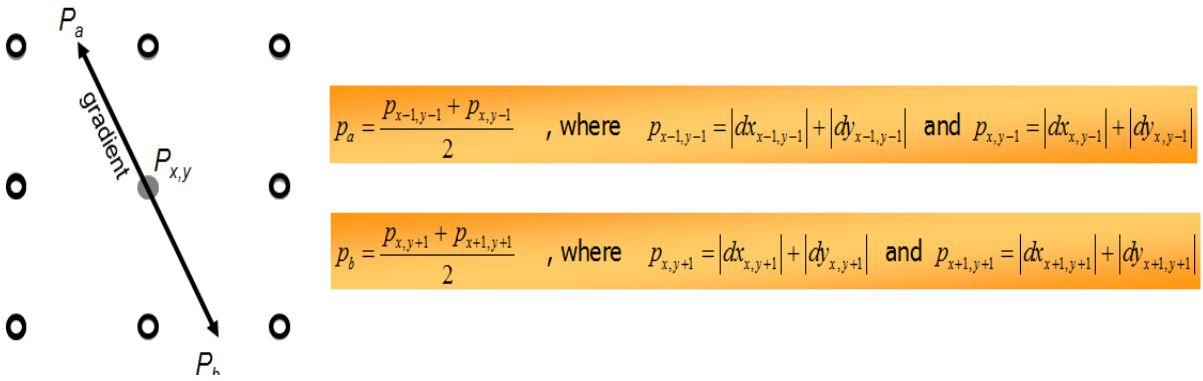

Figure 3-9 Non Maximal Suppression Procedure

Step 4: Hysteresis

The problem now is that we may have some pixels that, despite being a local maximum, represent noise. At this stage, most of the edge detectors apply a threshold process. The threshold is then defined so that each pixel with a value below it is eliminated. Two levels of thresholding are selected: high threshold (TH) and low threshold (TL). For a given pixel, if the gradient magnitude is below TL, it is unconditionally set to zero. If the gradient is at least TH, the pixel is left alone. And finally, if the gradient is between these two thresholds, then it is set to zero unless there is a path from this pixel to a pixel with a gradient above TH. An example is in Figure 3-10.

TL=0.2 TH=0.6 TL=0.4 TH=0.8

Figure 3-10 applying hysteresis to Canny edge map
(www.cs.washington.edu/research/imagedatabase/demo/edge)

Table 3-2 summarizes a comparison between curvelet, wavelet and canny operator.

Table 3-2 Comparison between wavelet, curvelet and Canny

	Wavelet	***Curvelet***	***Canny***
Scale	Isotropic	Anisotropic	N/A
Directionality	Limited (vertical, horizontal and diagonal)	Multi directional (through wedges)	According to the calculated direction from the gradient value
Edge detection	Handle point singularity quite well, but fail to represent higher dimensional singularities (curved singularity)	Handle both point and smooth curves quite well	Depends on the thresholds values
Processing time (512X512) Pixel	0.76 (s)	2 (s)	1.07 (s)
Criteria	The maxima of the wavelet transform modulus	Curvelet, which most fit the curves, have the higher coefficient values	Gradient calculation followed by non-maxima suppression and hysteresis

3.6 Implementation of the edge detection techniques for high-resolution satellite imagery

The influence of edge detection process comes from the fact that it is usually lies at the bottom of the classification process to serve as a base map for all other coming modules. Consequently, the more accurate this process, the more accurate the whole classification results are.

In this section, edge detection results using curvelet, wavelet and Canny operator will be compared. Figure 3-11, illustrates the proposed algorithm for edge detection using curvelet transform with some pre-processing steps. The pre-processing steps involve data fusion between the multispectral bands with 2.00 m resolution with the panchromatic band with 0.5 m resolution. The resulting image will be a multi spectral image with 8-bands. The next step is to convert the RGB image to gray level image using the standard perceptual weightings for the three-color components RGB using the equation 3-13, (www.mathworks.com/help/toolbox/wavelet/gs/f4-1013594.html).

After that, a high-pass filter is applied, and the resulting image will be added to the original image as in Figure 3-12.

$$Gray\ level = 0.2990 * R + 0.5870 * G + 0.1140 * B \qquad \textbf{3-13}$$

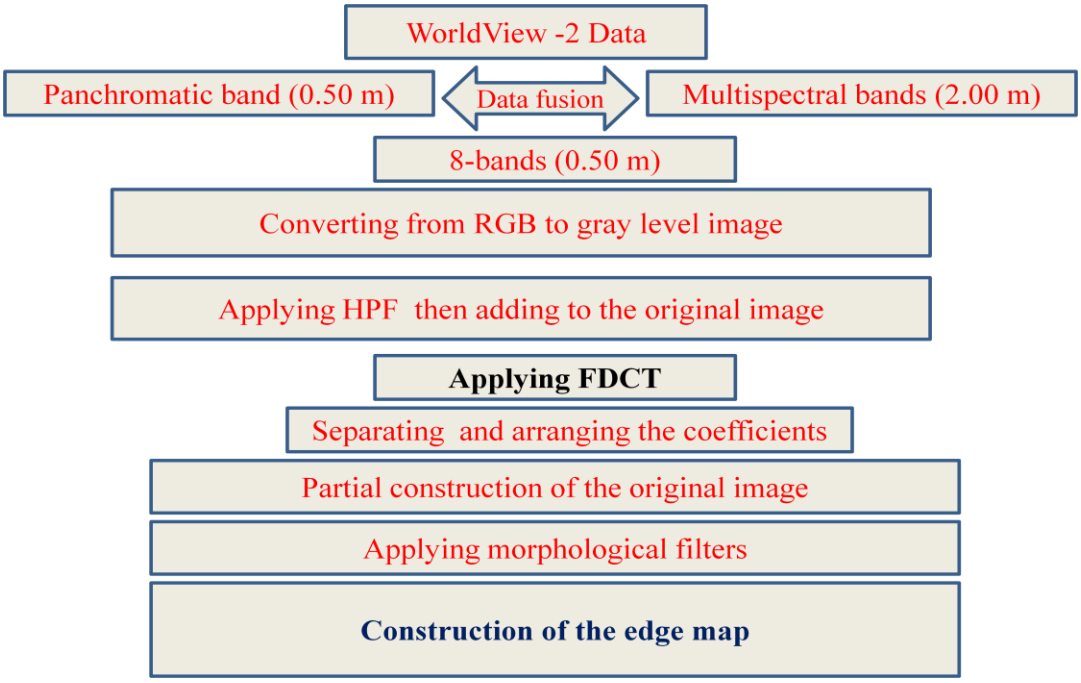

Figure 3-11 Edge detection technique using curvelet transform (Elhabiby et al. 2012)

Figure 3-12 The grey level image after high pass results added to the original image

The 2D FFT of the output image is then calculated to obtain Fourier's samples. And according to the size of the original image, the scale levels are determined by using:

$$n=\log_2(N)-3 \qquad \textbf{3-14}$$

Where N is the minimum number of the image size and n is the number of the scale levels, i.e. for N=512 pixels, n=6 levels. These scale levels are divided into three parts, which are coarse level, detail level and fine level. Then curvelet transform is applied to extract the coefficients from these parts. Images are then reconstructed for each level with those coefficients as shown in Figure 3-13.

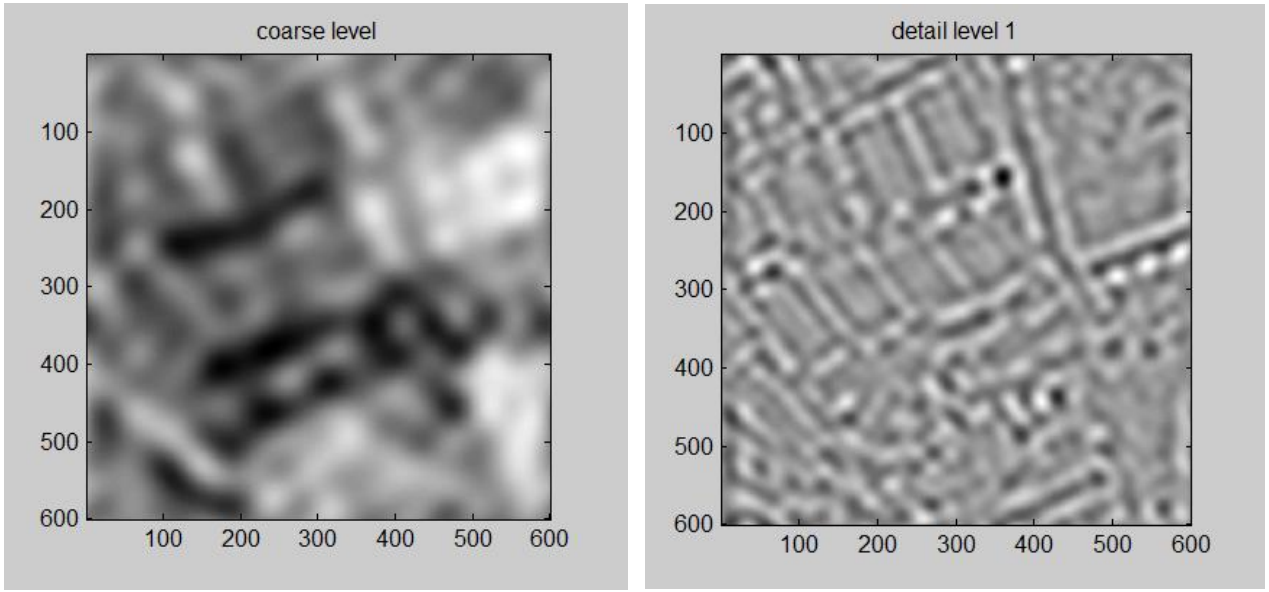

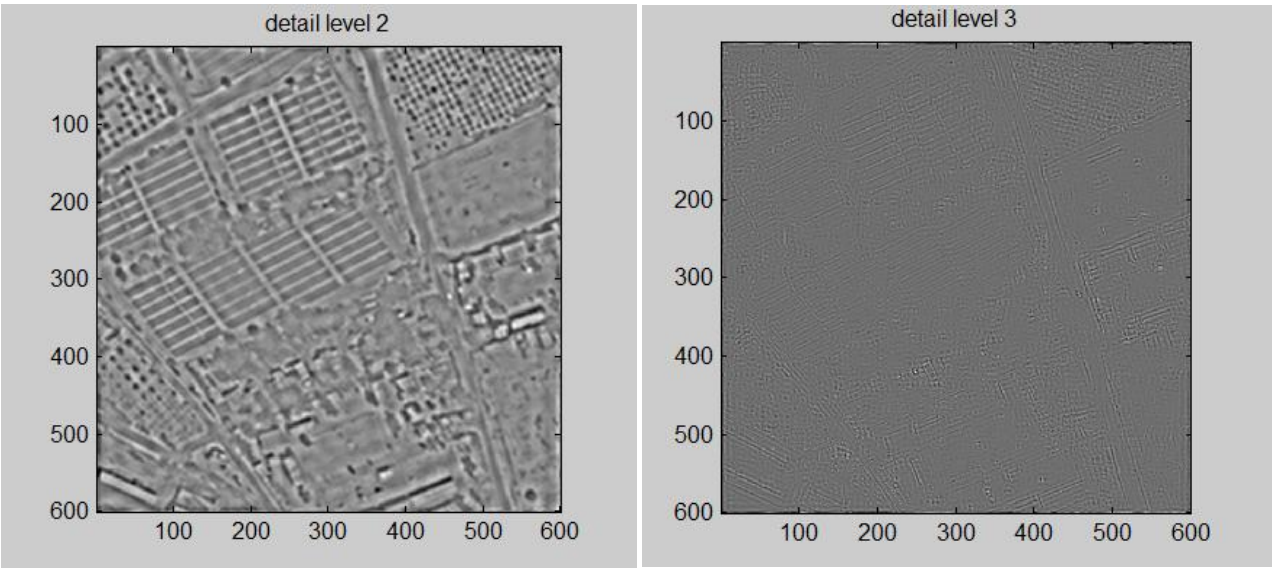

Figure 3-13 The reconstructed images using different scales levels

Analyzing the curvelet transform coefficients, it can be found that they contain different information in each scale level. Consequently, by arranging the coefficients of each level and take the most significant part of them, this will enhance the edge information that represents the image part of interest. Then, the coefficients are reconstructed to get a new image called the edge map, as shown in Figure 3-14, where the edge parts are enhanced.

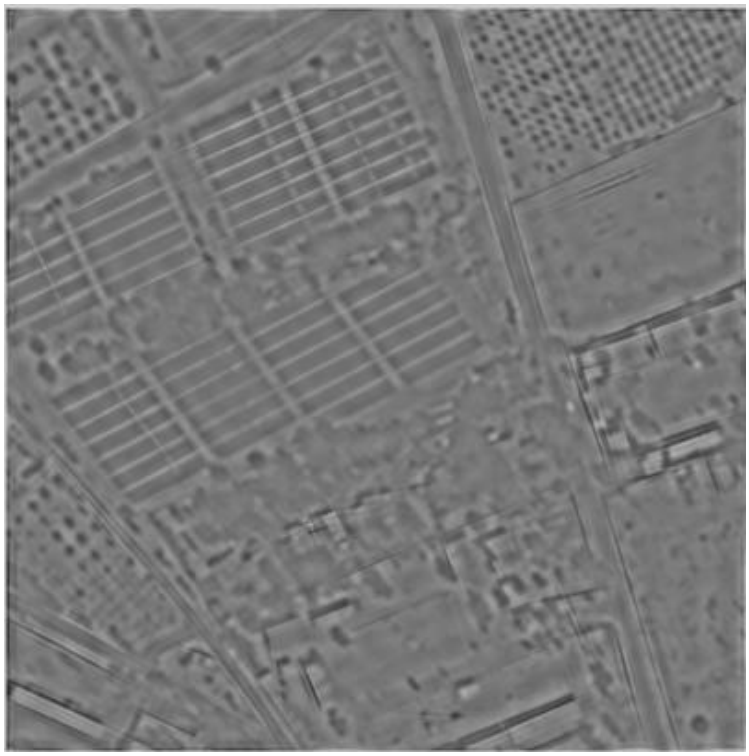

Figure 3-14 The reconstructed edge map

Table 3-3 summarizes the total number of coefficients in each scale and the actual used percentage.

Table 3-3 The percentage used in reconstructing the edge map image

Scale	*No. of total coefficients*	*Percentage used*	*No. of used coefficients*
1	625	0%	0
2	8320	0%	0
3	32032	100%	32032
4	124064	100%	124064
5	491264	1%	4912

6	1944856	1%	19448
Total	2601161	6.9 %	180456

The edge map is then thresholded to get enhanced edge map as shown in Figure 3-15. The reconstructed edge image was thresholded based on the fact that any edge will have abrupt changes in the pixel from negative towards positive values, and the absolute summation will determine the strength or the weakness of that particular edge.

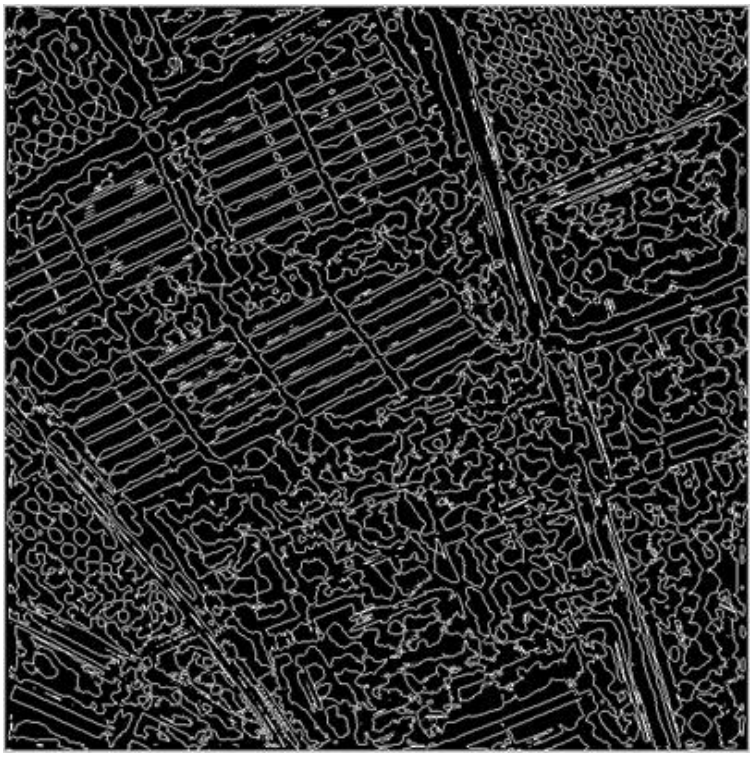

Figure 3-15 The thresholded edge map

Figure 3-16, demonstrates the impact of the thresholding process on the criteria of selecting edges. For instance, two points on both sides of a strong edge with indices' values +5.503 and -5.43 respectively, while the same figure (down) illustrates two points on the sides of a weak edge

having the values of -26.35 and -21 respectively, this is why first point will be considered as an edge while second point is not.

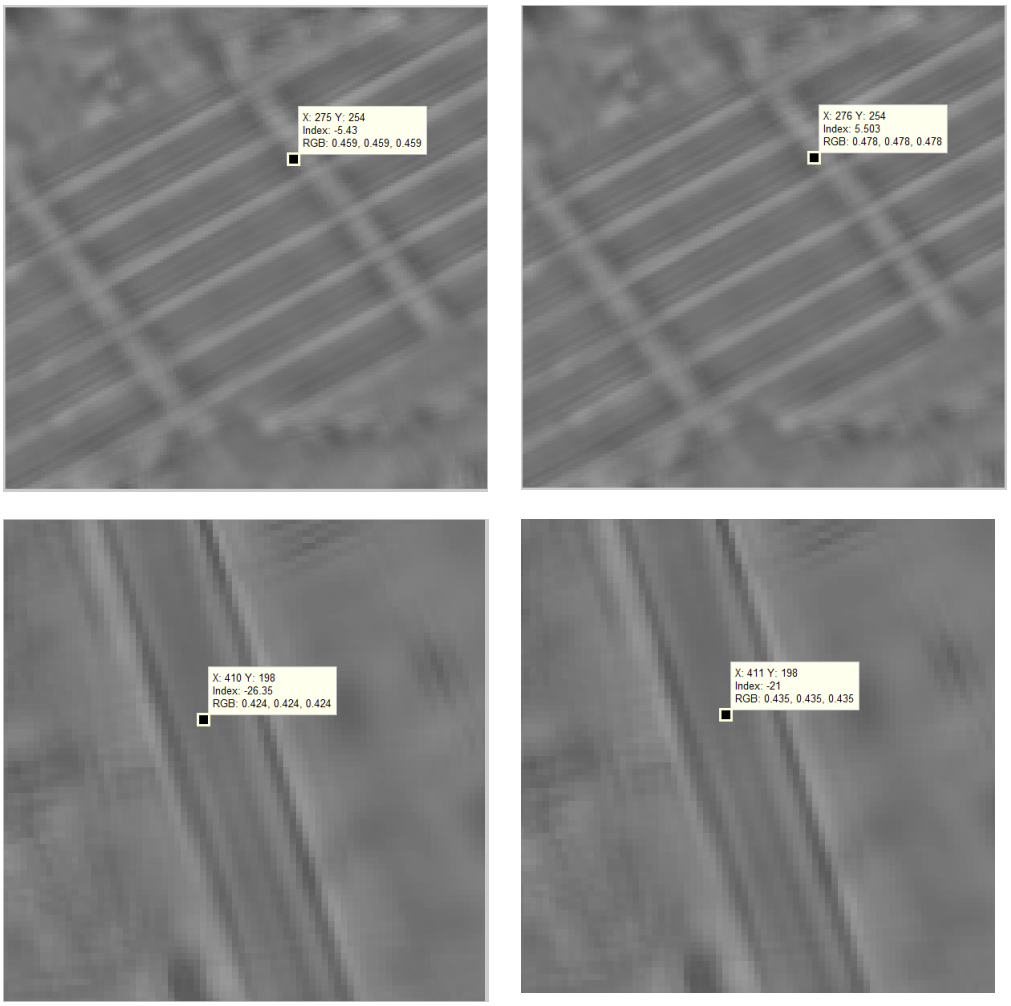

Figure 3-16 An example of the thresholding criteria

The next step is applying morphological filters to get rid of undesired artifacts, i.e. isolated pixels below certain threshold, and the result is shown in Figure 3-17.

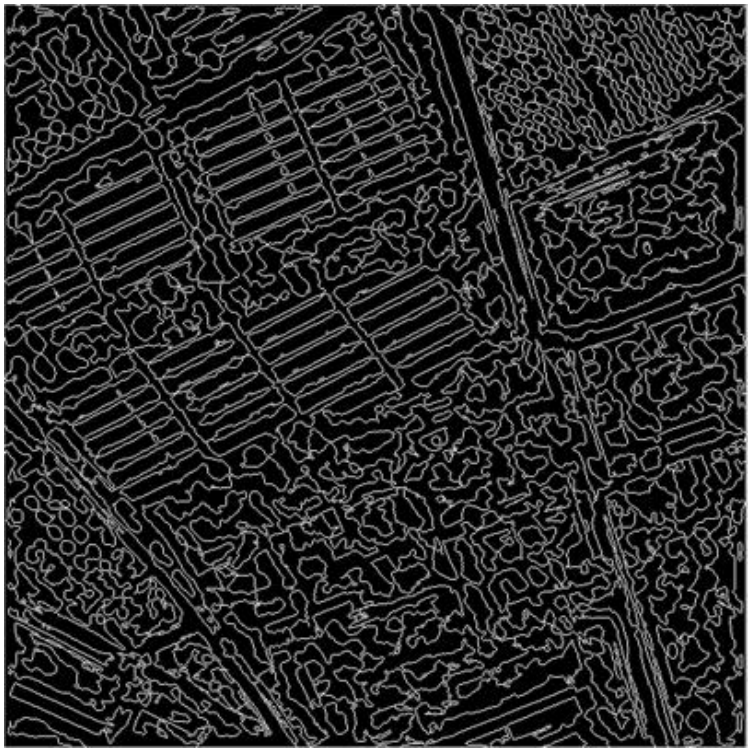

Figure 3-17 Final edge map after morphological filters

To illustrate the quality of this algorithm compared to Canny and wavelet transforms, the procedure was repeated using these two methods and the final results are shownin Figure 3-18 and Figure 3-19. Canny was used with sigma equal to 1 and the thresholds T1= 0.006 and T2= 0.02.

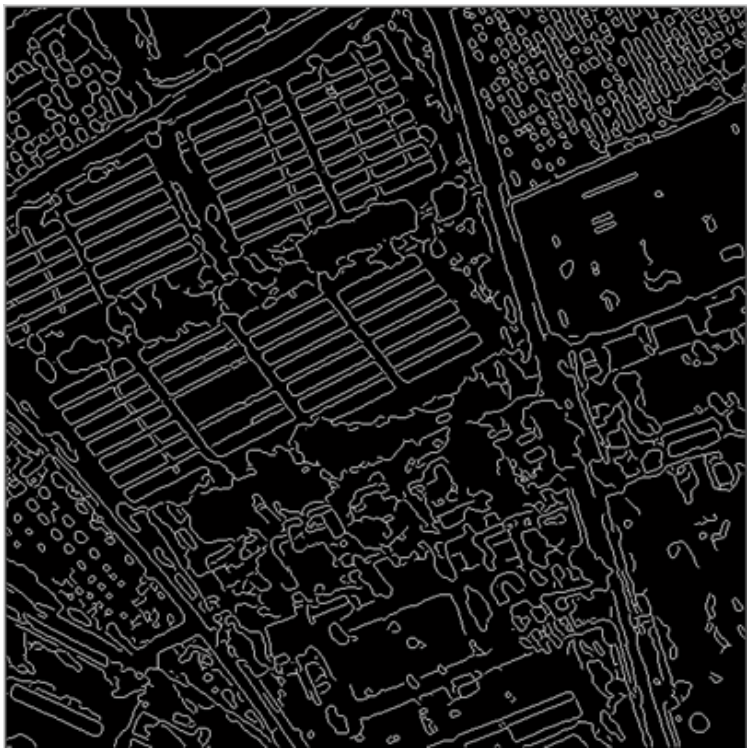

Figure 3-18 Final edge map with Canny Operator

Figure 3-19 Final edge map with Wavelet transforms

The result of Canny shows almost identical result with the curvelet transforms edge detection result. The case was different with the wavelet as in the Figure 3-19, which illustrates the edge detection result when using the original image as an input to the wavelet transforms.

A tiny area in the original image, Figure 3-12, was picked and enlarged to emphasize the potentials of using the curvelet transform as an edge detector against Canny and wavelet transform. Figure 3-20, highlights a small area in both Curvelet (left) and Canny edge map (right) overlaid on the original image. It is very clear that Canny wasn't able to siege or block many features leaving a lot of open boundaries, e.g. see the cricked areas in the Canny edge map, while curvelet gave the most accurate delineation of the edges better than the Canny.

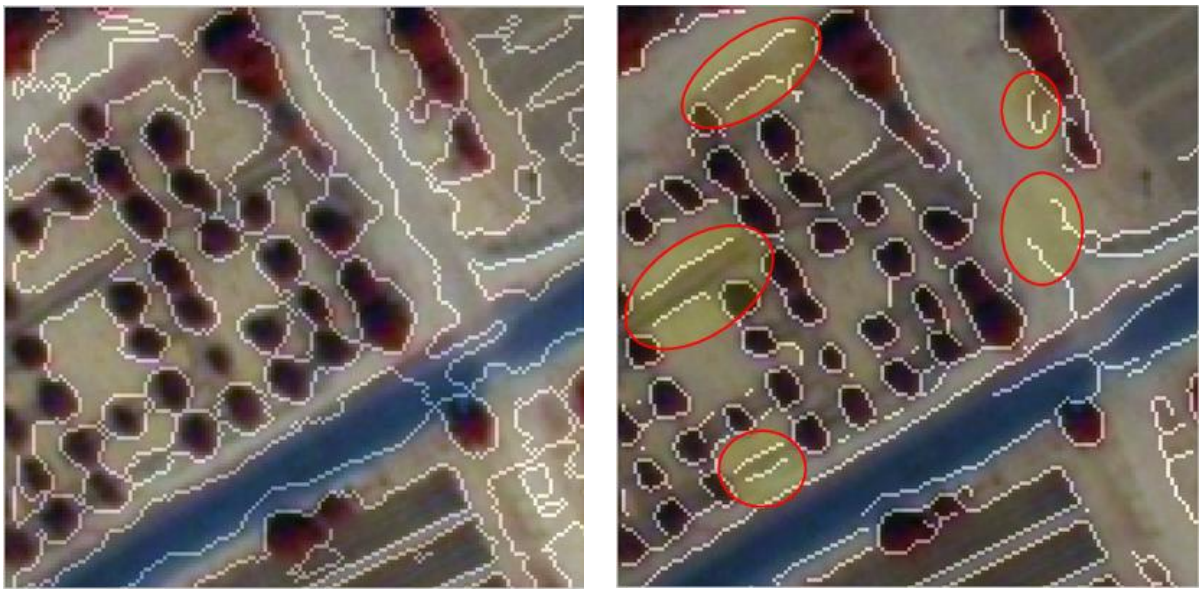

Figure 3-20 Highlight a certain area in curvelet (left) and Canny (right) images

In chapter four and five more results and detailed discussions for each of the previous techniques will be given.

3.7 Curvelet-Canny approach for edge detection

In this section, a new approach using the capability of the second generation curvelet transform together with the traditional Canny operator for edge detection from high-resolution satellite imagery; the combined technique will be applied on WorldView-2 imagery. First, the curvelet coefficients will be generated in multi-scales and multi-directions using a forward discrete curvelet algorithm. Then, these coefficients will be sorted in each scale to generate the edge map using the larger coefficients for the coarser scales. Second, this edge map will be the input to the second stage where the three main steps of the traditional canny operator, gradient calculation, non-maximal suppression and hysteresis, will be applied. The first step results in removing noise, fine edges, from the image aiding the second step for better connecting the strong edges without the effect of weak edges coming from the noise.

The percentage of the utilised coefficients in the curvelet transforms step together with the weight for each scale are the tuning parameters the user has to adjust to getting the desired level of edges detected. The results from the proposed approach were compared to the traditional canny edge detection algorithm. The results showed very good potentials for detecting elongated edges and also for generating more closed objects, which make this method a good alternative for the segmentation step for any further object-based classification algorithm.

3.7.1 Methodology

Figure 3-21, illustrates the proposed algorithm for edge detection using curvelet transforms and canny operator with some pre-processing steps.

The data is WorldView-2 imagery, provided by Digital Globe Company for a part of San Francisco, USA. The imagery was captured on October, 2011 morning time. Second generation curvelet transform wrapping algorithm will be applied to the gray level image, Figure 3-22,

resulting in generating of the curvelet coefficients in different scales and orientations. The coarser level starts from scale number one and gets finer as we move to the second , third fourth scales.

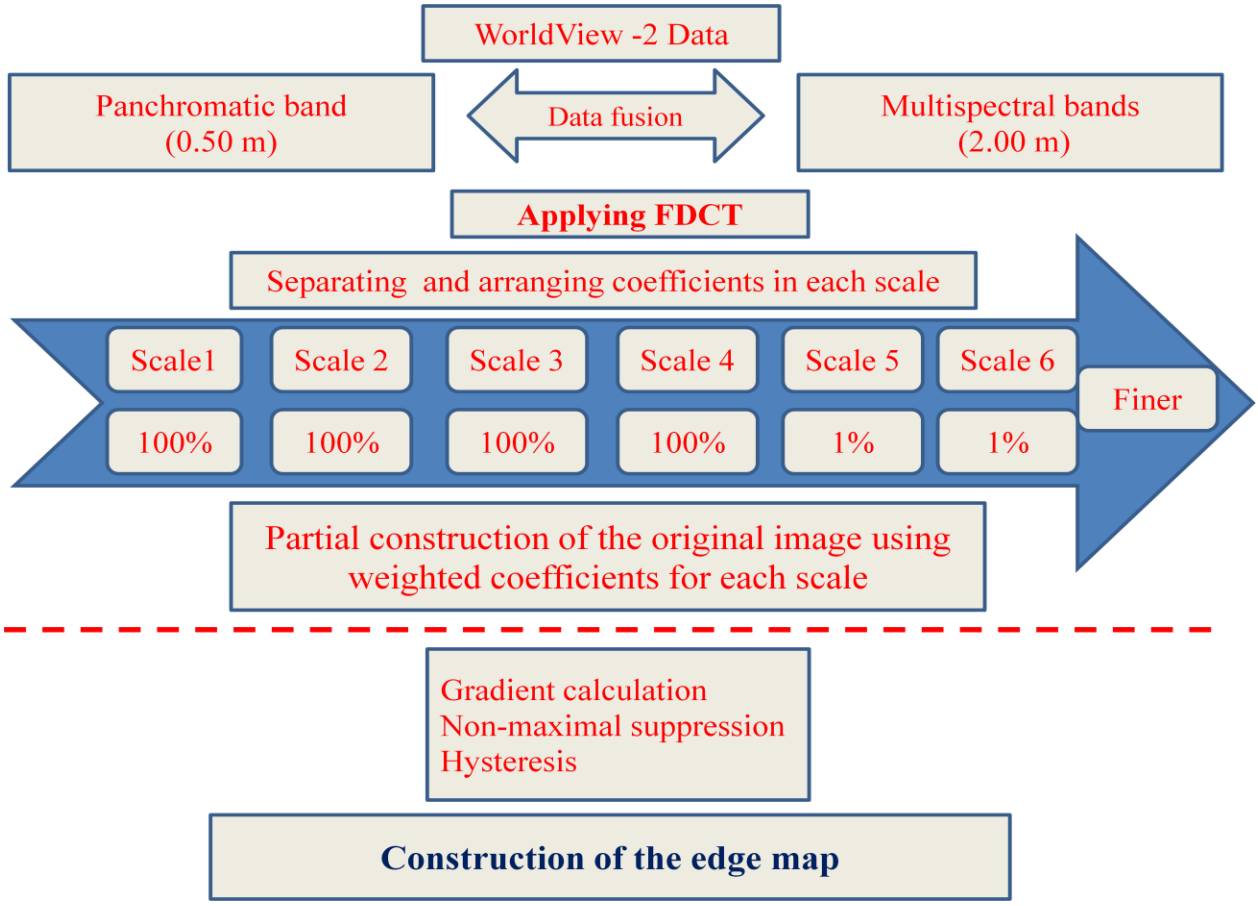

Figure 3-21 The proposed edge detection technique using curvelet-canny

Figure 3-22 The grey level image for the area of the study

Reconstructing the images from each scale individually shows that coarser scales, first four scales, contain the most important information about the image, while finer scales, fifth and sixth scales mostly contain noise or very fine details about the image, as in Figure 3-23. Therefore, the main purpose of this step is to suppress the coefficients coming from the finer scales, as a result the reconstructed image will be partially free from insignificant information, noise and very fine details, to help the next step for better detecting the strong edges. Consequently, by arranging the coefficients of each level and take the most significant part of them, this will enhance the edge information that represents the image part of interest. Then, the coefficients are reconstructed to get a new image called the edge map (Elsharkawy et al. 2011), as shown in Figure 3-24, where the edge parts are enhanced.

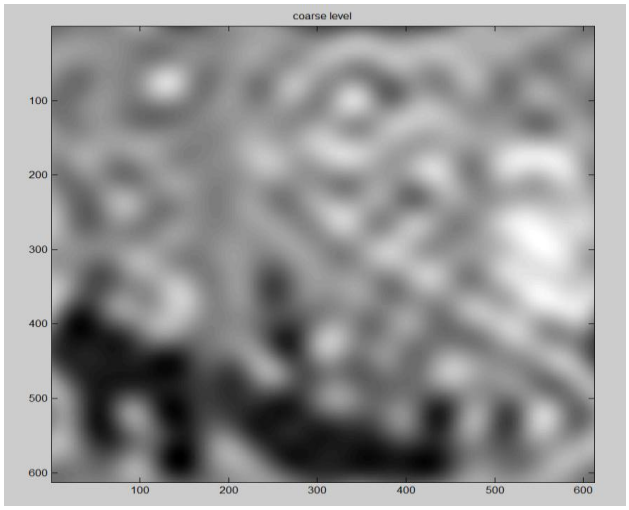

Coarse Level

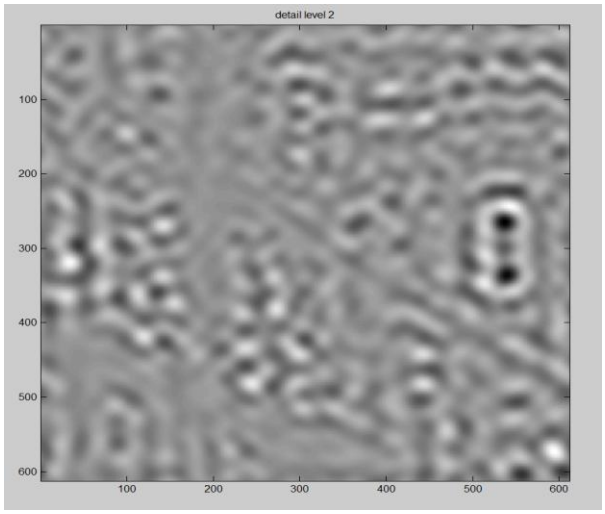

Detail Level 2

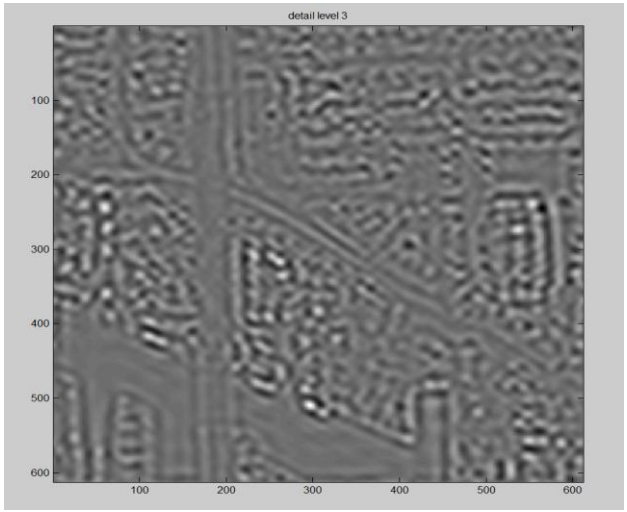

Detail Level 3

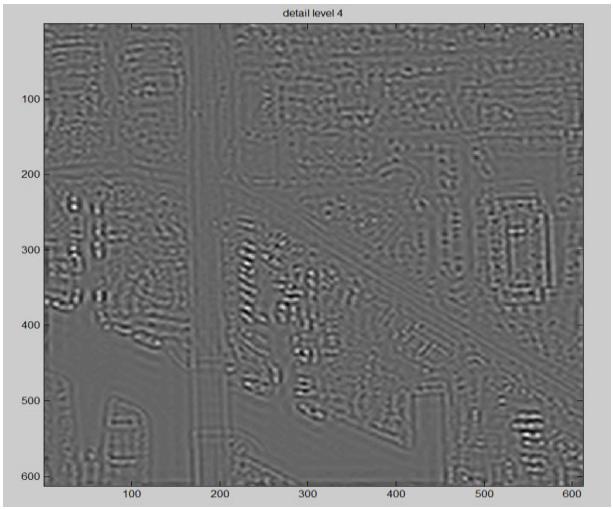

Detail Level 4

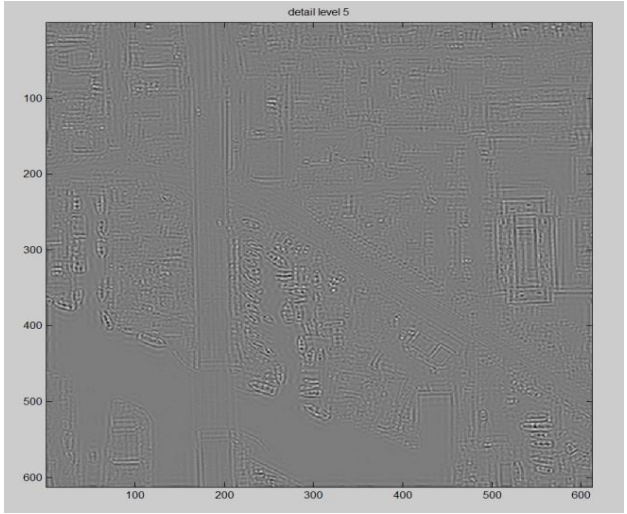

Detail Level 5

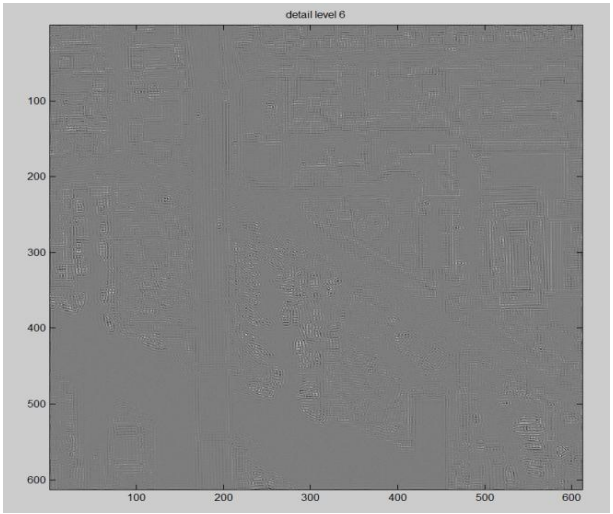

Detail Level 6

Figure 3-23 The reconstructed images using different scales levels

Figure 3-24 The reconstructed edge map

Table 3-4, summarizes the total number of coefficient in each scale and the weight of each scale level used to reconstruct the edge map.

Table 3-4 the percentage used in reconstructing the edge map image

Scale	*No. of total coefficients*	*Percentage used*	*No. of used coefficients*	*Weight of each scale level*
1	625	100%	625	1
2	8320	100%	8320	1
3	33488	100%	33488	1
4	129792	100%	129792	1

5	510848	1%	5108	0.9
6	2022976	1%	20229	0.9
Total	2706049	7.3 %	197562	

The reconstructed edge map, Figure 3-24, will be the input to the next step, which includes gradient calculation, non-maximal suppression and hysteresis. The result from this stage is illustrated in Figure 3-25.

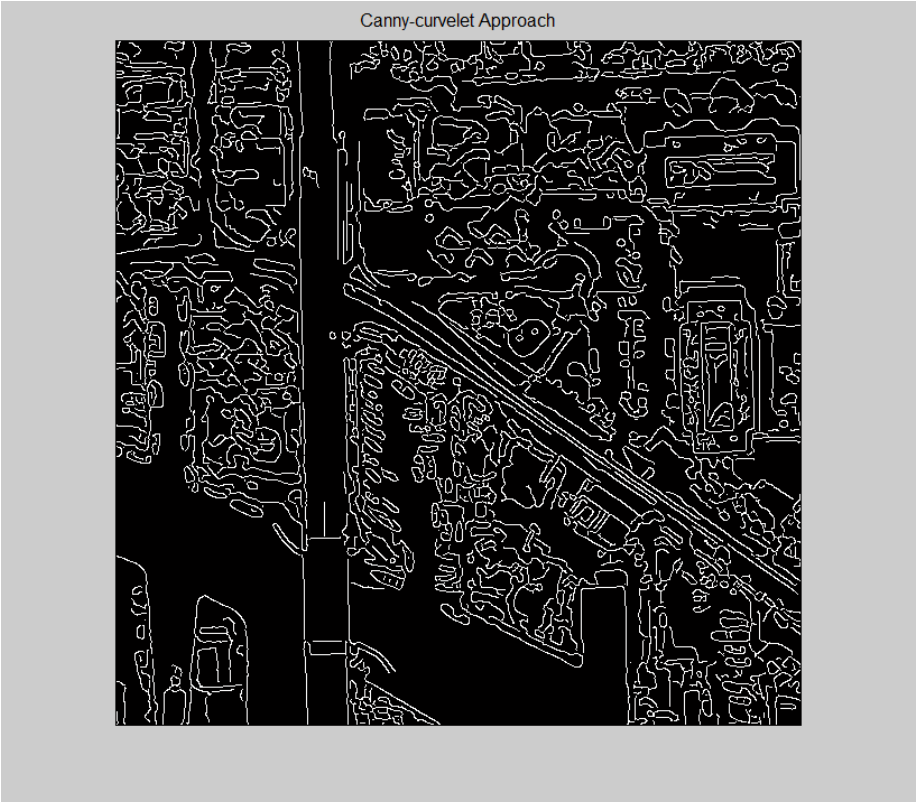

Figure 3-25 Edge detection result using the proposed algorithm

To illustrate the quality of this algorithm the result was compared with the traditional Canny, Figure 3-26. Details of the comparison are given in the next section.

Figure 3-26 Results with Canny Operator

3.7.2 Results and discussion of the curvelet-canny integration

Comparing the two figures, it was clear that Canny wasn't able to siege or block many features leaving a lot of open boundaries, and also canny alone, was not able to detect many elongated structures, while curvelet-canny approach gave better results regarding more detection of elongated structures and more closed boundaries. Figure 3-27, enlarge some snapshots to illustrate these findings.

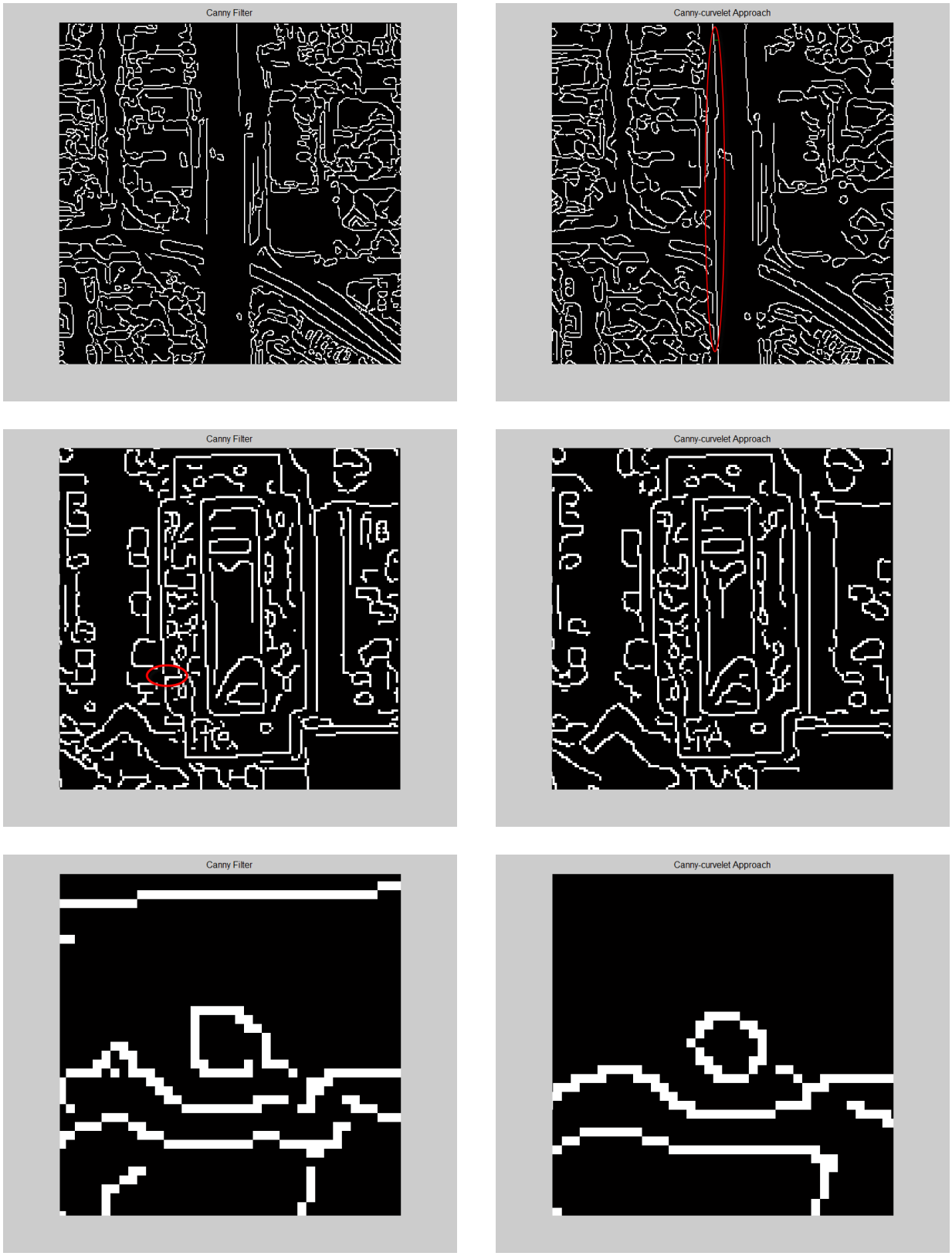

Figure 3-27 Comparing certain areas in curvelet-canny and canny

Chapter Four: **Urban Classification**

4.1 Introduction

In this chapter, urban classification problem will be tackled using the advantages of the WorldView-2 imagery. First, a new multi-layer classification algorithm is introduced in section 4.2, using the will known NDVI ratio and two other innovated NDVI like ratios. The new algorithm targets six common classes which can be found in most urban classification scales; vegetation, water, asphalt roads, bare soil, shadow and buildings. Second, curvelet transform will be introduced, in section 4.3, as a feature extraction technique for building extraction. Third, the integration between the aforementioned two approaches is introduced in section 4.4.

4.2 Land cover classification: pixel-based approach

4.2.1 Area of study

The study area is part of the whole area of study, previously described in chapter two. It is mainly a residential area, comprises scattered buildings, roads, vegetation areas, shadowed areas, shoreline and water body. The data was provided by Digital Globe, the images were captured on April 7th, 2011 in morning time. Figure 4-1, illustrates a false color composite, NIR-1, G and B, of the study area.

Figure 4-1 Area of study

4.2.2 Pixel-based Classification Algorithm

For the purpose of the study, two data sets will be generated from this imagery, as there is no IKONOS or QUICKBIRD data were available, one will be notified by (Data Set I), which comprises the full 8-bands, and the other will be notified by (Data Set II), in which the four new bands will be omitted and it will contain only the 3-visible bands and the NIR-1, as in the next figure.

Data set I	Data set II
C-B	
B	B
G	G
Y	
R	R
R-E	
NIR-1	NIR-1
NIR-2	

Figure 4-2 Data set used

As described in the radiometric calibration section, section 2.3.3, a conversion to radiance followed by a conversion to reflectance takes place for the original DN's values.

To get the most gain of the spatial resolution capability of the WorldView-2 data, a fusion technique has to be applied. The proposed algorithm begins with a data fusion between the panchromatic band of the WorldView-2 data, 0.50 m, and the multispectral ones, 2.00 m resolution, to generate 8-spectral bands with a resolution of 0.50 m. One of the most common fusion techniques is the Brovey Transform. This technique is optimum when increase in contrast in the low and high ends of an images histogram (i.e., to provide contrast in shadows, water, and high reflectance areas such as urban features) is needed. The procedure of this transform starts with multiplying each Multi-Spectral, MS, band by the high-resolution Panchromatic, PAN, band, and then divides each product by the sum of the MS bands. Since the Brovey Transform is intended to produce RGB images, only three bands at a time should be merged from the input multispectral scene (Nikolakopoulos 2008) in our case we choose NIR-1, Green and Blue bands.

The study uses two different methods for extracting land cover information, namely;

1) Supervised classification approach using the Maximum Likelihood Classifier,

2) Image classification using multi-layer classification tree analysis.

In the following sections the details of these methods will be demonstrated.

4.2.3 Supervised classification approach using the Maximum Likelihood Classifier

For the purpose of applying Maximum Likelihood Classifier, training pixels for six classes; asphalt roads, vegetation, Bright surface, red roofs, shadow, water and bare soil, were chosen for the two data sets (I, II). Table 2 summarizes the number of pixels used for training and verification for each class.

Table 4-1 Training and verification pixels summary

Class name	*Training pixels No.*	*Validation pixels No.*	*Total*
Asphalt roads	3798	3484	7282
Vegetation	6984	2936	9920
Bright surface	4280	4726	9006
Red roofs,	2710	1551	4261
Shadow	1278	934	2212
Water	23467	3823	27290
Bare soil	5872	783	6655
Total	48389	18237	66626

The classification results were compared with the validation pixels, as ground truth data, to assess the overall accuracy. The error matrix was generated to obtain the user's and producer's accuracy (Congalton 1991). The user's accuracy refers to the measure of commission errors that correspond to those pixels from other classes that the classifier has labeled as belonging to the class of interest. Moreover, the producer's accuracy refers to the measure of omission errors that

correspond to those pixels belonging to a class of interest that the classifier didn't recognize (Richards and Jia 2006; Bhaskaran et al. 2010).

4.2.3.1 Evaluation of Training Sets

In order to evaluate certain training data sets against specific classes it is common to run statistical measures of distances between two signatures for all possible combination of bands that is used in the classification. This process will help us to rule out any bands that are not useful in the results of the classification. In remote sensing literature, the most popular separability measures are the separability indices; namely, divergence, transformed divergence, Bhattacharyya distance and Jeffries-Matusita distance (Kavzoglu and Mather 2000). For instance, one of the most popular separability measures, divergence, is computed using the mean and variance-covariance matrices of the data representing feature classes. While, the transformed divergence measure, the one we used in this research paper, can be considered as the standardized form of divergence as it scales the divergence values to a certain range, 0 to 2 here. Generally, pairs with values greater than 1.9 indicate that the ROI pairs have good separability. Separability of the training pixels for all possible combinations was calculated for the 2 data sets and the results were as in the figure 5. The formula for computing the divergence (D_{ij}) is as follows:

$$D_{ij} = \frac{1}{2} tr\left(\left(C_i - C_j\right)\left(C_i^{-1} - C_j^{-1}\right)\right) + \frac{1}{2} tr(\left(C_i^{-1} - C_j^{-1}\right)\left(\mu_i - \mu_j\right)\left(\mu_i - \mu_j\right)^T) \qquad \textbf{4-1}$$

Where:

i and *j* are the two signatures (classes) being compared

C_i is the covariance matrix of signature *i*

μ_i is the mean vector of signature *i*

tr is the trace function (matrix algebra)

T is the transposition function

And the formula for computing the transformed divergence (TD_{ij}) is as follows:

$$TD_{ij} = 2000(1 - exp\left(\frac{-D_{ij}}{8}\right)) \quad \textbf{4-2}$$

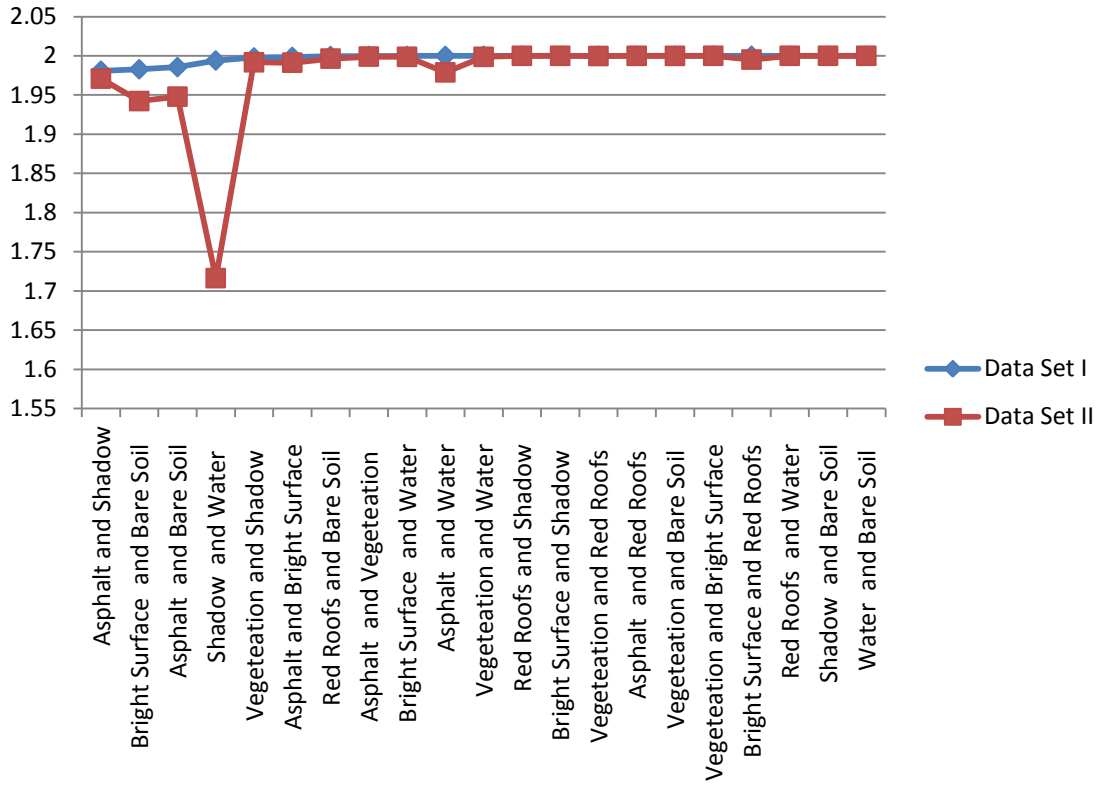

Figure 4-3 Separability values for all possible pairs for the 2 data sets

4.2.4 Supervised classification approach using the new band ratios

The traditional NDVI ratio plus two new band ratios are introduced, the original NDVI (R1) specially suited for vegetation and water, second one (R2) to detect asphalt, shadow and man-

made objects and finally (R3) to detect red roofs, buildings and barren. Table 4-2, summarizes the three ratios and their usage. Note that we flipped the original NDVI, equation 2-10, by subtracting the reflectance values of the visible band minus the reflectance values of the near-infrared values divided by the summation of the two values as in Table 4-2.

Table 4-2 Band ratios and their implementation

	Band ratio	*Target classes*
R1	$\frac{\rho_R - \rho_{NIR1}}{\rho_R + \rho_{NIR1}}$	Vegetation Water
R2	$\frac{\rho_C - \rho_R}{\rho_C + \rho_R}$	Asphalt Shadow Manmade object
R3	$\frac{\rho_{NIR1} - \rho_Y}{\rho_{NIR1} + \rho_Y}$	Red roof Building Barren

R1 is applied twice to separate between water and vegetation classes, and then R2 is applied to detect asphalt, shadow and red roofs are detected through lower and upper thresholds, finally the R3 ratio is applied to detect bright surfaces below certain threshold. Figure 2-14, summarize these steps along with the applied thresholds.

4.2.5 Classification Results

4.2.5.1 Supervised classification results using MLC

Data set I:

Classification results were evaluated using validation pixels as shown in Table 4-1. Table 4-3, summarizes the confusion matrix of the data set I against the verification pixels, the overall Accuracy was 99.3% and the Kappa Coefficient was 0.9907.

Table 4-3 Confusion matrix for the data set I

	Asphalt	*Vegetation*	*Bright Surface*	*Red Roofs*	*Shadow*	*Water*	*Bare Soil*	*Total*
Asphalt	99.54	0.00	0.11	0.00	1.21	0.00	2.30	10.93
Vegetation	0.14	99.95	0.00	0.00	0.82	0.00	0.00	14.89
Bright Surface	0.25	0.04	99.13	0.00	0.43	0.01	1.38	13.52
Red Roofs	0.04	0.01	0.00	100.00	0.09	0.00	0.00	6.40
Shadow	0.00	0.00	0.00	0.00	95.75	0.01	0.00	3.32
Water	0.00	0.00	0.71	0.00	1.69	99.98	0.00	40.96
Bare Soil	0.03	0.00	0.04	0.00	0.00	0.00	96.32	9.99
Total	100.00	100.00	100.00	100.00	100.00	100.00	100.00	100.00

Data set II

Table 4-4, summarizes the confusion matrix of the data set II against the verification pixels, table 2, the overall Accuracy was 97.5280% and the Kappa Coefficient was 0.9679.

Table 4-4 Confusion matrix for the data set II

	Asphalt	Vegetation	Bright Surface	Red Roofs	Shadow	Water	Bare Soil	Total
Asphalt	99.51	0.00	0.09	0.00	0.87	0.30	2.25	11.03
Vegetation	0.14	99.98	0.00	0.00	1.26	0.03	0.00	14.92
Bright Surface	0.25	0.01	98.62	0.35	0.13	0.15	2.04	13.58
Red Roofs	0.07	0.01	0.00	99.65	0.00	0.00	0.01	6.37
Shadow	0.00	0.00	0.00	0.00	93.37	3.28	0.00	4.57
Water	0.00	0.00	0.57	0.00	4.38	96.25	0.00	39.51
Bare Soil	0.03	0.00	0.73	0.00	0.00	0.00	95.70	10.02
Total	100.00	100.00	100.00	100.00	100.00	100.00	100.00	100.00

Figure 4-4, Figure 4-5 and Figure 4-6, illustrate the classification results for the data sets and the user's and producer's accuracy comparisons respectively.

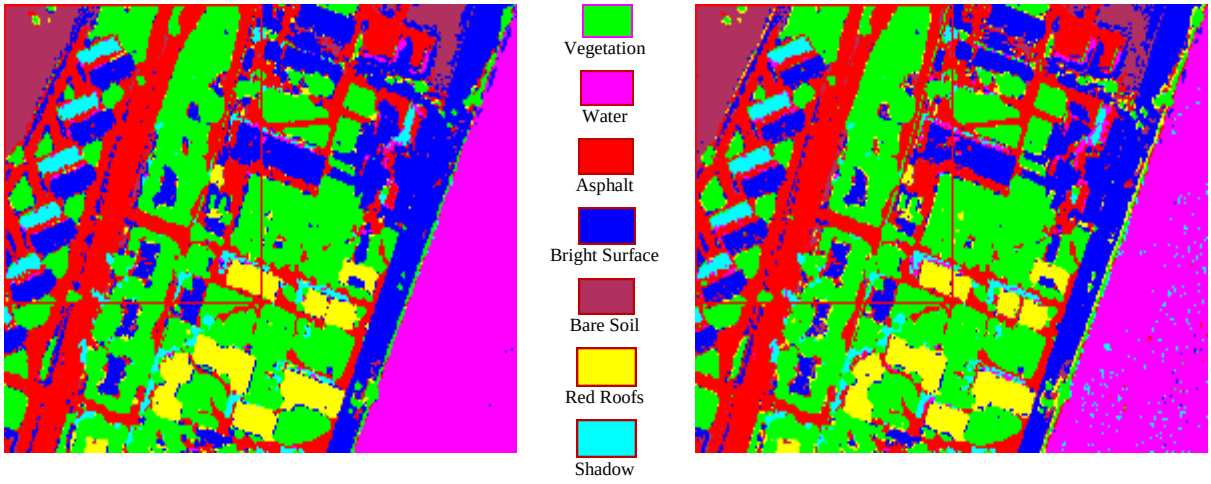

MLC results for Data I MLC results for Data II

Figure 4-4 supervised classification results for the two data set

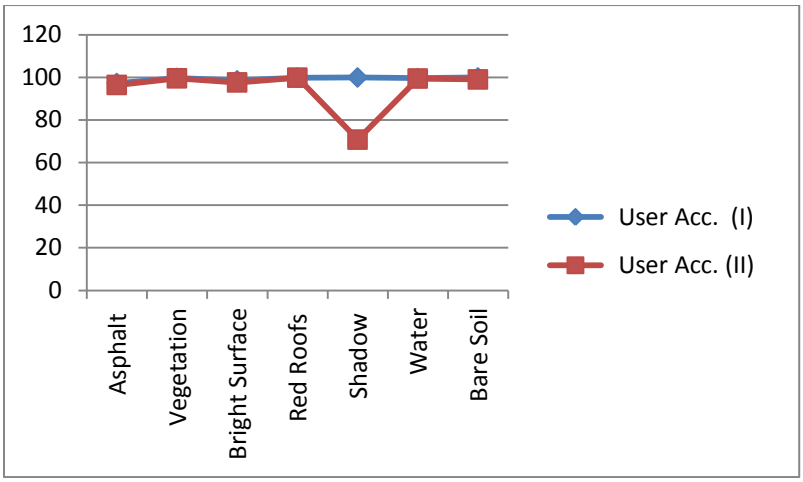

Figure 4-5 User's accuracy comparison for the two data sets

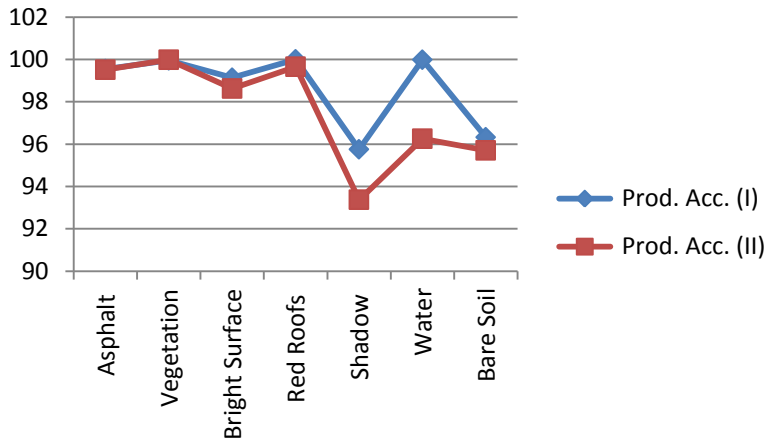

Figure 4-6 Producer's accuracy comparison for the two data sets

4.2.5.2 Supervised classification results using band ratios

Applying the band ratios in the shown sequence as in Figure 2-14, showed good results. Water, vegetation, manmade objects and shadow were all successfully classified using the 3 band ratios without any spatial attributes, in which it will give a good solution for those who need fast and reliable land cover types. The original image and the classified image are shown in Figure 4-7 and **Error! Reference source not found.** respectively.

As a result of lack of ground truth and for assessment purposes, a ground truth map was generated to the same scene in the ENVI software using MLC, utilising more than 50% of the image as a training pixels. The original image, the ground truth image and the classified image using the proposed algorithm are shown in Figure 4-7, 4-8 and **Error! Reference source not found.** respectively.

Figure 4-7 Area of study

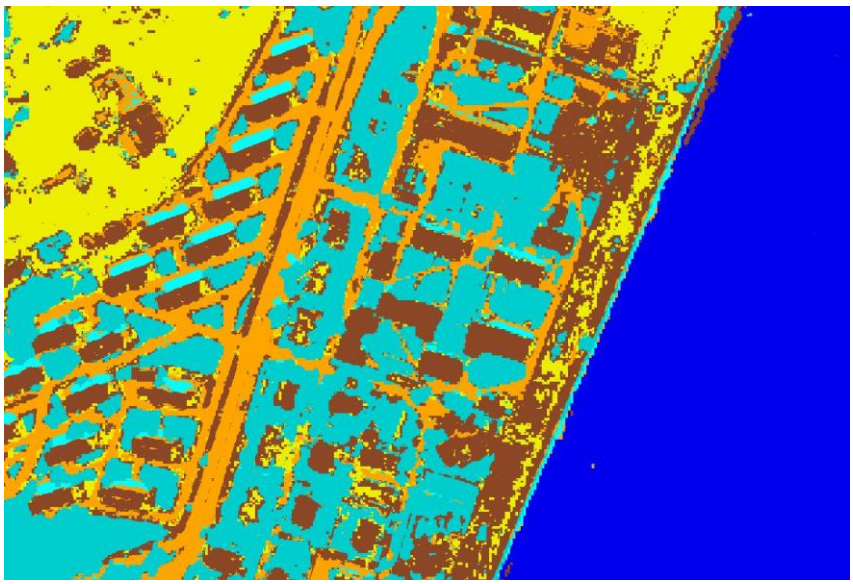

Bare soil Asphalt Vegetation

Shadow Water Buildings

Figure 4-8 Ground truth map

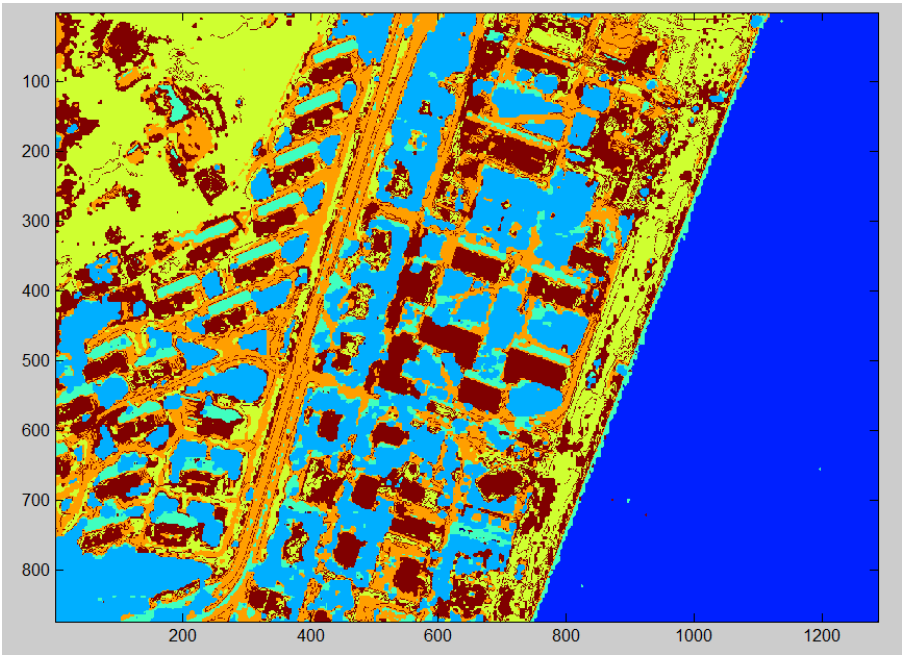

Bare soil Asphalt Vegetation

Shadow Water Buildings

Figure 4-9 Classification results for the proposed band ratios

The confusion matrix between the generated ground truth and the classified image is tabulated in the following table.

Table 4-5 Confusion matrix for the multi-layer algorithm results compared to the generated ground truth

	Bare soil	**Veg.**	**Buildings**	**Shadow**	**Asphalt**	**Water**	**User's Accuracy**	**Producer's Accuracy**
Bare soil	60	0	35	0	5	0	60	74
Veg.	0	99	1	0	0	0	99	74
Buildings	15	5	66	0	13	0	66	56
Shadow	0	45	2	33	19	0	33	87
Asphalt	4	16	21	1	58	0	58	70
Water	0	0	1	0	0	99	100	100

4.2.6 Analysis of the classification results

For the first approach, MLC, visual inspection showed better results for the data set I than the data set II. Statistically, both the overall accuracy and kappa coefficients were enhanced by 3% higher, than those of data set II. Consequently, user's and producer's accuracy were higher for data set I relative to data set II for all classes as shown in Figure 4-5 and Figure 4-6. Even for the separability analysis the 8-band combination gives better separability measures for all class combinations comparing to the 4-band combination as in Figure 4-3.

Regarding the multi-layer classification approach, applying the band ratios in the shown sequence in Figure 2-14, results in good delineation of vegetation, asphalt, shadow, water, red

roofs and bright surfaces. Visual inspection of the generated ground truth shows that building class was greatly confused with bare soil class; also the shadow class was mixed with the vegetation class. Even though, the producer's accuracy for almost all classes was greater than 70% except for the buildings class it was 60%. And the user's accuracy was almost 100% for water and vegetation classes, while it has less percentage for the other classes due to the aforementioned confusion between classes. The new bands, namely C, Y, Red edge and NIR2 showed very good potentials for detecting manmade objects and vegetation as well.

In order to enhance the overall classification result, the buildings class will be targeted in the next two sections, 4.3 and 4.4.

4.3 Building extraction

The process of automatic extraction of buildings from digital imagery has a major practical importance in the areas of data acquisition and updating of geographic information system (GIS) databases. This process also involves a number of scientific challenges for researchers as a result of the heterogeneous nature of the buildings, especially in the developing countries (Aytekin et al. 2009).

Several techniques are used in building extraction from satellite images. In this section, second generation curvelet transform will be introduced as an edge detection tool for detecting of buildings boundaries. Second generation curvelet transform provides optimally sparse representations of objects, which display smoothness except for discontinuity along the curve with bounded curvature (Candes et al. 2006). Some papers have investigated this technique for edge detection from high resolution satellite imagery such as IKONOS or QuickBird, and microscopic imagery (Xiao et al. 2008; Geback and Koumoutsakos 2009; Zhenghai and

Jianxiong 2009; Guha and Wu 2010), which clearly show a great potential of using curvelet transform in solving edge detection problems. However, to-date there is no researches to tackle the building detection problem using the curvelet transform from high resolution satellite imagery.

In this section an algorithm for building detection based on curvelet transform will be introduced. The algorithm consists of four main parts; first data fusion between the panchromatic band, 0.50 m resolution, and the multispectral ones, 2.00 m resolution, to generate 8-spectral bands with a resolution of 0.50 m. Second, a Gaussian high pass filter is applied to enhance the edges. Third, using the curvelet transform edges will be detected depending on the fact that the values of curvelet coefficients are determined by how they are aligned in the real image. The more accurately a curvelet is aligned with a given curve in an image, the higher is its coefficient value. Fourth, a filling process for every closed boundary followed by calculation of statistics for these enclosed boundaries; such as area, major and minor axis and compactness to extract the buildings (Elsharkawy et al. 2011).

The difficulty of implementing an automatic building extraction technique comes from the heterogonous nature of the buildings, where buildings have different shapes and sizes. Furthermore, the buildings may be occluded by shadows or by taller buildings. Moreover, the diverse materials used for the top roofs play an important role in this heterogeneity as these materials could have a similar texture and spectral properties with the surrounding objects, which make the segmentation process very difficult (Yanfeng et al. 2004). Consequently to overcome all these difficulties, there are many trials and proposed methods to solve building extraction problem using different approaches. (Mayer 1999), and (Braun et al. 1995) provide a good review about the different approaches related to automatic building extrication problem, while

(Matsuyama et al. 1990) provides an overview of the whole detection and photo interpretation problem.

There are a number of challenges when addressing the problem of building extraction. The first is related to how buildings are presented in imagery? Roofs as seen from above have a wide spectral diversity, from colored roof tiles, to metal roofs which may be confused with surrounding objects such as roads or parking lots or even bare soil. The second, what are the significant shape characteristics for buildings? Roofs have a wide variety in shape and in size. They can differ in shape from rectangular to circular, small family houses to larger industry buildings. In general, buildings if compared to other classes such as trees, cars or any other man-made objects can be considered a quite larger in size. Third, what is the role of contextual information?, the answer here points toward the shadow problem, as buildings in general are higher than its surrounding so in most cases they have shadows. Many researchers considered shadows as an important evidence for detecting building, see (Yanfeng et al. 2004) for example. One more important character about buildings is that they are generally not covered by water or vegetation. Finally, how the ancillary data be employed? this will be through providing a Digital Surface Model (DSM) for the study area, which may be the only way to detect building from surrounding areas in some cases. These data may be generated from stereoscopic imagery for the study area or directly from LIDAR data. These questions summarize the problem of building extraction from high resolution satellite imagery and also show the need of a new algorithm that can help in having an efficient automation for building extraction.

Following (Mayer 1999) in his surveying for building extraction, (Ünsalan and Boyer 2011) update this survey by adding missing and new papers published after this survey. Generally the

building extraction systems can be classified based on their **complexity in data**, **complexity in building model**, and the **system strategy** used (Ünsalan and Boyer 2011).

- Data complexity deals with the image types, some used satellite images (such as Landsat, SPOT, and IRS) with resolutions ranging from 5 to 30 meter or high resolution satellite images (IKONOS, QUICKBIRD, WorldView-2) where spatial resolution approach the 50 cm. Others used aerial images with resolutions ranging from 0.3 up to 1 meter. Complexity in building model deals with the relative location and orientation of the buildings and the complexity of the scene (tall trees- shadows- different material types of roof construction). Some have used even ancillary data such as Digital Elevation Map (DEM) or Digital Surface Model (DSM) data. Finally, some have used Synthetic Aperture Radar (SAR) images. Each of these representations has its own benefits and shortcomings (Ünsalan and Boyer 2011).
- Model complexity simply represent the building model used wether it is 2-D rectangle, a 2D polynomial, or a 3D surface. The choice of the building model is characterized by the type of input data and the type of application where the results will be used.
- System strategy captures the complexity of the system. This strategy may range from simple classification rules to more complex Bayesian networks, and graph-theoretical methods.

After 1999, several commercial satellites with high-resolution imaging capability were launched and being increasingly employed for large-scale topographic mapping, and especially for updating databases (Grigillo and Fras 2011). Few researches utilized high resolution satellite images in building extraction without the help of ancillary data, (Grigillo and Fras 2011) for instance used GeoEye-1 images with 0.5 m resolution for building detection using supervised

classification and region growing technique to get the building extracted, the authors recommended using DSM for better results. Also, (Wei et al. 2004) used Panchromatic QUICKBIRD images for building extraction using unsupervised clustering and Hough transform for edge detection. The authors indicated that the quality of detection relies heavily on the quality of segmentation or the clustering process. From this discussion it is quite clear the lack of research in this area. This research mainly focus on building detection from high resolution satellite images without any ancillary date using the enhanced capability of the WorldView-2 in its spectral and spatial resolution and the large covering area to work as a standalone sensor for building extraction.

4.3.1 Study area

The study area is part of the image previously described in chapter two. The study area includes well structured urban area comprises small family houses, shadows, trees, grass area and part of asphalt road. The images were captured on April 7th, 2011 in morning time. Figure 4-10, illustrates a false color composite, NIR-1, R and Y, of the study area.

Figure 4-10 Area of study

The choice of this 3-band combination is coming from the calculation of the Optimum Index Factor of the WorldView-2 data. Optimum Index Factor (OIF) is a statistical value that can be utilized to choose the best combination of three bands in a satellite image(Jensen 1994). The optimum combination of bands out of all possible 3-band combinations is the one with the highest amount of information, with the least amount of duplication. 4-3 describes how to calculate this index.

$$OIF = \frac{\sum_{k=1}^{3} S_k}{\sum_{j=1}^{3} Abs(r_j)} \qquad \textbf{4-3}$$

Where

S_k standard deviation of band-k

r_j correlation coefficient between any two bands

Standard deviation and correlation coefficients for all bands were calculated and all possible combinations were computed, the results are listed in Table 4-6, arranged from the greater value to the smaller one.

Table 4-6 OIF for all possible combinations

No.	*Band combination*	*OIF*	*No.*	*Band combination*	*OIF*	*No.*	*Band combination*	*OIF*
1	178	28.42393	**19**	358	24.8232	**37**	238	20.85876
2	378	26.64355	**20**	567	24.67987	**38**	345	20.3925
3	457	26.36094	**21**	678	24.44914	**39**	256	19.94141
4	458	26.05515	**22**	368	24.41157	**40**	127	19.9052
5	278	25.8133	**23**	267	23.6883	**41**	246	19.86977
6	467	25.76912	**24**	247	23.60386	**42**	128	19.6042
7	157	25.5563	**25**	258	23.3367	**43**	145	19.57658
8	147	25.4897	**26**	248	23.3282	**44**	245	18.75718
9	168	25.3997	**27**	268	23.2565	**45**	136	18.7019
10	158	25.31879	**28**	456	23.0016	**46**	236	17.54582
11	468	25.3023	**29**	137	22.7607	**47**	135	17.0053
12	148	25.24069	**30**	138	22.517	**48**	134	16.7669
13	347	25.161	**31**	257	22.0375	**49**	235	16.11067
14	357	25.08621	**32**	356	21.59818	**50**	126	16.0153
15	568	25.01004	**33**	346	21.5813	**51**	234	15.92579
16	348	24.89036	**34**	156	21.35826	**52**	125	14.3482

17	167	24.84341	**35**	146	21.22792	**53**	124	14.1125
18	367	24.83921	**36**	237	21.13095	**54**	123	11.2804

The third combination was chosen as it has high OIF and also gives very good visual separation between different land cover classes (vegetation, water, manmade objects …….).

4.3.2 Building Extraction Algorithm

Basic spectral information for mapping applications such as land-use surveys are essentially provided by the multispectral bands. However, as the limitation to the data storage volume and transmitting capability of the satellite, satellites do not collect high-resolution multispectral images directly. So, what happen is the sensor collects only one panchromatic band, wide range of spectrum, with higher spatial resolution and the rest of the bands, with narrower ranges of the spectrum, with lower resolution (Nikolakopoulos 2008). In case of WorldView-2, the panchromatic band volume is twice as the whole 8-spectral bands together. Considering these limitations, it is clear that effective image fusion techniques are the most effective solution for providing high-spatial-resolution and high-spectral-resolution images.

The proposed algorithm begins with a data fusion between the panchromatic band of the WorldView data, 0.50 m, and the multispectral ones, 2.00 m resolution, to generate 8-spectral bands with a resolution of 0.50 m. One of the most common fusion techniques is the Brovey Transform. This technique is optimum when contrast in shadows, water, and high reflectance areas such as urban features is needed. The procedure of this transform starts with multiplying each multi spectral band by the high-resolution panchromatic band, and then divides each product by the sum of the multi spectral bands. Since the Brovey Transform is intended to

produce RGB images, only three bands at a time should be merged from the input multispectral scene (Nikolakopoulos 2008) in our case we choose NIR-1, R and Y bands.

The next step is applying a Gaussian high pass filter to enhance the edges. Based on the curvelet transform theory, an implementation for detecting edges will be introduced depending on the fact that the values of curvelet coefficients are determined by how they are aligned in the real image. The more accurately a curvelet is aligned with a given curve in an image, the higher is its coefficient value. Analyzing these coefficients, it can be found that the coefficient in each scale level contains different information. Consequently, by arranging the coefficients of each level from the higher to the lower values and take the most significant part of them will enhance the edge information that represents the important part of the image to us. Then, the coefficients are reconstructed to get a new image where the edge parts are enhanced.

Morphological filters will be applied to remove the undesired noised pixels. After that, a filling process will be used to generate colored candidate parcels, in which buildings will be extracted from it in a final step.

The final step involves calculation of statistics for the enclosed boundaries; such as area, major and minor axis and solidity. Based on shape and area characteristics, buildings will be extracted from the candidate parcels. Figure 4-11, represent a schematic diagram of the aforementioned algorithm.

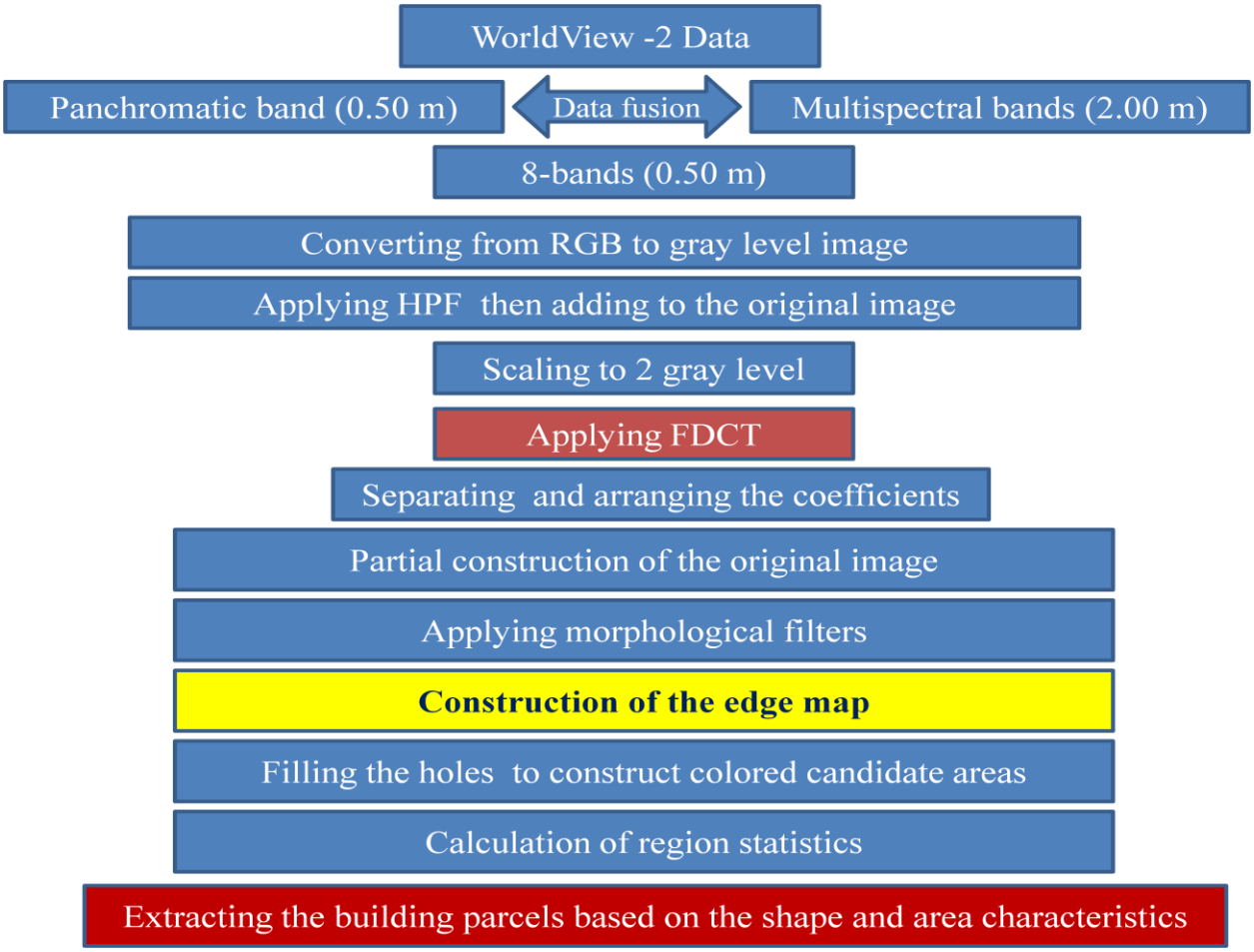

Figure 4-11 The proposed algorithm

4.3.3 Results of building extraction

The proposed algorithm will follow the described algorithm in chapter three for implementing curvelet transforms for edge detection. First, data fusion between the multispectral bands with 2.00 m resolution with the panchromatic band with 0.5 m resolution takes place. Then, the resulting image will be a multi spectral image with 8-bands. Second, a gray image will be generated using the equation 3-14.

After that a high pass filter is applied and the resulting image will be added to the original image as in Figure 4-12. Scaling the previous image to two pins only is an essential step to remove the

undesired noise and give more ability to the curvelet transform to detect the edges effectively, the result is in Figure 4-13.

Figure 4-12 The original image + high pass filter after converting to gray level image

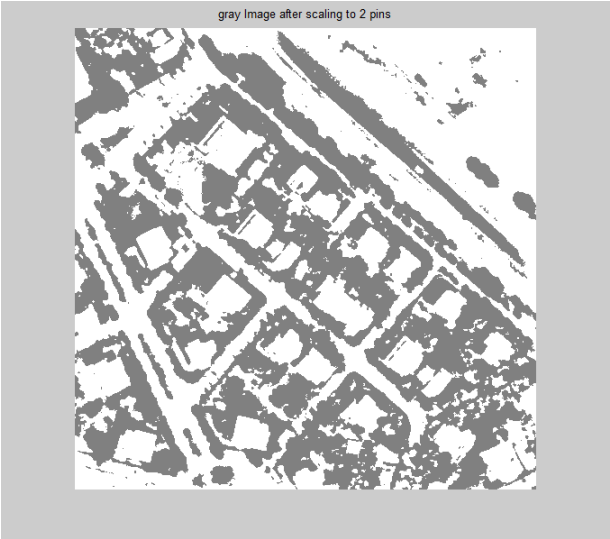

Figure 4-13 The image in Figure 4-12,after scaling to two pins

A forward curvelet transform is, then, applied and the curvelet coefficients are generated in multi-scale and multi-directions. These scale levels are divided into three parts, namely coarse level, detail level and fine level. Then curvelet transform is applied to extract the coefficients from these parts. Images are then reconstructed for each level with those coefficients as shown in Figure 4-14.

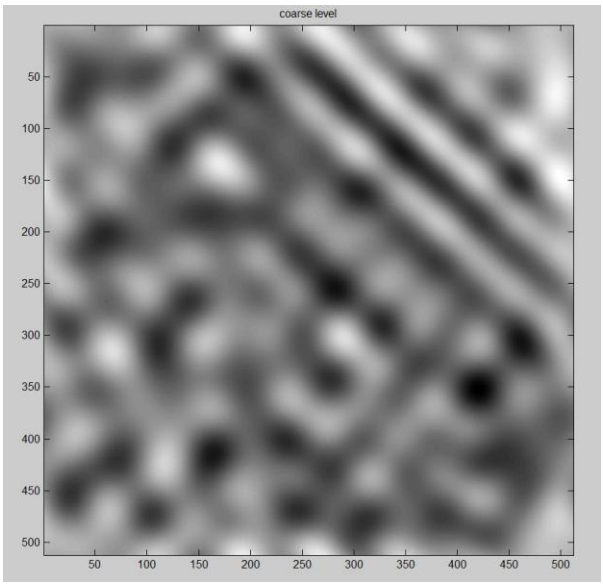

Coarse Level

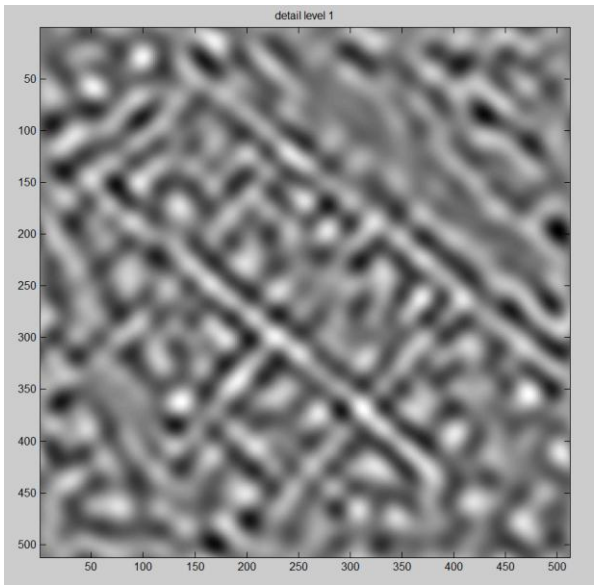

Detail Level 1

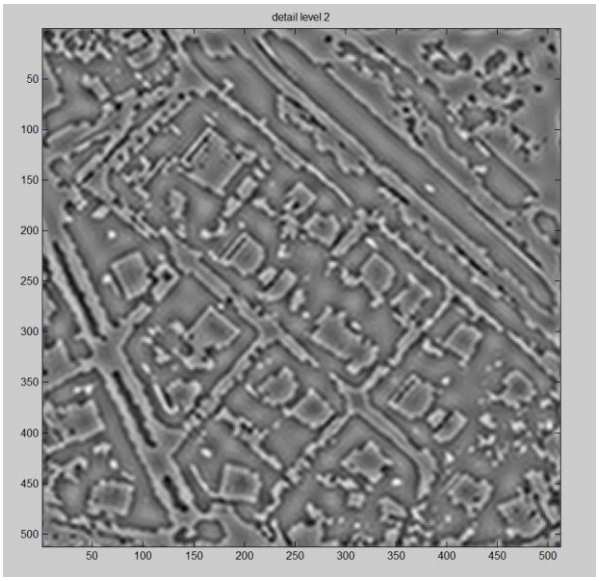

Detail Level 2

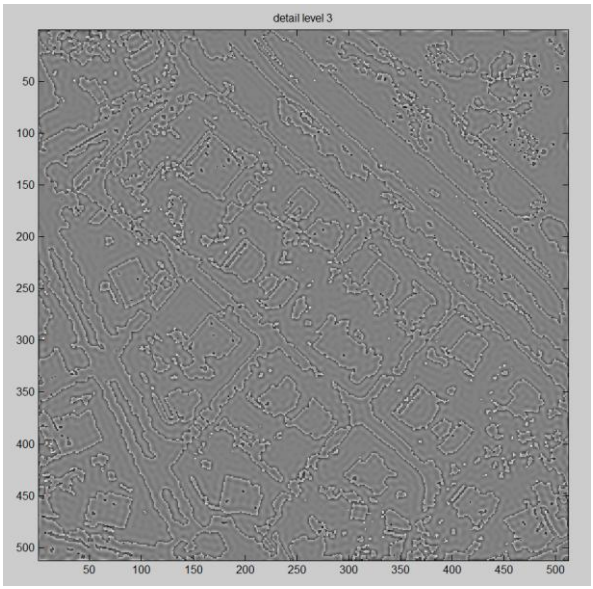

Detail Level 3

Figure 4-14 The reconstructed coarse and fine details levels

Analyzing the curvelet transform coefficients, it can be seen that they contain different information in each scale level. Consequently, by arranging the coefficients of each level and by taking the most significant part of them, this will enhance the edge information that represents

the image part of interest. Then, the coefficients are reconstructed to get a new image called the edge map, as shown in Figure 4-15, where the edge parts are enhanced. The edge image is then thresholded to get enhanced one as shown in Figure 4-16.

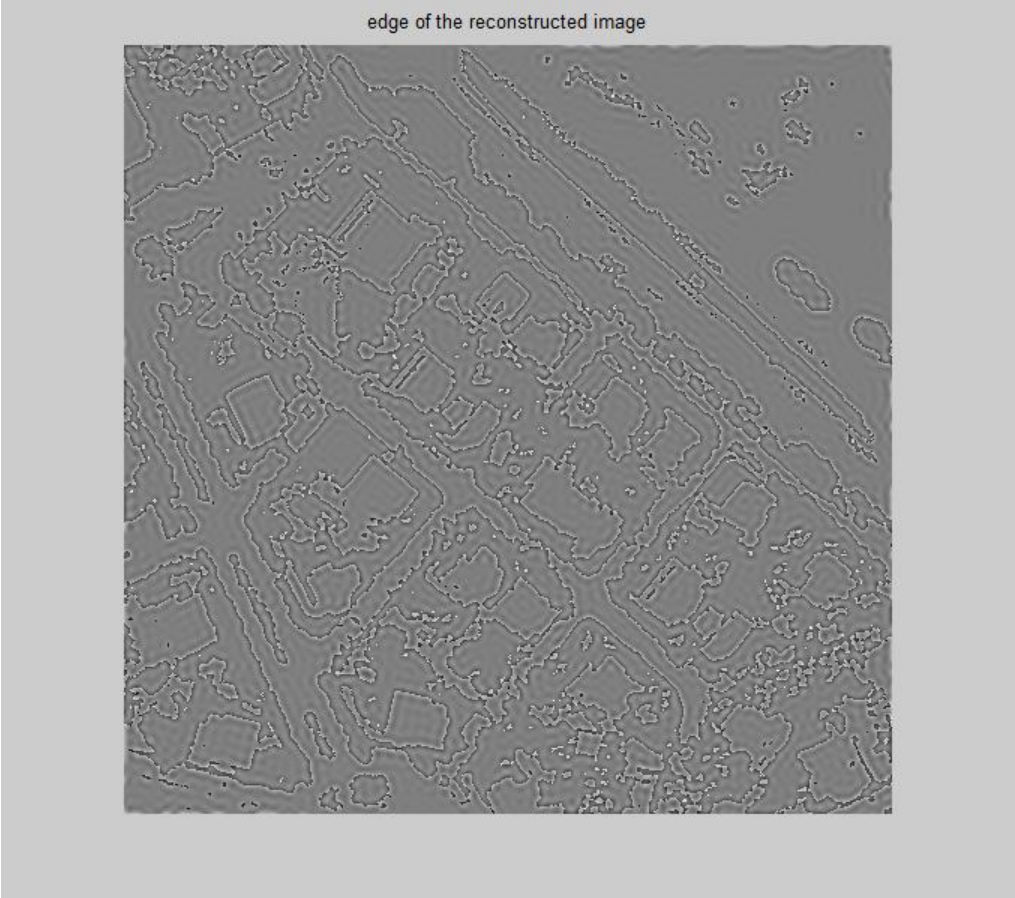

Figure 4-15 The reconstructed edge map

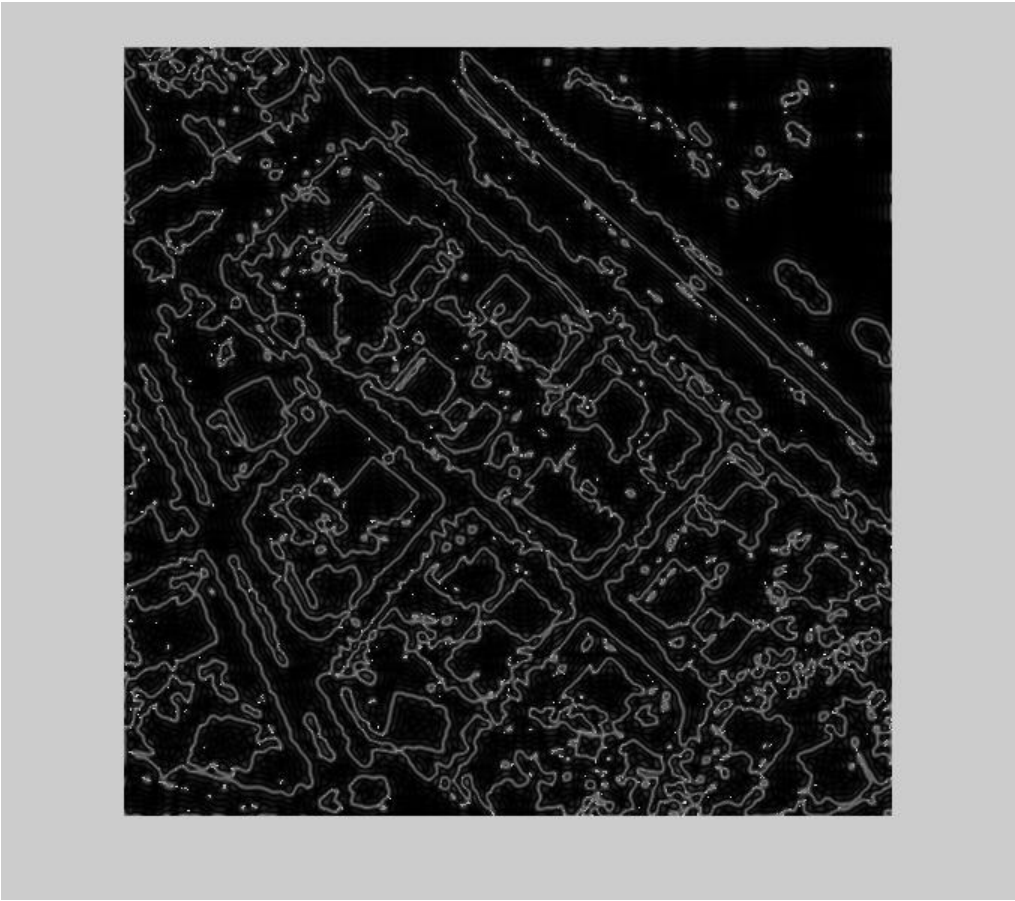

Figure 4-16 The reconstructed edge map after thresholding

The reconstructed edge image was thresholded based on the fact that any edges will have abrupt changes in the pixel from negative to positive values and the absolute summation will determine the strength or the weakness of that particular edge. Figure 4-17, (upper row) illustrate two points on both sides of a strong edge and the index values are +3882 and -3820 respectively gives an absolute summation of 7702, while the same figure (lower row) illustrate two points on the sides of a weak edge having the values of -220 and +270.2 respectively gives an absolute summation of 490.2 which is far lower than the previous value.

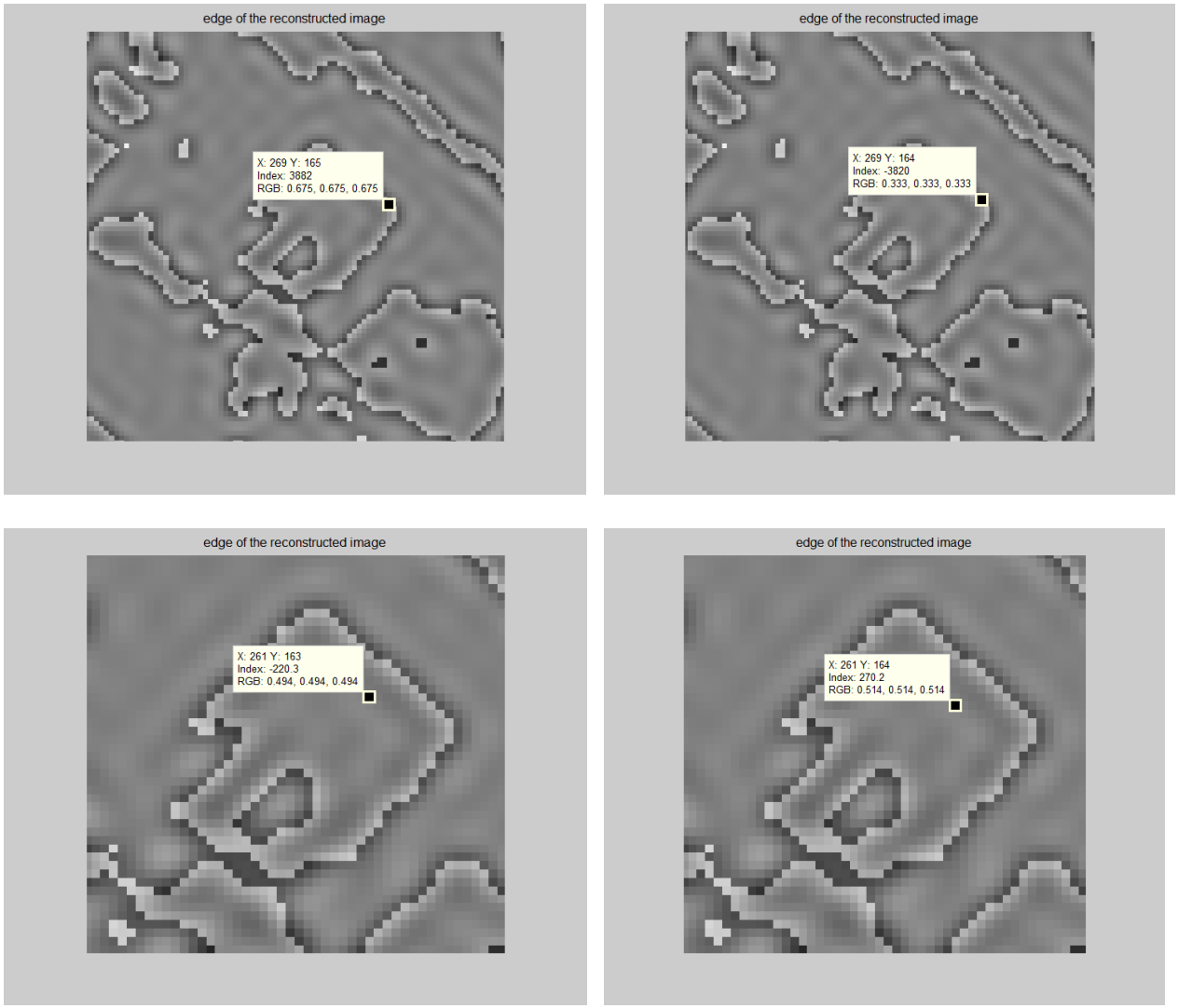

Figure 4-17An example of the thresholding criteria(Elsharkawy et al. 2011)

The next step is applying morphological filters to get rid of undesired artifacts and the result is in Figure 4-18.

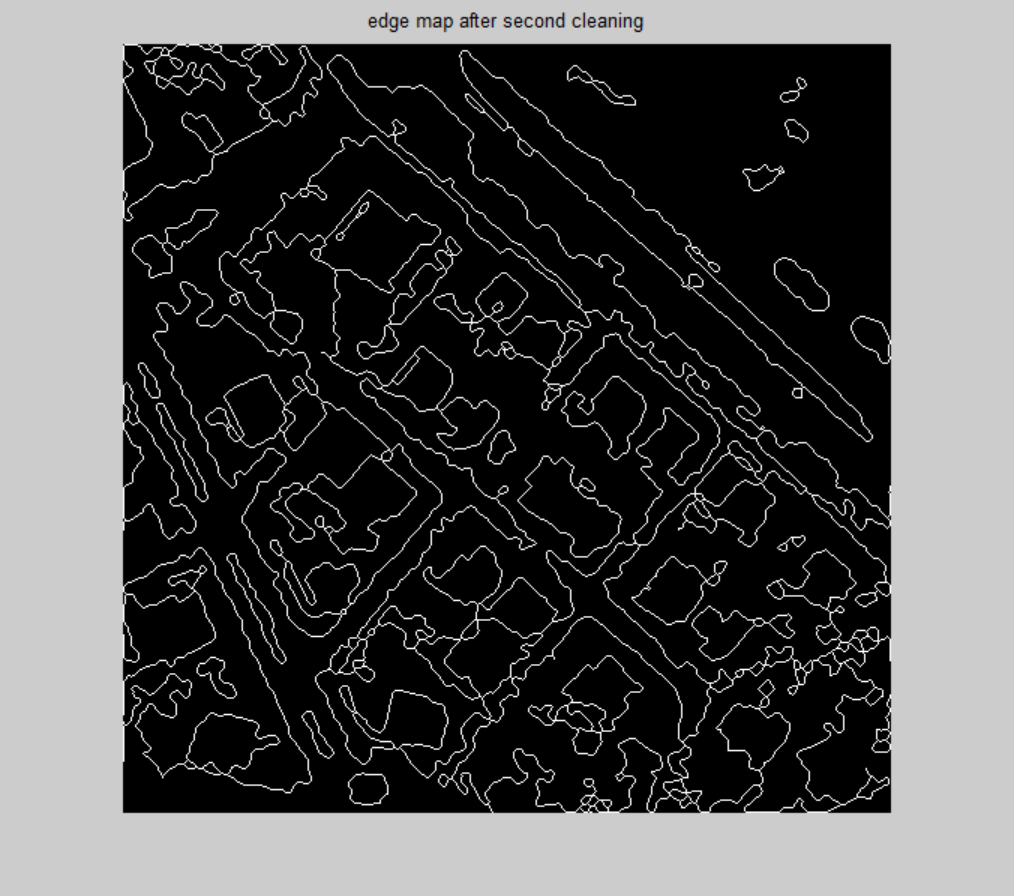

Figure 4-18 The reconstructed edge map after applying morphological filters

A filling process to all closed area is applied to generate colored parcels to work as candidates for the next building extraction process. The result is in the following figure.

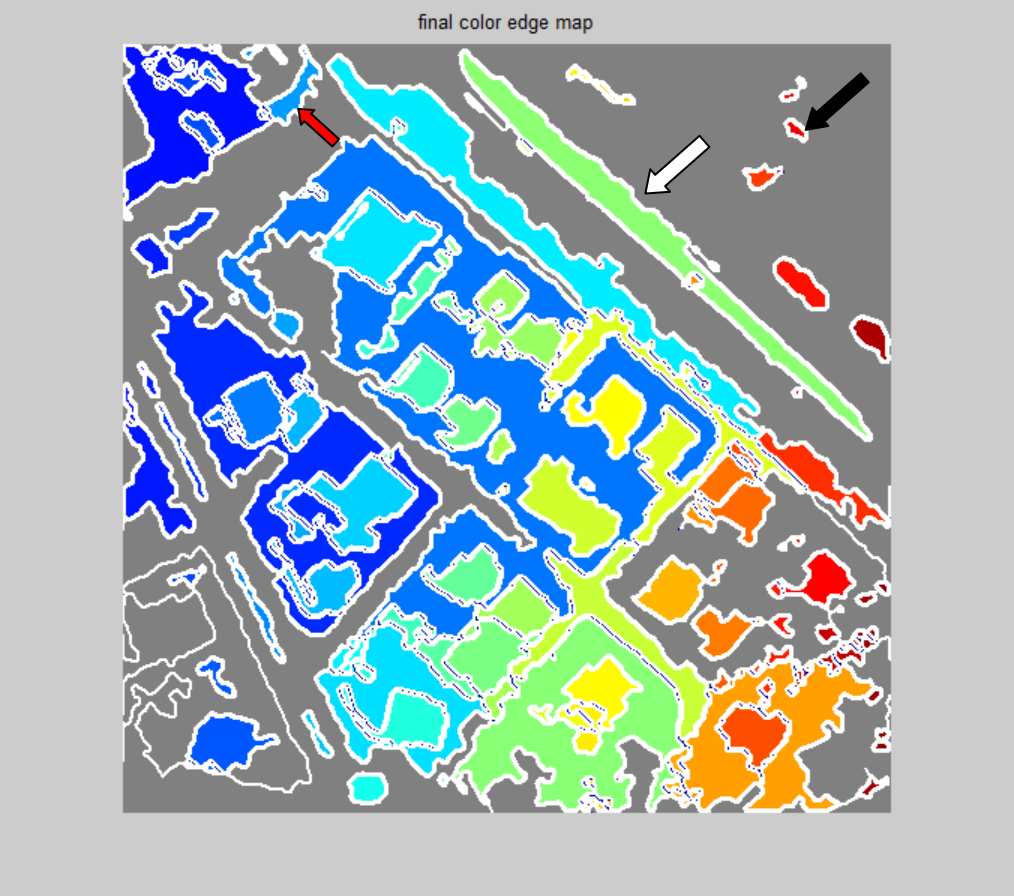

Figure 4-19 the colored edge map after filling

Statistics such as; area, major and minor axis of the closed boundaries are then calculated to help in choosing the parcels that represents buildings out of the candidate parcels. Three thresholds for the area, the ratio between the major and minor axes and finally the compactness, area/perimeter^2, of the closed parcels are computed and used to get the best extraction of the building parcels. For instance, the ratio between major and minor axes was very helpful in rejecting elongated parcels such as the one indicated by the white arrow in Figure 4-19. Also the area threshold was used to eliminate very large parcels or very small parcels such as the small parcel indicated by the black arrow in the same figure, while the last ratio was used to eliminate

un-compacted parcels such as the one indicated by the red arrow in the same figure. The final result is in Figure 4-20.

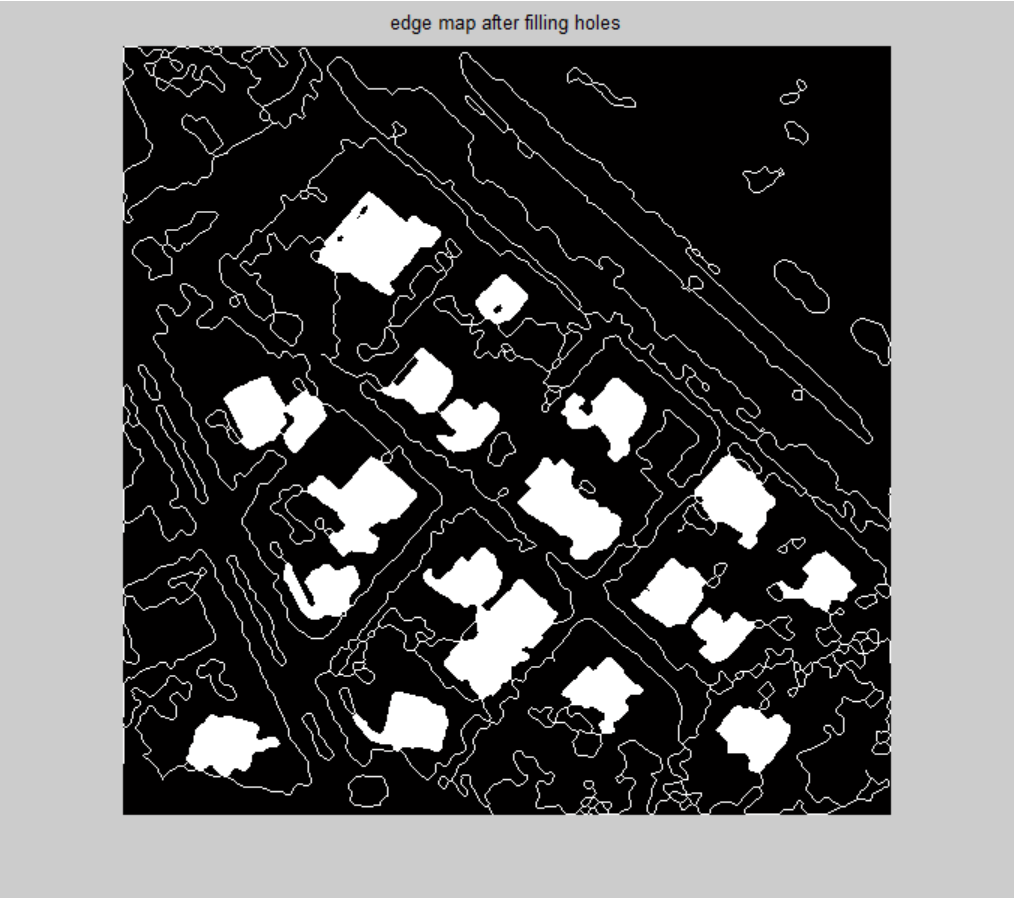

Figure 4-20 Final detection of building parcels

The edge detection process was repeated using Wavelet transform and Canny Edge detector for comparison purpose between these traditional techniques and the curvelet transform approach and the results in Figure 4-21. On one hand, it was clear that Canny edge detector, which is known as the optimum detector in the spatial domain gives almost identical solution to the curvelet transform which can be considered then as the optimal edge detector but in the frequency domain, which is very good results putting in mind the advantages of working in the

frequency domain. On the other hand the wavelet transform solution was very bad compared to the curvelet and Canny Due to the limitation in directionality and scaling of the wavelet transform.

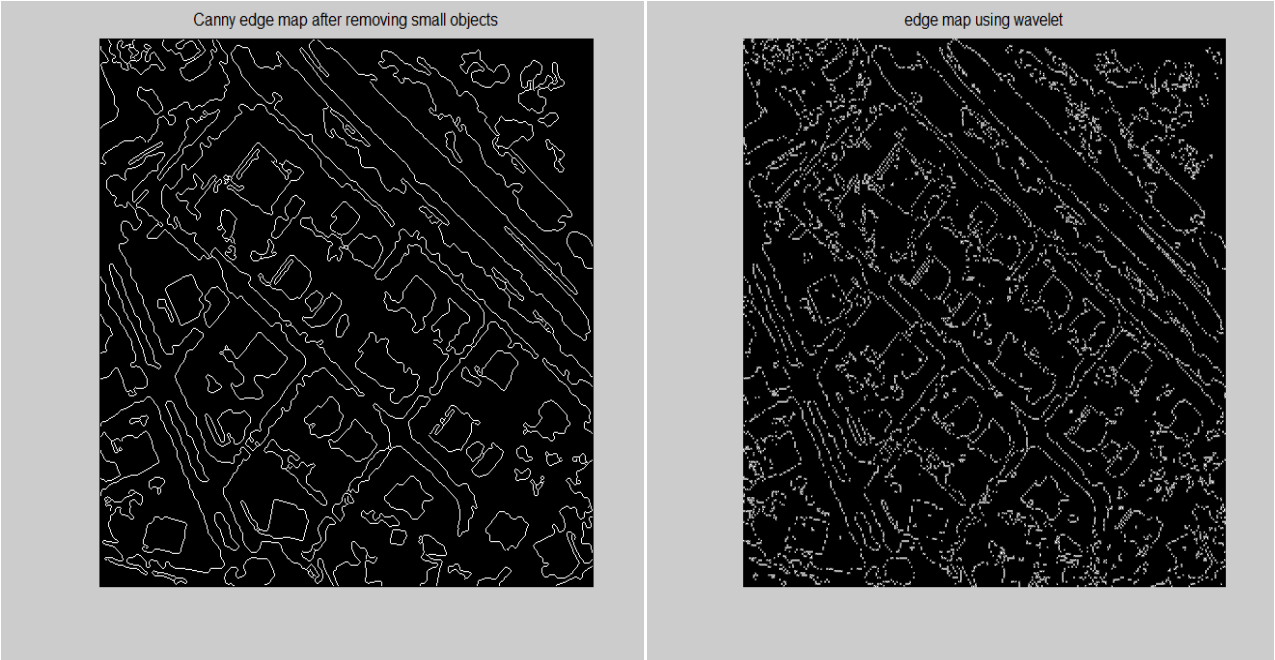

Figure 4-21 edge detection results using canny operator (left) and wavelet transform (right)

4.3.4 Accuracy assessment of the building extraction results

Overlaying the final detection image over the original image will emphasize the efficiency of this method where 19 building out of 24 buildings were perfectly delineated and accurately extracted and marked within the white pixels. The overall accuracy is approximately 80%. The processing time was less than 17 seconds for a 512X512 pixels starting from reading the images until the final results. The process is considered automatic as there is no interference from the operator side during the processing, putting in mind that the thresholds will be determined previously based on the characteristics of the buildings in the study area such as the area and the shape. Figure 18 shows the final result overlaid on the original image.

4.4 Integration of both object/pixel based approaches

The processes of per-pixel supervised classification methods were always the primary tool to extract land cover classes from digital remotely sensed data (Bhaskaran et al. 2010). The ultimate goal of any image classification procedure is to automatically categorize all pixels in an image into land cover classes (Lillesand and kiefer 2001). For the purpose of urban planning, supervised classification has been used extensively. Unfortunately, this procedure always results in mixed pixel's problem (Bhaskaran et al. 2010). This problem leads many researchers to incorporate segmentation, texture, context, colour, and many other parameters to glide the mixed or wrongly classified pixels into their proper classes. Segmentation can be done either by detecting similarities or by detecting singularities (edge detection) (Gonzalez and Woods 2002). Contrasting spectral methods, object-oriented methods are based on segmenting the image into homogeneous parcels of pixels then these parcels are classified using spectral, spatial, textural, relational and contextual methods (Bhaskaran et al. 2010).

The primary objective of this section was to classify urban features from a WorldView-2 imagery by using both per-pixel classification, three new band ratios as describes in section 4.2.4, and object-oriented classification method, edge detection using curvelet transforms as described in section 4.3. The first step implements the three new band ratios to classify the image and check accuracy of all classes. The second step improves the accuracy of the lowest two classes' accuracy. The final step involves the integration between the previous two steps to enhance the pixel-based classification results. The main idea behind this step is to incorporate the object-based results as a classification layer to be added to the multi-layer classification process.

In this integration step, we have confidence in the water, vegetation, asphalt and shadow classes, while building and bare soil classes can be modified according to the edge detection process. If

we denote the pixel-based classification results by p(m,n) and object-based classification results as E(m,n) and the final classification results as f(m,n) so we can apply the following rule to integrate the object and pixel based results.

If p(m,n) water then …….f(m,n) = water
If p(m,n) vegetation …….f(m,n) = vegetation
If p(m,n) shadow…….f(m,n) = shadow
If p(m,n) asphalt and f(m,n) not buildings then f(m,n)= asphalt
If p(m,n) bare soil and f(m,n) not buildings then f(m,n)= baresoil
If p(m,n) building ……..f(m,n)= buildings
If E(m,n)>0 and f(m,n) not vegetation or shadow or asphalt then f(m,n) is building

Generally, any imagery will be used in a radiometric/spectral analysis must be converted to spectral radiance at a minimum or top of atmosphere reflectance in order to account for the variation in the relative positions between the sun, the earth and the satellite to obtain absolute values for the NDVI ratios can be applied in any other scene (Updike and Comp 2010). Converting the Digital Numbers (DN) to top of atmosphere (ToA) reflectance is a two-step process. First DN's are converted to top of atmosphere radiance values. Then these radiance values are then converted to reflectance values(Observation 2010; Elsharkawy et al. 2012).

4.4.1 Results and analysis of the integration between object/pixel based approaches

Figure 4-9, illustrates the output from the multi-layer classification process. While Figure 4-22 and Figure 4-23, represent the edge detection map for the study area and the candidate parcels as buildings, as described in section 4.5 respectively.

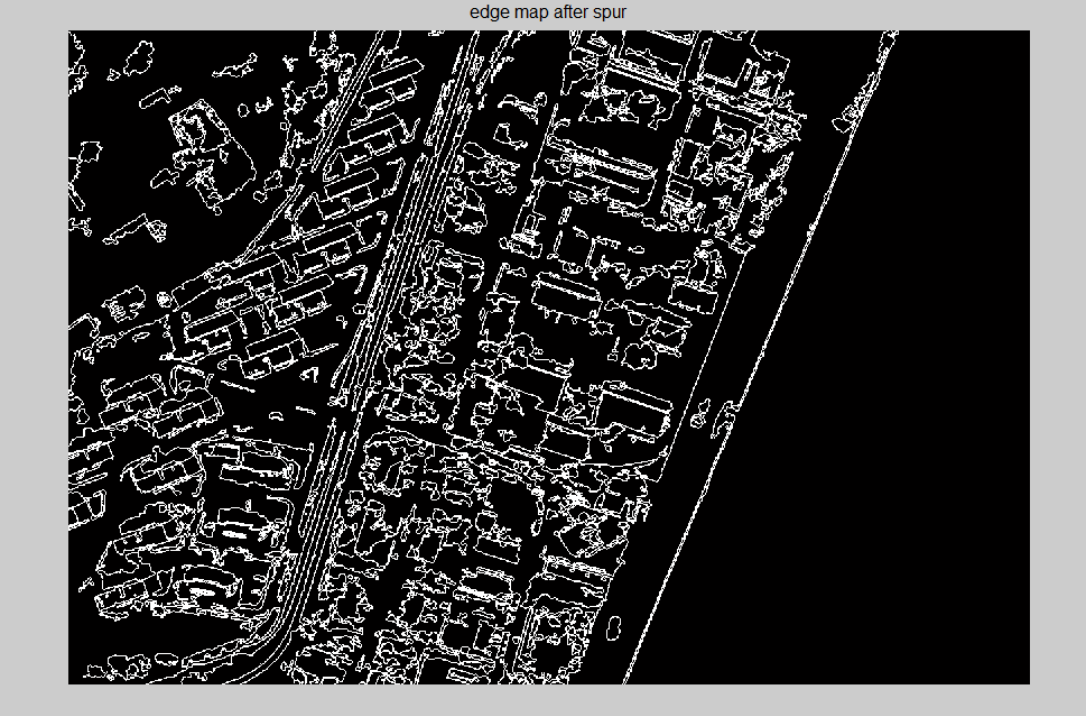

Figure 4-22 Edge detection result

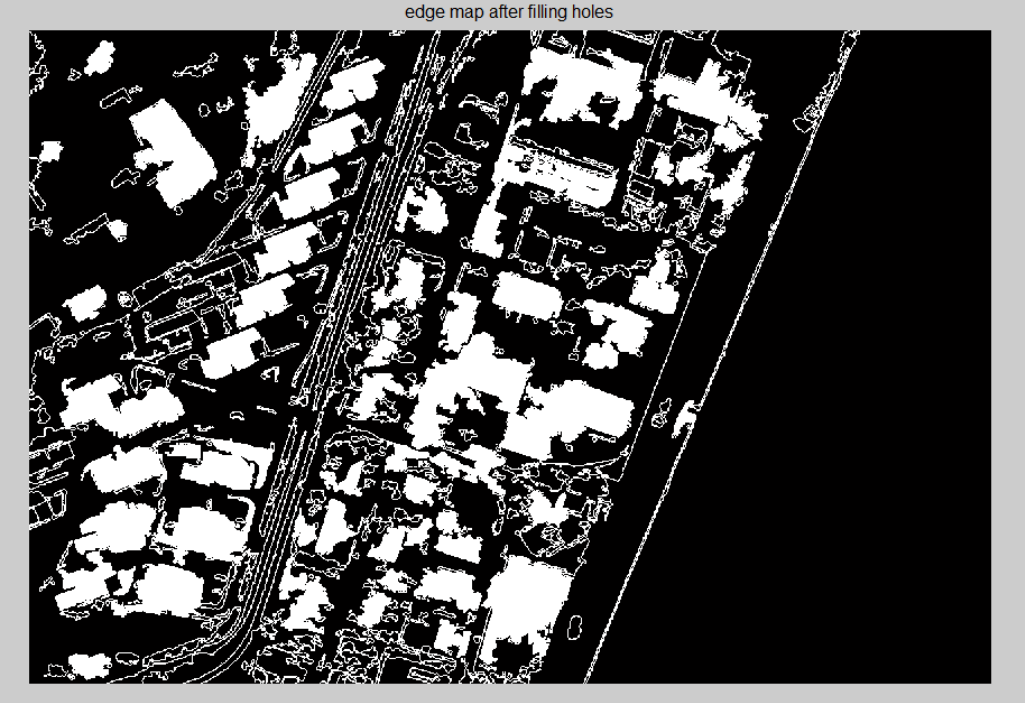

Figure 4-23 Candidate parcels as buildings

Figure 4-9, shows that the algorithm mixed between shadow and vegetation areas with buildings. The integration part, Figure 4-24, will account for this confusion as vegetation and shadow areas are well defined in the multi-layer classification part. A quantitative analysis for the building class (extracted) were done by comparing the number of buildings in the original image by the complete detected number of buildings being detected in the classified images either from pixel-based output or from the final integrated output. Table 4-7, summarizes the comparison results.

Table 4-7 Pixel-based results Vs. proposed method

	No. of Red Roofs	*No. of Tall buildings*	*No. of Short buildings*	*Total No.*
Ground truth	14	17	17	48
Pixel-based result	12	9	1	22
Accuracy %	85.7	52.9	5.8	45.8
Proposed method	14	16	11	41
Accuracy %	100	94.1	64.7	85.4

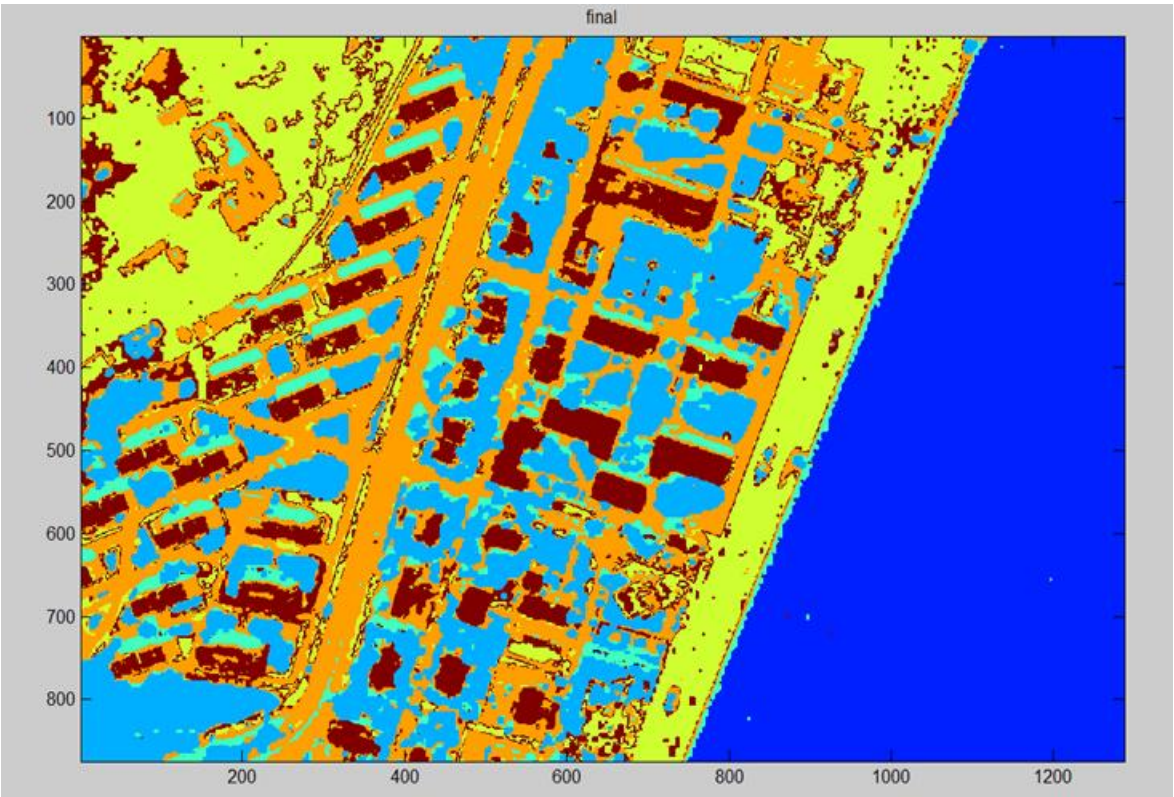

Figure 4-24 final classification results

Chapter Five: **Coastline Detection and Bathymetry**

5.1 Introduction

In this chapter, second generation curvelet transform in the edge detection of coastline is presented and applied on WorldView-2 imagery**,** together with a comparison with the classical edge detection methods such as Canny operator and the traditional wavelet transforms. This implementation is aiming to compare this new approach to the traditional edge detection techniques. Then, the new bands of WorldView-2 will be utilised in deriving the relative bathymetry of part of the water way of the Suez Canal and Temsah Lake, Egypt.

5.2 Coastline detection

Urban studies, coastal erosion, and agricultural surveys are a few examples where edge detection can be utilized. In the past few years, the development of edge detection techniques for the analysis of multi-temporal remote sensing imagery has been intensively growing. One of the most important characteristic in an image is the features edges, which can be described as a discontinuity in the local domain of the image. These discontinuities may result as gray, colors and texture variations (Zhenghai and Jianxiong 2009). Edge detection has broad applications in the domain of image processing, computer vision and so on. In the next three sections the area of study, methodology and the discussion of the results will be explained.

5.2.1 Study area

The study area is an urban area comprises scattered buildings, two shorelines and water body. The data was provided by Digital Globe, the images were captured on April 7th, 2011 in morning time. Figure 5-1, illustrates a gray scale image of the study area.

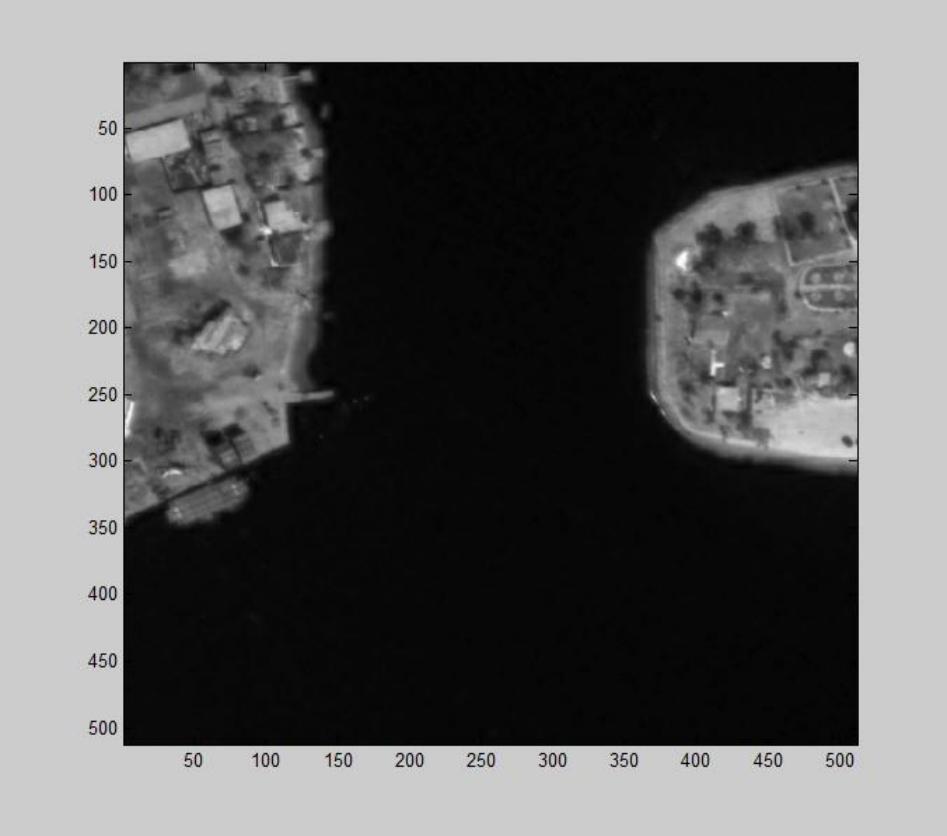

Figure 5-1 Gray scale image of the area of study

5.2.2 Methodology

As described in section 4.3.2, image sharpening takes place at the beginning of this algorithm, then water body will be extracted using an NDVI like ratio, using the NIR-2 and C bands. Then, based on the curvelet transform theory an implementation for detecting edges will be introduced (Elhabiby et al. 2012). As described in chapter three, the coefficients are reconstructed to get a new image where the edge parts are enhanced. Morphological filters will be applied to eliminate the undesired noised pixels. Figure 5-2, represent a schematic diagram of the aforementioned algorithm.

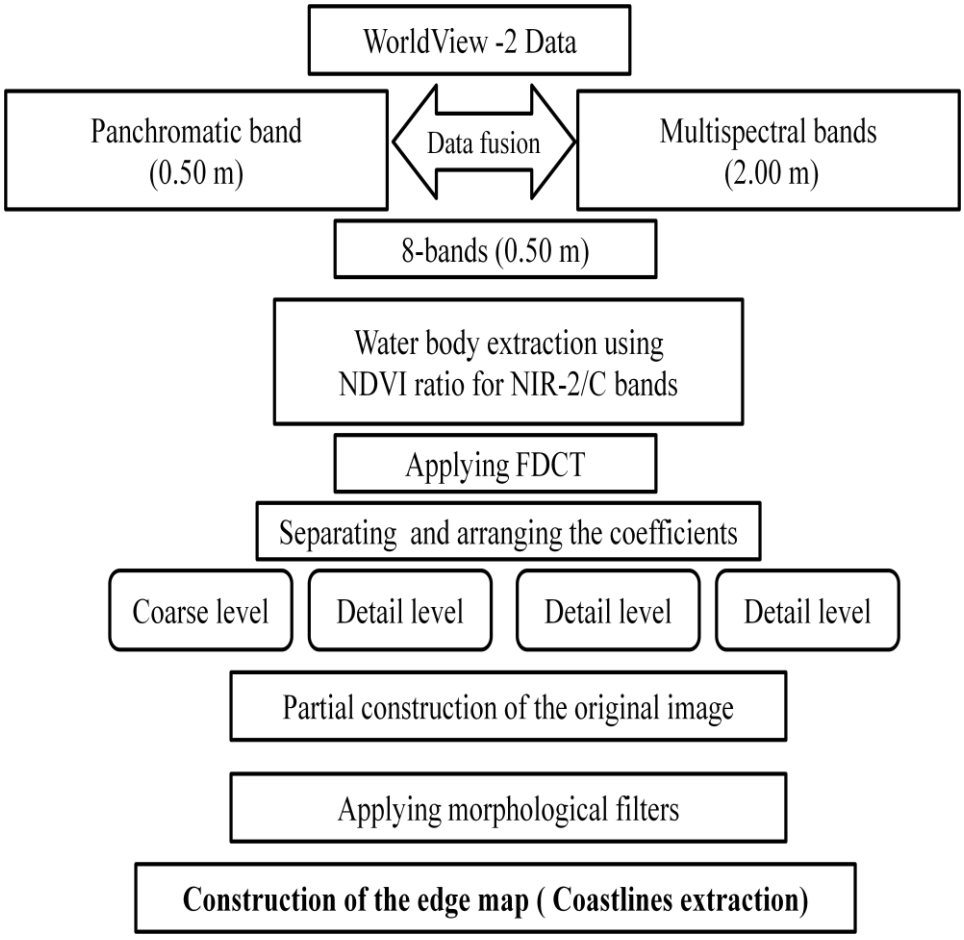

Figure 5-2 The proposed algorithm

5.3 Results and Discussion

NDVI rationing between bands 8 and 1 is then applied to extract the water body. Then, thresholding is applied to the NDVI output to get binary image as in Figure 5-3.

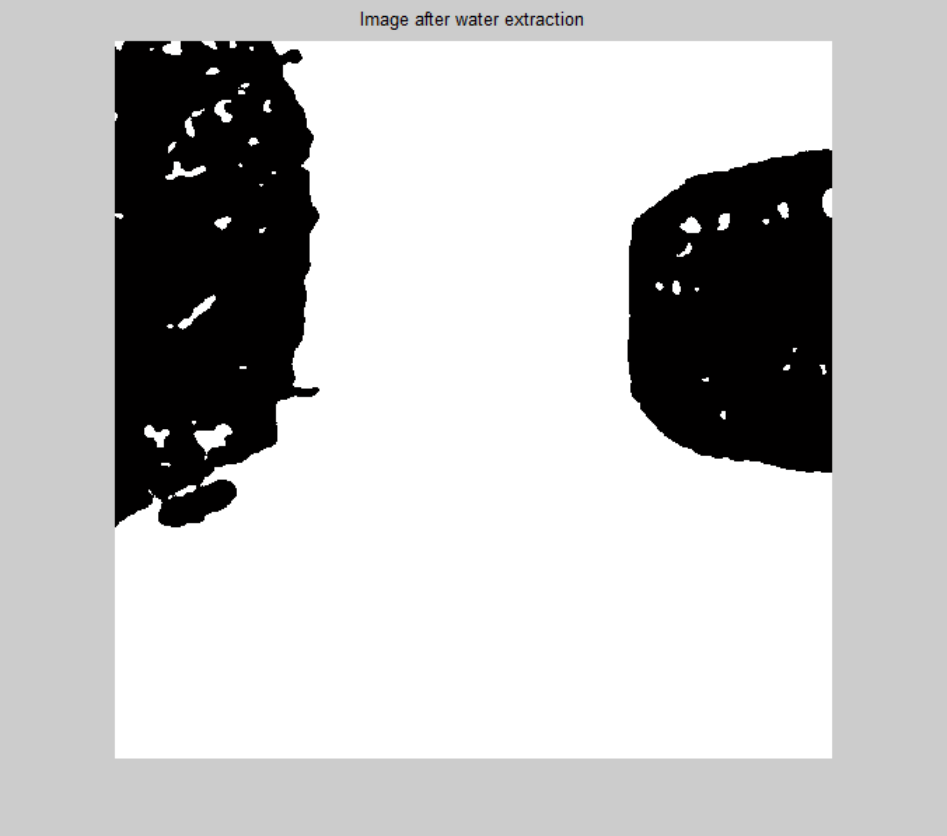

Figure 5-3 The image after water extraction

Then, the 2D FFT of the output image is calculated to obtain the curvelet coefficients. These coefficients are generated in multi-scale levels will be grouped into three parts, which are coarse level, detail level and fine level. Images are then reconstructed for each level with those coefficients as in Figure 5-4. First scale generates the coarse level image, while second and third scales were merged to generate the detail level 1 image, fourth and fifth scales were merged to generate the detail level 2 image and finally sixth scale was responsible for the generating of the detail level 3 image.

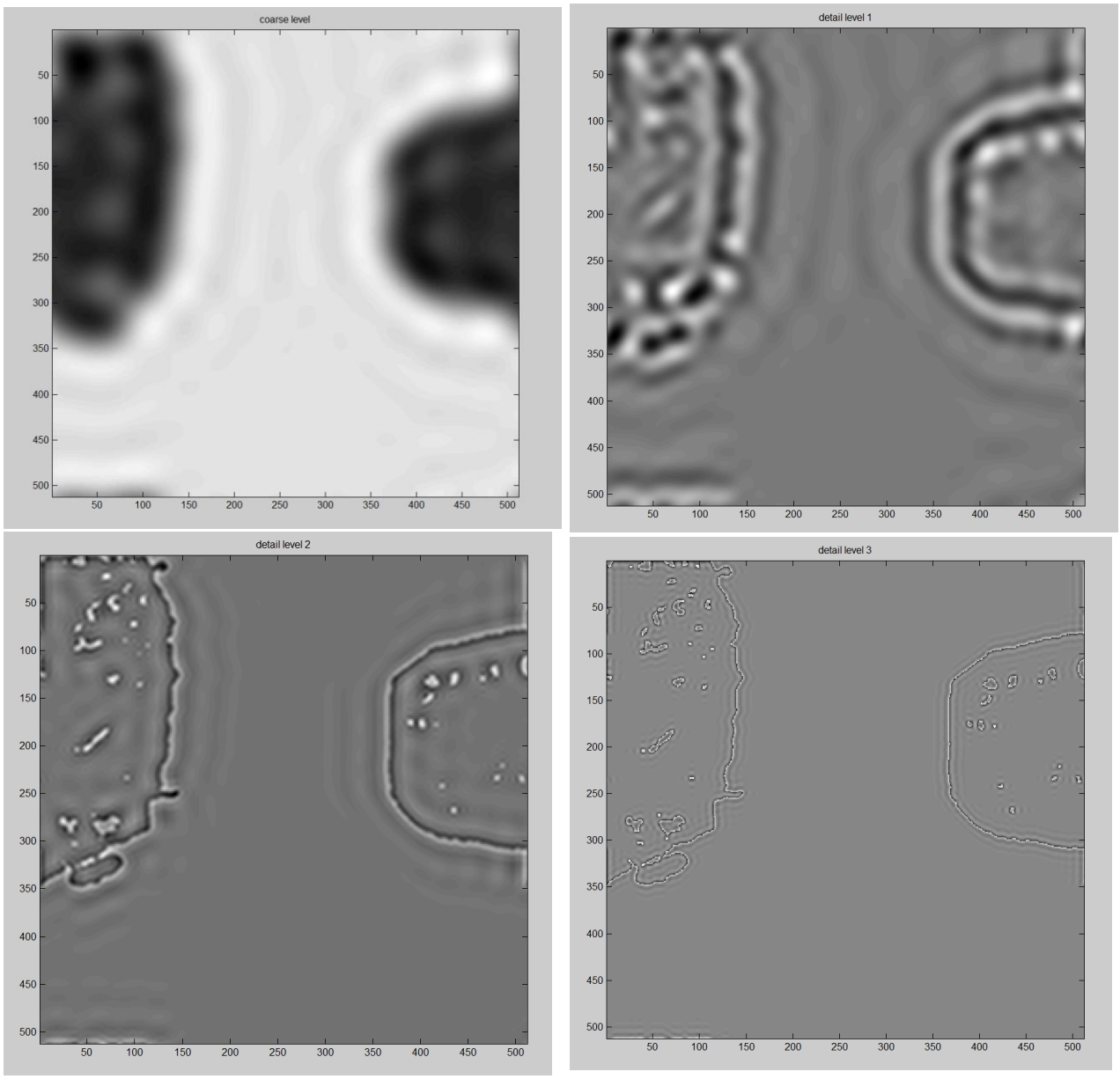

Figure 5-4 The reconstructed coarse and fine details levels

Analyzing the coefficient of curvelet, it can be found that the coefficient in each scale level contains different information. Consequently, by arranging the coefficients of each level and take the most significant part of them, this will enhance the edge information that represents the important part of the image to us. In other words, larger coefficients will be emphasized and

small coefficients in value will be suppressed. Then, the coefficients are reconstructed to get a new image called the edge map, where the edge parts are enhanced. Table 5-1, summarizes the total number of coefficient in each scale and the actual used percentage.

Table 5-1 the percentage used in reconstructing the edge map image

Scale	No. of total coefficients	Percentage used	No. of used coefficients
1	441	0%	0
2	5984	0%	0
3	22880	0%	0
4	90144	100%	90144
5	357408	1%	3574
6	1417248	1%	14172
Total	1894105	5.7 %	107890

The edge map is then thresholded to get enhanced edge map as in Figure 5-5. The reconstructed edge image was thresholded based on the fact that the strong edges have abrupt changes in the pixel from negative to positive values and the absolute summation falls within a certain threshold. The next step is applying morphological filters to clear the undesired artefacts and the result is in Figure 5-6.

Figure 5-5 The reconstructed edge map after thresholding

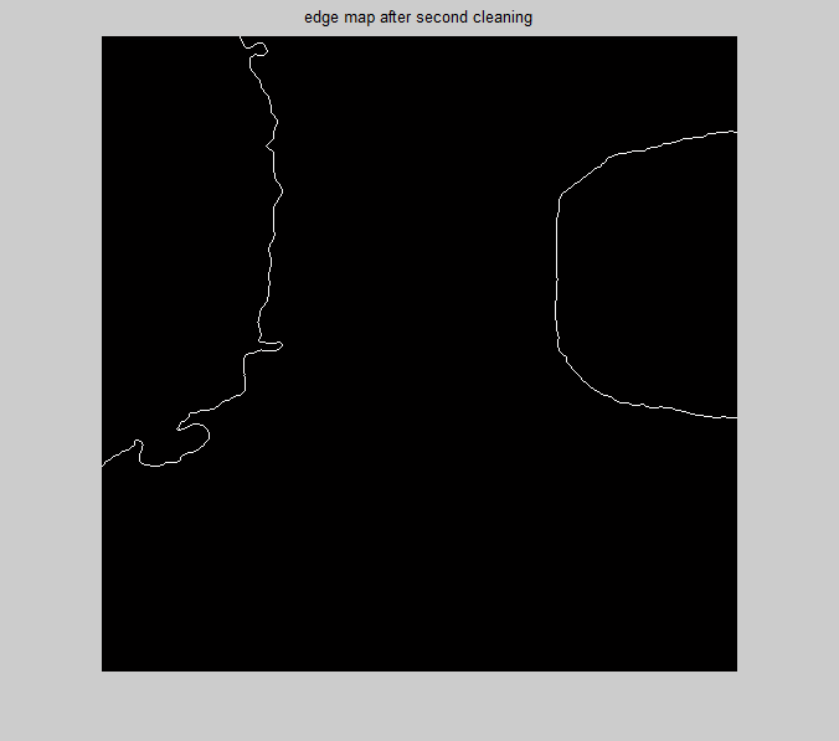

Figure 5-6 The reconstructed edge map after applying morphological filters

The final result was overlaid over the original image to show the exact matching of the delineation of the coastline, Figure 5-7.

To illustrate the quality of this algorithm compared with Canny and wavelet transforms, the procedure was repeated using these two methods, canny was used with sigma equal to 1 and the thresholds T1= 0.006 and T2= 0.02.

Figure 5-7 Final result overlaid over the original image

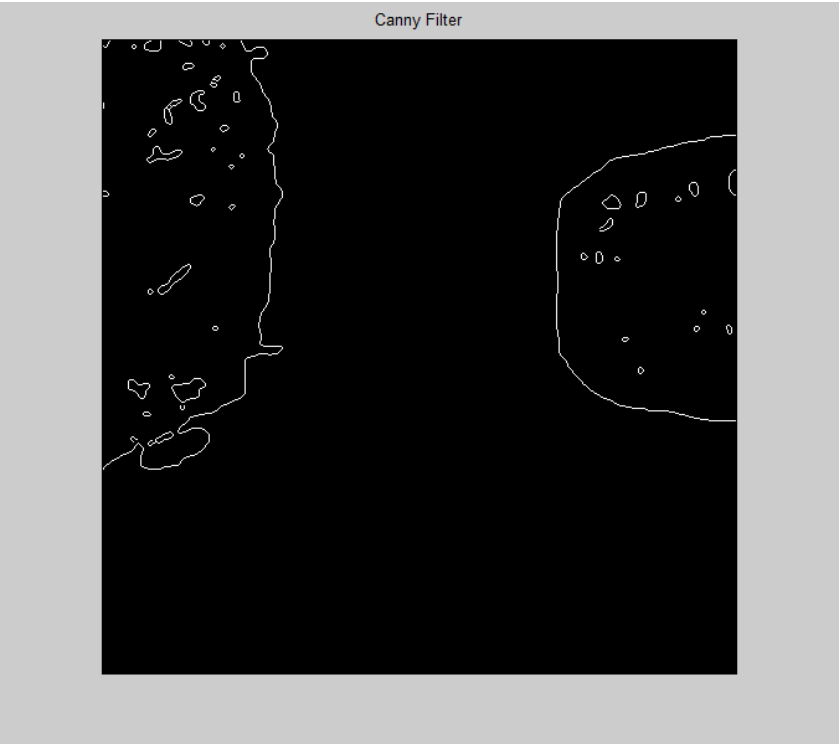

Figure 5-8 Results with Canny Operator (the input is the classified image)

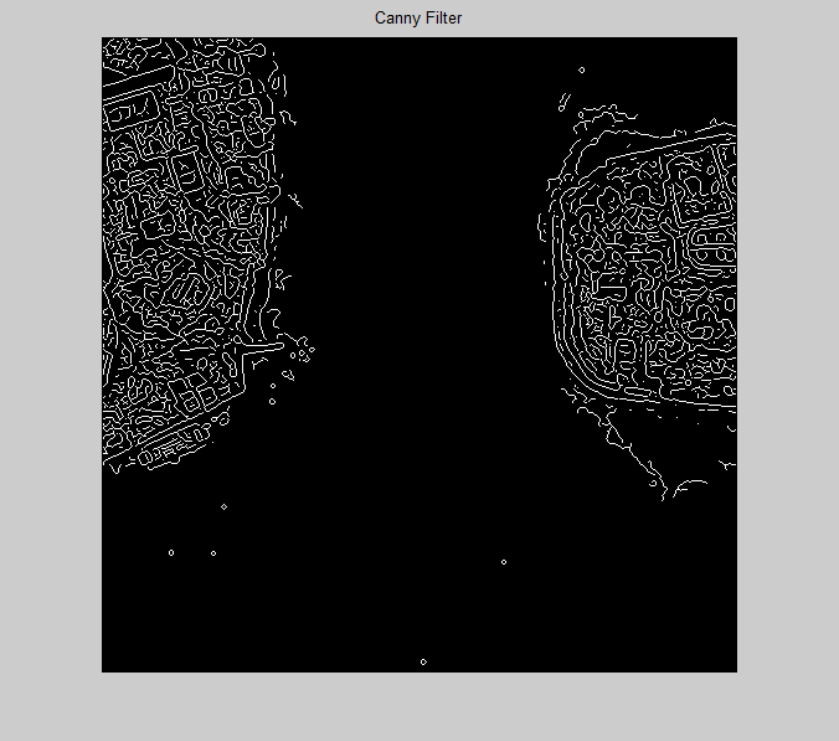

Figure 5-9 Results with Canny Operator (the input is the original image)

The result in Figure 5-8, shows almost identical similarity with the curvelet transforms edge detection result, when the input to Canny was the classification image. While if the input was the original image without any classification the result was in Figure 5-9.

The case was different with the wavelet as in the Figure 5-10, which illustrate the edge detection result when using the classified image as an input to the wavelet transform. And it was much worse when using the original image as an input to the transforms. The total number of generated coefficients was 262144 and it was used totally, which is more than twice the number of coefficients used in case of curvelet.

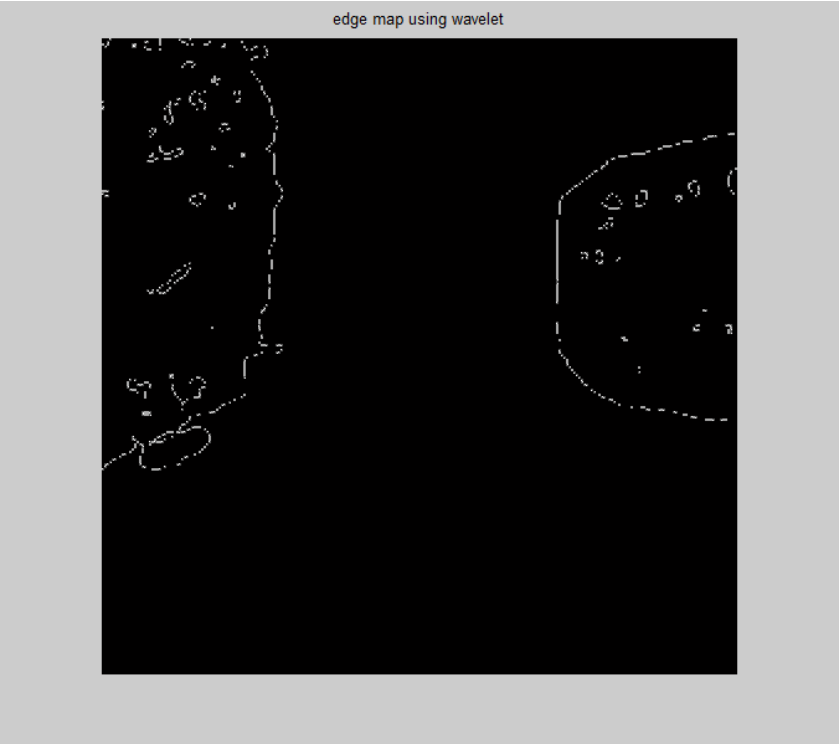

Figure 5-10 Results with Wavelet transform (the input is the classified image)

A small area in the classification map, Figure 5-6, was picked and enlarged to emphasize the potentials of using the curvelet transform as an edge detector against Canny and wavelet transform. Figure 19 is highlighting one pixel in every edge map and in the original classification map as well.

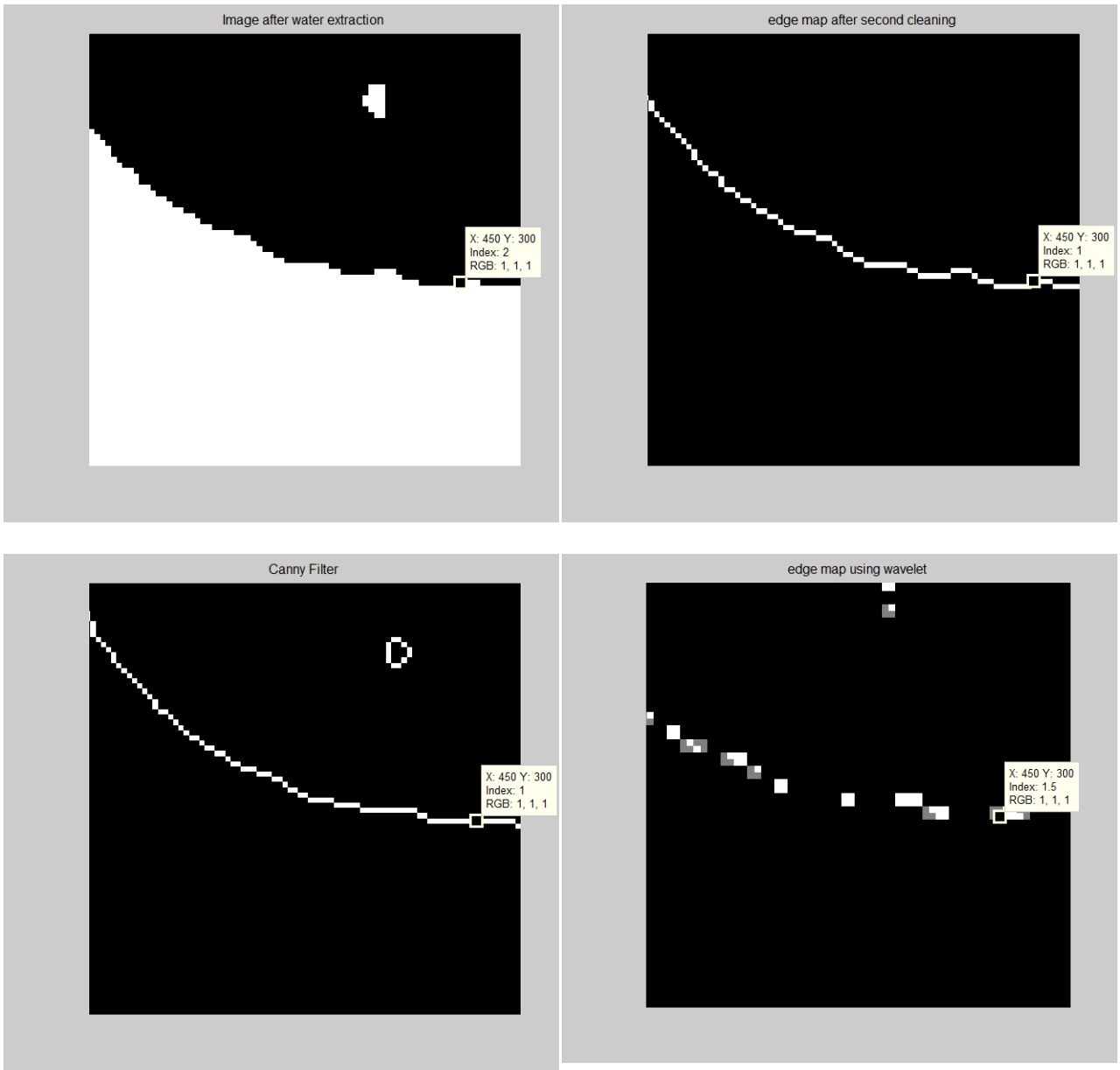

Figure 5-11 Highlighting a certain pixel in curvelet , Canny and wavelet transform

It was very clear that curvelet gave the most accurate delineation of the edges better than the Canny and the wavelet transform.

5.4 Bathymetry

Typically, bathymetric charts are generated from ship-borne sounding surveys with single- or multi-beam echo sounders, in which they can operate to depths more than 500 m. State-of-the-art acoustic multi-beam, swath-mapping systems can achieve 6 m spatial resolution and about 8 cm depth accuracy in 200 m water depth (Su et al. 2008). However, in case of shallow water, ship-borne surveys may not be the proper solution for the following reasons:

- The survey will be time consuming and expensive, as the survey swaths are narrow.
- It may not be feasible to survey waters shallower than 2–3 m deep because of sound saturation or/and inaccessibility of survey vessels.

Recently, airborne bathymetric LiDAR (Light Detection And Ranging), introduced an optimum solution for the mapping of shallow coastal waters. The only limitations occur with this relatively new technology are; the high cost of operation and that the amount of maximum penetration of LiDAR systems is greatly dependent upon water transparency. Average penetration depth for most of currently operated systems are in the range of 30 meters, LADS (Laser Airborne Depth Sounder) developed by Tenix LADS Corporation is an exception where penetration depth reaches 70 meters. Also, most systems can reach up to 4 meters spatial resolution with 20 cm accuracy (Su et al. 2008). In 2012, Optech developed CZMIL, coastal zone mapping and imaging LiDAR. CZMIL is an innovative airborne coastal zone mapping system that integrates bathymetric LiDAR, with a hyper-spectral imaging system and digital

metric camera to produces simultaneous high-resolution 3D data and imagery of the beach and shallow water seafloor (www.optech.ca/Optech_News_Release_CZMIL-120507.html).

Optical remote sensing was also introduced as an alternative solution for bathymetric applications. David R. Lyzenga, first introduced a model for shallow water depth estimation using a single band from aerial photography (Lyzenga 1978). This model was then expanded to multi-spectral satellite imagery using a non-linear bathymetric inversion model (Stumpf et al. 2003).

According to Beer's law, the basic physical principles underlying the retrieval of bathymetric information from optical remote sensing images are:

- Light attenuation in the water column increases exponentially as depth increases.
- Additionally, attenuation varies by wavelength, resulting in less attenuation and greater depth penetration in the blue region of the visible spectrum than the green or red regions (Lyzenga 1978; Lyzenga 1981).

These two properties are the basis for optically-derived bathymetry from multispectral, passive sensors. In the next section a brief summary of these two properties and how they can be applied to finally derive water depth of shallow waters will be introduced.

5.4.1 Bathymetric Models for Optical Multi-spectral Imagery

According to (Jensen 2007), the total upwelling radiance (L_t) recorded by the remote sensor consists of four components, Figure 5-12, as shown in equation 5-1.

$$L_t = L_b + L_v + L_s + L_p \qquad \textbf{5-1}$$

Where, *(L_p)*, atmospheric path radiance, is a function of atmospheric scattering, including both Rayleigh (molecular) scattering and Mie (aerosol) scattering, ***(L_v)*, subsurface volumetric radiance,** results from volume scattering from the water and its organic/inorganic constituents like sediment and chlorophyll. ***(L_s)*, Specular radiance,** is the reflection from the water surface, including possible sun-glint effects. Finally, ***(L_b)*, the bottom radiance,** is the energy reflected from the seabed, which integrates the information about water depth and bottom characteristics.

In order to retrieve water depth information from the total radiance, bottom radiance (L_b), has to be extracted from the total radiance (L_t). Atmospheric correction and sun-glint removal are applied first to remove (L_p) and (L_s), then deep water correction is accomplished to remove (L_v) (Lyzenga 1978; Lyzenga 1981; Stumpf et al. 2003).

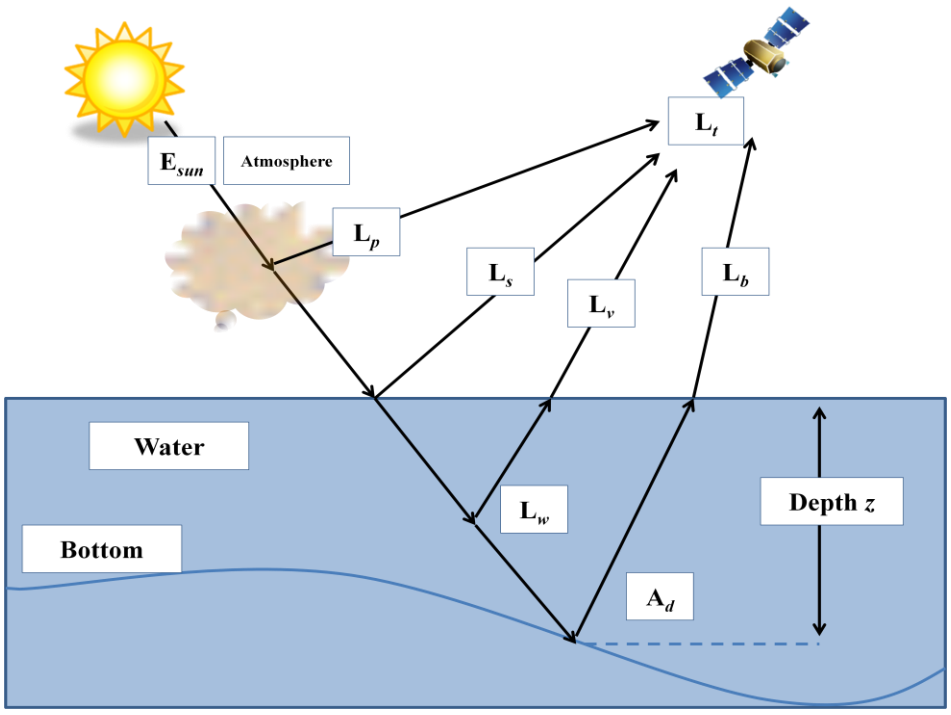

Figure 5-12 Four main components of the total radiance, after (Jensen 2007)

As long as, the bottom radiance (L_b) equals zero for deep water, then the measured total radiance over optically-deep water (L_∞) includes the joint effects of subsurface volumetric radiance (L_v), specular radiance (L_s), and atmospheric path radiance (L_p). After atmospheric and sun-glint corrections, the deep water radiance (L_∞) only contains subsurface volumetric radiance (L_v) (Su et al. 2008). Assuming that the values of (L_v) of shallow and deep waters will not change, then we can use optically deep water radiance (L_∞) recorded by the remote sensor to correct the subsurface volumetric radiance (L_v) in shallow water.

Based on Beer's Law, (Lyzenga 1978; Lyzenga 1981) introduced a simple radiative transfer model for shallow waters:

$$L = L_\infty [\, 1 - exp(-gz) \,] + A_d \, exp(-gz) \qquad \textbf{5-2}$$

Where, $L = L_t - L_p - L_s$, is the measured radiance after atmospheric and sun-glint corrections, L_∞ is deep water radiance (equivalent to volumetric radiance L_v), A_d is the upwelling spectral radiance directly reflected from the bottom before interacting with the overlying water column, g is a two-way attenuation coefficient, and z is depth. Rearranging this equation, putting z in the left hand side, results in the equation of the bathymetric inversion model for a single spectral band as follows:

$$z = g^{-1} [\, ln(A_d - L_\infty) - ln(L - L_\infty) \,] \qquad \textbf{5-3}$$

Later on, Lyzenga developed a new bathymetric inversion model using more than one band as follows:

$$z = a_o + \sum_{i=1}^{N} a_i \ln[L(\lambda_i) - L_\infty(\lambda_i)] \qquad \textbf{5-4}$$

Where, a_i are the constant coefficients, N is the number of spectral bands, $L(\lambda_i)$ is the remote sensing radiance after atmospheric and sun-glint corrections for spectral band λ_i , and $L_\infty(\lambda_i)$ is the deepwater radiance for spectral band λ_i .

The model explained in Eq. 5-4, referred to as the log-linear inversion (or deepwater correction) model, this model has been extensively used for estimating water depths from optical multi-spectral remote sensing imagery (Su et al. 2008).

In 2003, (Stumpf et al. 2003) proposed a non-linear bathymetric inversion model based on a log-transformed band ratio:

$$z = m_1 \frac{\ln(nL(\lambda_1))}{\ln(nL(\lambda_2))} - m_o \qquad \textbf{5-5}$$

Where, m_0, m_1, and n are constant coefficients for the model, and L (λ_1) and L (λ_2) are the atmospheric and sun-glint corrected remote sensing radiances for bands λ_1 (short wave length), and λ_2 (long wave length) (Stumpf et al. 2003).

When two bands are used, with different water absorptions, the log values change with depth and the whole ratio will change. If we abide to retain the shorter wave length in the nominator and the longer wave length in the denominator so the log ratio will increase as the depth increase. This ratio will compensate for the implicitly for variable bottom type (Stumpf et al. 2003), but changes in depth affect the high absorption band more. As a result, the effect of change in ratio because of depth is much greater than that caused by change in bottom reflectance. Generally,

(Stumpf et al. 2003) demonstrated that their non-linear inversion model is more robust and accurate than the conventional log-linear inversion model for relatively deep areas. This is why we will utilise this method with WorldView-2 imagery to examine the role of the new bands in bathymetry.

Blue light (450-510 nm) can penetrate clear water down to 30 m depth, and thus serves as the optimum spectral band from which to extract depth information (Su et al. 2008). WorldView-2 provides a new band; costal blue (400-450 nm), with higher capability of penetrating water (Globe 2009). Also, the yellow band (585-625 nm) will be examined as the longer wavelengths attenuate rapidly in water.

The main assumption for both aforementioned models is based on the assumption that water optical properties are spatially homogeneous, which results in uniformity in water quality over the area of study. In addition, both models assume that the ratio of bottom reflectances is the same for different types of bottoms in the same scene. In general, high water clarity and uniform bottom types are two vital conditions, that must be met for reliable depth retrieval from optical multispectral imagery (Su et al. 2008). In this research the relative depths of part of the water way of the Suez Canal and the over polluted Temsah Lake will be derived from the WorldView-2 imagery, using the non-linear bathymetric inversion model derived by Stumpf.

5.4.2 Data description

Lake Temsah has a nearly triangular shape with elongated sides extending East-West. The lake is small and shallow. It has a surface area of about 8 square kilometers with an average depth of only 11 meters and containing about 90 million cubic meters of water. The lake is surrounded by industrial workshops for shipyards, domestic areas, recreational beaches and agricultural lands.

The Suez Canal pathway is deep, about 24 m depth, but narrows about 300-360 m wide at water level. Figure 5-13 illustrates a false color image for the area of study.

Figure 5-13 Temsah Lake and Canal Suez water way

Unlike the Canal water way, Temsah Lake receives a great deal of untreated domestic and industrial waste discharges and agricultural drainage return flows. Consequently, the lake and its beaches exhibit serious water quality problems in many locations. Moreover, the substantial

amounts of sediment loads, which enter the lake, produce higher accumulation rates and seriously obstruct lake transportation (Donia 2011).

A water quality index, WQI, is a mathematical way of summarizing multiple properties into a single value. This index values are ranging between 0 and 100, with higher numbers indicating lower quality water. (Donia 2011), introduced one of the standers WQI chart for the Temsah Lake and it used in this study to demonstrate the differences in water quality across this region.

Figure 5-14 A WQI for the Temsah Lake, after (Donia 2011)

The figure above shows that almost all the lake water quality is considered very bad except the southern region of the lake that is considered better quality but still bad.

5.4.3 Methodology

A conversion to the radiance then to reflectance followed by relative atmospheric correction will be applied to the master scene as in section 2.3.3. The traditional NDVI ratio will be used to generate a mask to separate the water body of the study area, as in Figure 5-15. C/RE, C/Y, B/Y,

C/G, B/G and G/Y ratios will be used to derive relative bathymetry of the study area using the non-linear bathymetric inversion model derived by Stumpf.

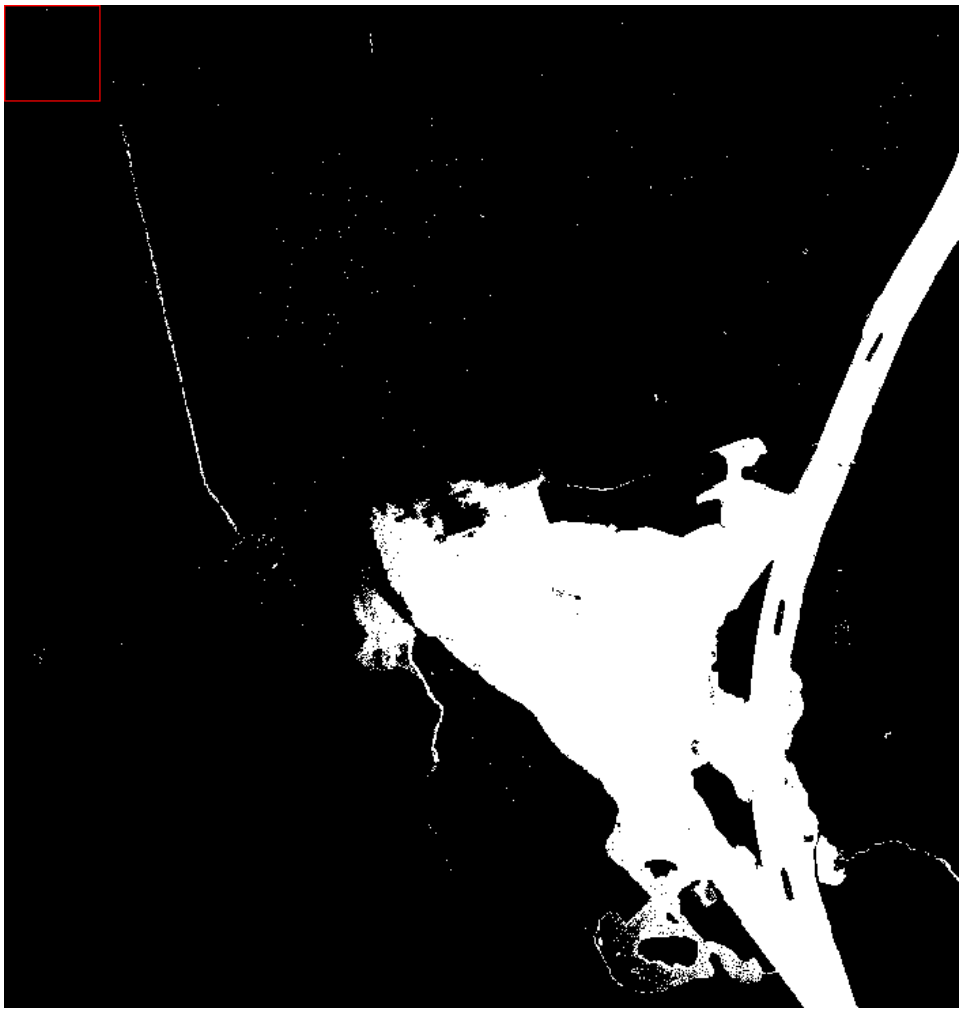

Figure 5-15 Masked area of study

Ideally, atmospheric effects must be removed together with the water column correction in order to achieve radiometric values that are only representative of the sea depth and to make the upwelling response from different bottom types homogeneous (Deidda and Sanna 2012). Moreover, if sun-glint is present, the effect of the sun beams reflecting on the sea surface, it has to be corrected. Knowing that, the upwelling radiance of NIR bands have very low values even

for shallow waters. Subsequently, dark pixel subtract will be applied to account for sun-glint and atmospheric effects by subtracting the Min. value in the NIR bands for a deep water area from the reflectance values for all other visible band.

The available data about the depth of Suez Canal and the Temsah Lake indicates that the dominant depth of the Suez Canal water way is about 24 meters, and an average of 11 meters for the Temsah Lake. No DEM data was available for this site, so the analysis of this result will be depending on the aforementioned information and considering the environmental condition of this area. As discussed before the logarithmic ratio will increase as the depth increase, if we apply this rule on the given results will leads to un realistic results. For instance, considering C/R-E result, if we start with a depth of 24 meters at the blue range (1.033-1.07) will lead to a nominal depth of 46 m at the brown range (1.0885-1.11) which is not true.

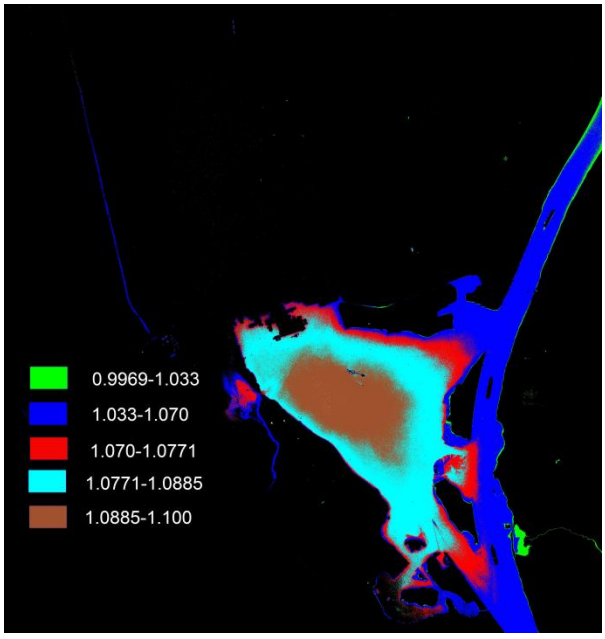

C/RE

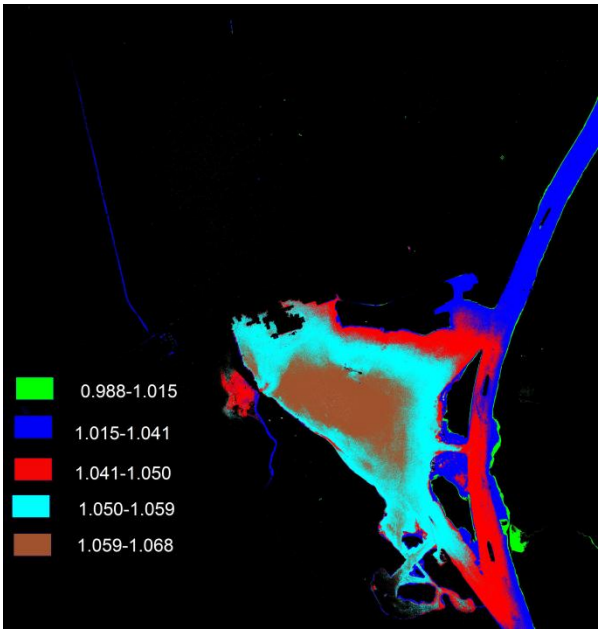

C/Y

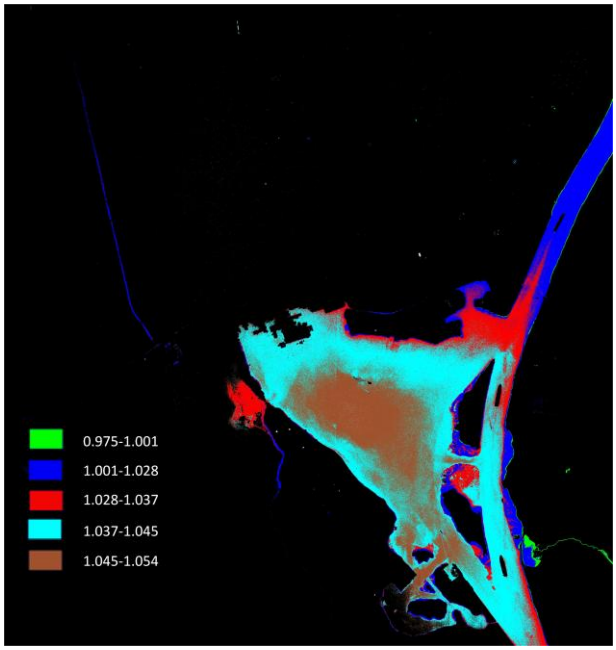

B/Y

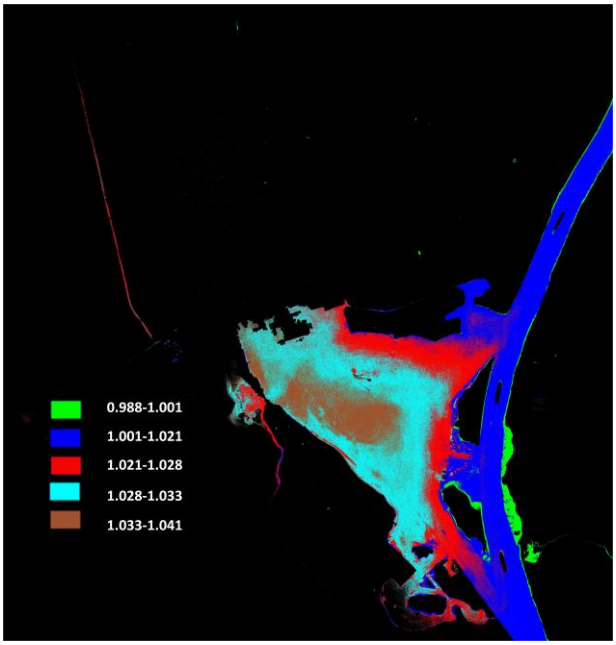

C/G

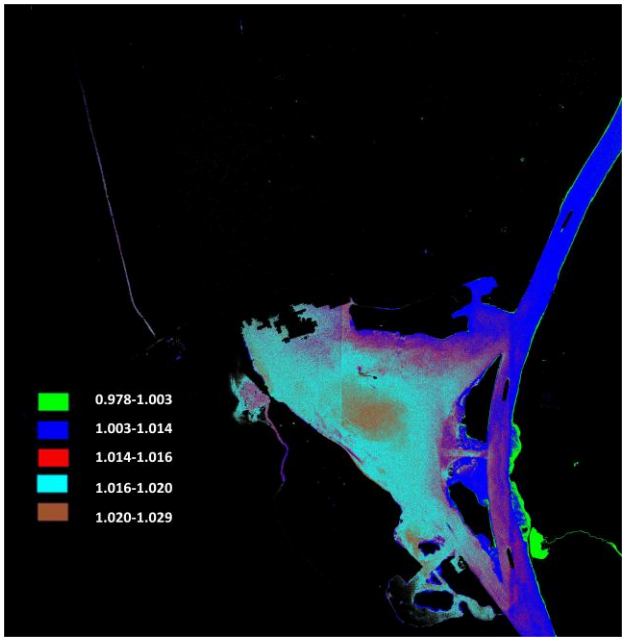

B/G

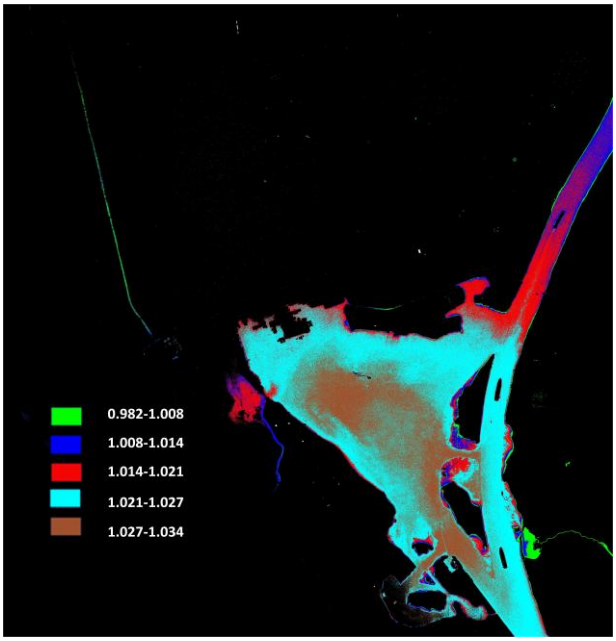

G/Y

Figure 5-16 Relative non-linear bathymetric inversion results

The reason behind this result is the water quality and bottom type condition of the water way of the Suez Canal and the Temsah Lake. The water way of Suez Canal is much better than the one exist in the Temsah Lake as it is always running water has two sources of fresh water coming

from both the Red sea and the Mediterranean Sea. Moreover, the bottom type is homogeneous sand with small gravel, which follows the main assumptions for the bathymetry derivation from satellite imagery; shallow water with homogenous bottom and clear water. But in case of the Temsah Lake results, the bottom of the lake suffer from a lot of sediments coming from the water way plus enormous domestic pollution from the ship yards, the agriculture land and domestic waste water. This pollution affects both water quality and bottom type.

Based on visual comparison, C/RE, C/Y and C/G give better results compared the other ratios, as they were able to separate between two homogeneous ranges (the green and the blue) to depicts both 4-5 meters and 24 meters depth ranges respectively for the water way. Moreover, these ratios give a distinct three ranges for the Temsah Lake (red, cyan and brown) all of them have an average depth of 11 meters, but with different bottom types; the more the ratio value the more sediments and impurities.

Chapter Six: **Summary, Conclusions, Contributions and Recommendations**

The main objective of this thesis was to introduce an integrated urban classification solution. It was successfully achieved through a number of sub-objectives. In this thesis six main classes were targeted; water, vegetation, asphalt, shadow, buildings and bare soil. Additionally, the extraction of shorelines and the development of algorithms for relative bathymetry were also successfully implemented. A new multi-layer classification algorithm integrated with a novel implementation of the second generation multi-resolution techniques for edge detection to overcome the limitations of solely used pixel-based approach was successfully implemented.

6.1 Summary

First, two multi-temporal high resolution satellite imagery were developed to evaluate the calibration parameters for the WorldView-2 data. This was achieved by applying a multi-layer classification algorithm with fixed thresholds. DN's were converted to top of atmosphere reflectance values. Then a relative atmospheric calibration process was applied to the slave scene using manually selected PIF's. The classification algorithm was applied to the master scene and to the slave scene before and after normalization.

New bands of WV-2 were used to develop new band ratios to extract shadow, asphalt, bare soil and building classes in a pixel-based approach, using a multi-layer classification algorithm, and then was integrated with an edge detection algorithm based on the second generation curvelet transforms to enhance the building class percentage.

A further use of the new bands was extended to extract the shorelines and the relative bathymetry of the waterway of the Suez Canal and the Temsah Lake.

6.2 Conclusions and Contributions

The results of the calibration and relative atmospheric step show very good potentials for the use of the calibration parameters even without applying the relative atmospheric normalization. This was achieved because we have the same area and almost the same time of acquisition of April, 2011. Even better results were achieved after applying the normalization process.

The proposed algorithm for edge detection using curvelet transforms was compared with wavelet transform and canny operator on a high-resolution satellite imagery data, the results were promising and shows an improvement in detection of elongated curves and percentage of bounded objects. The total number of coefficients used to reconstruct the edge map using curvelet transforms was 1894105, representing almost 6% of the total coefficients, while in case of wavelet, the number coefficients was 360000, 100% of the total coefficients. Although Curvelet transforms is promising and efficient for edge detection, there is one drawback which must be addressed in the future, related to the quality of the edge detection and its relation with the pre-processing steps (the high-pass filter to enhance edges). As any edge detector will suffer from a great deal of heterogeneity of the images, especially when using very high resolution imagery, which will be the motivation for more distant investigation in the near future.

The proposed algorithm of integrating building extraction technique, using curvelet, with the pixel-based approach results in significant enhancement for the buildings' class accuracy from 45.8% to 85.4% using the new technique. This technique was applied for many other parts of the large scene, Ismailia city, and the results showed great potentials of using this method in enhancing the percentage of the detected buildings.

A further enhancement for the edge detection technique was introduced using a novel curvelet-canny combined approach for edge detection and was applied on high-resolution satellite

imagery data, and repeated using the traditional canny operator, the results were promising. The curvelet-canny approach gives an improved delineation to edges when compared to Canny. The proposed method was able to detect longer edges and generate more closed objects. This method can be used as an alternative for the segmentation process, as it gives a closed boundary for almost all main features in the input image, in an object-based classification approach.

Regarding the relative bathymetry and based on visual comparison, C/RE, C/Y and C/G give better results compared the other ratios, as they were able to separate between two homogeneous ranges (the green and the blue) to depict both 4-5 meters and 24 meters depth ranges respectively for the water way. Moreover, these ratios give a distinct three ranges for the Temsah Lake (red, cyan and brown) all of them have an average depth of 11 m, but with different bottom types; the more the ratio value the more sediments and impurities.

The main contribution of this research is the establishment of an integrated framework for the classification of land use and land cover for urban areas. These contributions can be summarized as follows:

- The implementation of the second-generation curvelet transform (DCTG2) as an edge detector for very high-resolution satellite imagery.
- The development of a detailed comparison between traditional edge detection techniques (Canny and wavelet transformation) against the second-generation curvelet transformation (DCTG2) regarding coastlines, and building extraction.
- The development of a novel approach integrating both canny and curvelet transforms for better edge detection results.

- Validating the improvement in classification accuracy attributable to the new spectral bands versus the traditional VNIR bands used for a broad range of land cover types.
- Determining the predictive role of each of the new spectral bands for each land cover.
- The development of optimal methodology for incorporating spatial and spectral approaches to enhance the classification.
- The development of best band ratio to be used for extracting building, shadow, asphalt, and bare soil in the scope of the new 4-bands.
- Utilizing the new bands, C-B and Y, in relative water depth estimation.
- Full assessment of WorldView2 for local urban monitoring using the full eight bands.

6.3 Recommendations

The recommendation to extend this research thesis is mostly related to the integration with a GIS data base to introduce continuously updated maps for urban areas. Moreover, ground truth regarding vegetation types, water depths, pollution and environmental parameters are essential to produce complete maps containing absolute depths and crops types. Additionally, it is crucial to apply these proposed techniques to different data images from different dates and areas.

The following list contains some of the interesting research topics that are recommended for future work:

- Continuous monitoring of isolated urban areas.
- Detection of underwater object for shallow water areas.
- Integrating the proposed techniques with other sensors such as LiDAR or aerial photogrammetry for the generation of ortho-photos and digital elevation model generation on large scale.

References

Aytekin, O., I. Ulusoy, A. Erener and H. S. B. Duzgun (2009). Automatic and unsupervised building extraction in complex urban environments from multi spectral satellite imagery. Recent Advances in Space Technologies, 2009. RAST '09. 4th International Conference on.

Baumgardner, M. F., E. R. Stoner, L. F. Silva and L. L. Biehl (1985). Reflectance properties of soils. Advances of Agronomy. N. Brady. New York, Academic Press**:** pp 1-44.

Bhaskaran, S., S. Paramananda and M. Ramnarayan (2010). "Per-pixel and object-oriented classification methods for mapping urban features using Ikonos satellite data." Applied Geography **30**(4): 650-665.

Braun, C., T. H. Kolbe, F. Lang, W. Schickler, A. B. Cremers, W. F¨orstner and L. Pl¨umer (1995). "Models for photogrammetric building reconstruction." Comput. & Graphics **19**(1): 109-118.

Candes, E., L. Demanet, D. Donoho and L. X. Ying (2006). "Fast discrete curvelet transforms." Multiscale Modeling & Simulation **5**(3): 861-899.

Candes, E. J. and D. L. Donoho (2004). "New tight frames of curvelets and optimal representations of objects with piecewise C-2 singularities." Communications on Pure and Applied Mathematics **57**(2): 219-266.

Candes, E. J. and D. L. Donoho (2005). "Continuous Curvelet Transform - I. Resolution of the wavefront set." Applied and Computational Harmonic Analysis **19**(2): 162-197.

Canny, J. (1986). "A Computational Approach to Edge Detection." Pattern Analysis and Machine Intelligence, IEEE Transactions on **PAMI-8**(6): 679-698.

CCRS. (2012). "Fundamentals of Remote Sensing." Retrieved June, 4th, 2012, from http://www.nrcan.gc.ca/earth-sciences/geography-boundary/remote-sensing/11691.

Clark, R. N. (1999). Spectroscopy of Rocks and Minerals, and Principles of Spectroscopy. Manual of Remote Sensing. A. N. Rencz. New York., John Wiley and Sons. **Volume 3:** p 3- 58.

Colwell, J. E. (1973). Bidirectional spectral reflectance of grass canopies for determination of above ground standing biomass, University of Michigan. **PhD Thesis**.

Condit, H. R. (1970). "The spectral reflectance of American soils." Photogrammetric Engineering and Remote Sensing **36**: 955-966.

Congalton, R. G. (1991). "A Review of Assessing The Accuracy of Classifications of Remotely Sensed Data." Remote Sensing of Environment **37**(1): 35-46.

Cu, P. V., N. T. T. Hang and N. P. Dong (2009). Comparison of Pixel Based and Object Oriented Classifications in Land Cover Mapping in the Red River Delta – Example of Duy Tien District, Ha Nam Province, Vietnam. 7th FIG Regional Conference. S. D. S. P. L. G. a. t. E. n. B. t. Capacity and Hanoi Vietnam**:** 19-22.

Daryaei, J. (2003). Digital Change Detection Using Multi-scale Wavelet Transformation & Neural Network. Enschede, The Netherlands, ITC. **Master**.

Deidda, M. and G. Sanna (2012). "Pre-processing of high resolution satellite images for sea bottom classification." Italian Journal of Remote Sensing-Rivista Italiana Di Telerilevamento **44**(1): 83-95.

Donia, N. (2011). "Water quality management of lake Temsah, Egypt using geographical information system (GIS)." Iinternational Journal of Environmintal Science and Engineering (IJESE) **2**: 1-8.

Donoho, D. L. and M. R. Duncan (2000). Digital curvelet transform: Strategy, implementation and experiments. Wavelet Applications Vii. H. H. Szu, M. Vetterli, W. J. Campbell and J. R. Buss. **4056:** 12-30.

El Hajj, M., A. Bégué, B. Lafrance, O. Hagolle, G. Dedieu and M. Rumeau (2008). "Relative Radiometric Normalization and Atmospheric Correction of a SPOT 5 Time Series." Sensors **8**(4): 2774-2791.

Elhabiby, M., A. Elsharkawy and N. El-Sheimy (2012). "Second Generation Curvelet Transforms Vs Wavelet transforms and Canny Edge Detector for Edge Detection from WorldView-2 data." International Journal of Computer Science & Engineering Survey (IJCSES) **Vol.3**(No.4): 13.

Elhabiby, M., A. S. Elsharkawy and N. El-Sheimy (2012). Curvelet transform for water bodies extraction from high resolution satellite images. the 8th ICEENG Conference, Cairo, Egypt.

Elsharkawy, A., M. Elhabiby and N. El-Sheimy (2011). A modified parallelepiped-like method for supervised classification for high resolution satellite imagery CGU Annual Scientific Meeting. Banff, Calgary**:** 4.

Elsharkawy, A., M. Elhabiby and N. El-Sheimy (2011). "Second Generation Curvelet Transform for Building Extraction from High Resolution Satellite Imagery." GEOMATICA **65**(4): 387-399.

Elsharkawy, A., M. Elhabiby and N. El-Sheimy (2012). "Assessment of Relative Atmospheric Normalization for Multi-temporal WorldView-2 Data." International Refereed Journal of Engineering and Science (IRJES) **vol. 1**(2): 1-10.

Elsharkawy, A., M. Elhabiby and N. El-Sheimy (2012). Iprovement in The Detection of Land Cover Classes Using The WorldView-2 Imagery ASPRS, Sacremento, CA.

Elsharkawy, A., M. Elhabiby and N. El-Sheimy (2012). New Combined Pixel/Object-Based Technique For Efficient Urban Classification Using WorldView-2 Data. XXII International Society for Photogrammetry & Remote Sensing Congress, VII/4

Elsharkawy, A., M. Elhabiby and N. El-Sheimy (2012). Quality Control on the Radiometric Calibration of the WorldView-2 Data. Global Geospatial Conference 2012, Québec City, Canada.

Franklin, S. E. and B. A. Wilson (1991). "Spatial And Spectral Classification of Remote-Sensing Imagery." Computers & Geosciences **Vol. 17, No. 8,**: 1151-1172.

Freund, J. E. (1992). Mathematical Statistics. New Jersey, Prentice Hall.

Geback, T. and P. Koumoutsakos (2009). "Edge detection in microscopy images using curvelets." BMC Bioinformatics **10**(1): 75.

Globe, D. (2009) "the Benefits of the 8 Spectral Bands of WorldView-2." White Paper, 12.

Globe, D. (2009). DigitalGlobe Core Imagery Products Guide. D. Globe.

Gonzalez, R. C. and R. E. Woods (1992). Digital Image Processing, Addison-Wesley Longman Publishing Co., Inc.

Gonzalez, R. C. and R. E. Woods (2002). Digital Image Processing, Prentice Hall.

Grigillo, D. and M. K. Fras (2011). Classification Based Building Detection From GeoEye-1 Images. JURSE 2011 - Joint Urban Remote Sensing Event. S. U, G. P, J. C and M. D. Munich, Germany.

Guha, T. and Q. M. J. Wu (2010). Curvelet Based Feature Extraction. Face Recognition. M. Oravec, InTech, Available from: http://www.intechopen.com/articles/show/title/curvelet-based-feature-extraction**:** 35-46.

Herold, M., M. Gardner, B. Hadley and D. Roberts (2002). "The Spectral Dimension in Urban Land Cover Mapping From High Resolution Optical Remote Sensing Data." The 3rd Symposium on Remote Sensing of Urban Areas: 8.

Herold, M., M. E. Gardner and D. A. Roberts (2003). "Spectral resolution requirements for mapping urban areas." Ieee Transactions on Geoscience and Remote Sensing **41**(9): 1907-1919.

Hoffer, A. M. (1978). Biological and physical considerations in applying computer-aided analysis techniques to remote sensor data, in Remote Sensing, McGraw-Hili Book Company.

Irons, J. R., R. A. Weismiller and G. W. Petersen (1989). Soil reflectance. Theory and Applications of Optical Remote Sensing. G. Asrar. New York, Wiley**:** pp 66-106.

Jensen, J. R. (1994). Introductory digital image processing : a remote sensing perspective, Prentice Hall.

Jensen, J. R. (2007). Remote sensing of the environment: An earth resource perspective. Upper

Saddle River,NJ, Prentice Hall.

Jordan, C. F. (1969). "Derivation of leaf area index from quality of light on the forest floor." Ecology **50**: 663-666.

Kauth, R. J. and G. S. Thomas (1976). A graphic description of the spectral-temporal development of agricultural crops as seen by Landsat. West Lafayette, IN, Purdue University.

Kavzoglu, T. and P. M. Mather (2000). The Use of Feature Selection Techniques in the Context of Artificial Neural Networks. 26th Annual Conference of the Remote Sensing Society, Leicester, UK.

Lillesand, T. M. and R. W. kiefer (2001). Remote Sensing and Image Interpretation, John Wiley and Sons, Inc.

Liu, J. G. and P. J. Mason (2009). Essential Image Processing and GIS for Remote Sensing. Imperial College London, UK, John Wiley & Sons Ltd.

Livens, S., P. Scheunders, G. van de Wouwer and D. Van Dyck (1997). Wavelets for texture analysis, an overview. Image Processing and Its Applications, 1997., Sixth International Conference on.

Lyzenga, D. R. (1978). "Passive remote sensing techniques for mapping water depth and bottom features." Aplied Optics **Vol. 17**(No. 3): 5.

Lyzenga, D. R. (1981). "Remote sensing of bottom reflectance and water attenuation parameters in shallow water using aircraft and Landsat data." International Journal of Remote Sensing **2**(1): 71-82.

Ma, J. and G. Plonka (2009). "Computing with Curvelets: From Image Processing to Turbulent Flows." Computing in Science and Engg. **11**(2): 72-80.

Mallat, S. G. (1989). "A theory for multiresolution signal decomposition: the wavelet representation." Pattern Analysis and Machine Intelligence, IEEE Transactions on **11**(7): 674-693.

Marchisio, G., F. Pacifici and C. Padwick (2010). On the relative predictive value of the new spectral bands in the WorldView-2 sensor. Geoscience and Remote Sensing Symposium (IGARSS), 2010 IEEE International.

Matsuyama, T., V. Shang and S. Hwang (1990). Sigma: A Knowledge-Based Aerial Image Understanding System, Perseus Publishing

Mayer, H. (1999). "Automatic object extraction from aerial imagery\—a survey focusing on buildings." Comput. Vis. Image Underst **74**(2): 1077-3142.

Meer, F. v. d. (2001). Imaging spectrometry : basic principles and prospective applications, Kluwer Academic Publishers,.

Myint, S. W. (2001). "A Robust Texture Analysis and Classification Approach for Urban Land-Use and Land-Cover Feature Discrimination." Geocarto International **16**(4): 29 - 40.

Nalepka, R. F., C. E. Colwell and D. P. Rice (1977). Forecasts of winter wheat yield and production using LANDSAT data, Research Institute of Michigan. **114800-38-F**.

Nikolakopoulos, K. G. (2008). "Comparison of nine fusion techniques for very high resolution data." Photogrammetric Engineering and Remote Sensing **74**(5): 647-659.

Observation, T. Y. C. f. E. (2010). "Converting Digital Numbers to Top of Atmosphere (ToA) Reflectance." from http://www.yale.edu/ceo.

Ouma, Y. O., R. Tateishi and J. T. Sri-Sumantyo (2010). "Urban features recognition and extraction from very-high resolution multi-spectral satellite imagery: a micro–macro texture determination and integration framework." IET Image Processing **4**(4): 235.

Pedroni, L. (2003). "Improved classification of Landsat Thematic Mapper data using modified prior probabilities in large and complex landscapes." International Journal of Remote Sensing **24**(1): 91-113.

Richards, J. A. and X. Jia (2006). Remote Sensing Digital Image Analysis, Springer.

Rouse, J. W., R. H. Haas, J. A. Schell, D. W. Deering and J. C. Harlan (1974). Monitoring the vernal advancement of natural vegetation. Greenbelt, MD, NASA Goddard Space Flight Cente.

Schowengerdt, R. A. (2006). Models and Methods for Image Processing. Burlington, MA, USA, Academic Press.

Shafri, H., M. Salleh and A. Ghiyamat (2006). "Hyperspectral Remote Sensing of Vegetation Using Red Edge Position Techniques." American Journal of Applied Sciences **3(6)**: 1864-1871.

Sharma, K. M. S. and A. Sarkar (1998). "Modified contextual classification technique for remote sensing data." Photogrammetric Engineering and Remote Sensing **64**(4): 273-280.

Singh, R. P. and S. A (1994). "Spectral reflectance properties of different types of soil surfaces." ISPRS Journal of Photogrammetry and Remote Sensing **49**: 30-34.

Solomon, C. and T. Breckon (2011). Fundamentals of Digital Image Processing, John Wiley & Sons, Ltd.

Stoner, E. R. and M. F. Baumgardner (1981). "Characteristic variations in reflectance of surface soils." Soil Science Society of America Journal **45**: 1161 -1165.

Stumpf, R. P., K. Holderied and M. Sinclair (2003). "Determination of water depth with high-resolution satellite imagery over variable bottom types." Limnology and Oceanography **48**(1): 547-556.

Su, H. B., H. X. Liu and W. D. Heyman (2008). "Automated Derivation of Bathymetric Information from Multi-Spectral Satellite Imagery Using a Non-Linear Inversion Model." Marine Geodesy **31**(4): 281-298.

Swayze, G. A., R. N. Clark, A. F. H. Goetz, T. G. Chrien and N. S. Gorelick (2003). "Effects of spectrometer band pass, sampling, and signal-to-noise ratio on spectral identification using the Tetracorder algorithm." J. Geophys. Res. **108**(E9): 5105.

Taubenbock, H., T. Esch, M. Wurm, A. Roth and S. Dech (2010). "Object-based feature extraction using high spatial resolution satellite data of urban areas." Journal of Spatial Science **55**(1): 117-132.

Thomas, N., C. Hendrix and R. G. Congalton (2003). "A comparison of urban mapping methods using high-resolution digital imagery." Photogrammetric Engineering and Remote Sensing **69**(9): 963-972.

Tso, B. and P. M. Mather (2009). Pattern Recognition Principles T2 - Classification Methods for Remotely Sensed Data, Second Edition T3. Classification Methods for Remotely Sensed Data, Second Edition, Taylor and Francic. **null**.

Tso, B. and P. M. Mather (2009). Texture Quantization. Classification Methods for Remotely Sensed Data, Second Edition, CRC Press. **null**.

Ünsalan, C. and K. L. Boyer (2011). Multispectral Satellite Image Understanding, Springer.

Updike, T. and C. Comp (2010). Radiometric Use of WorldView-2 Imagery. D. Globe.

Wei, Y., Z. Zhao and J. Song (2004). Urban building extraction from high-resolution satellite panchromatic image using clustering and edge detection.

Xiao, M., Y. Jia, Z. He and Y. Chen (2008). Edge Detection of Riverway in Remote Sensing Images Based on Curvelet Transform and GVF Snake. Spatial Accuracy Assessment in Natural Resources and Environmental Sciences. Shanghai, P. R. China, **:** pp. 344-351.

Yan, G. (2003). pixel based and object-oriented image analysis for coal fire research. Enchede, The Netherlands, International Institute for Geo-Information Science and Earth Observation. **Master:** 93.

Yanfeng, W., Z. Zhongming and S. Jianghong (2004). Urban building extraction from high-resolution satellite panchromatic image using clustering and edge detection. Geoscience and Remote Sensing Symposium, 2004. IGARSS '04. Proceedings. 2004 IEEE International.

Yiu-ming, C. (2005). "On rival penalization controlled competitive learning for clustering with automatic cluster number selection." Knowledge and Data Engineering, IEEE Transactions on **17**(11): 1583-1588.

Zhenghai, L. and Q. Jianxiong (2009). Study of Technique of Edge Detection Based on Curvelet Transform. Second International Symposium on Computational Intelligence and Design, IEEE computer society.

Appendix A

In this section the calculation of the confusion matrix will be explained using the data in Table 2-4. Table A-1, illustrates the pixel count format of table 2-4, in this table we can see that total number of pixels under consideration is 625186 pixels.

The overall accuracy can be calculated by dividing the summation of the diagonal by the total number of pixels. Table A-1

$$Overall\ accuracy = \frac{summation\ of\ the\ diagonal}{total\ number\ of\ pixels} = \frac{620740}{625186} = 99.2889\%$$

Table A-1 The confusion matrix in table 2-4 in pixel count format

Class	water	vegetation	Bare Soil	Asphalt	Shadows	Red Roof	Buildings	Total
water	282422	0	25	0	169	0	0	282627
vegetation	0	87949	0	8	2	0	0	87960
Bare Soil	0	230	244739	720	3	192	666	246553
Asphalt	0	239	74	2092	82	0	175	2650
Shadows	0	89	123	440	1590	0	24	2269
Red Roof	0	62	221	65	0	405	0	767
Buildings	0	0	787	30	0	0	1543	2360
Total	282432	88570	245978	3355	1846	597	2408	625186

To calculate producer's and user's accuracy the following rules were used

User's accuracy: Corresponds to error of commission (inclusion);

$$User's\ accuracy_{water\ class} = \frac{no.of\ pixels\ of\ the\ diagonal}{total\ number\ of\ row} = \frac{282422}{282627} = 99.927\ \%$$

Producer's accuracy: Corresponds to error of omission (exclusion);

$$Producer's\ accuracy_{water\ class} = \frac{no.of\ pixels\ of\ the\ diagonal}{total\ number\ of\ column} = \frac{282422}{282432} = 99.99\ \%$$

Table A-2 summarizes the producer's and user's accuracies for all classes.

Table A-2 The producer's and user's accuracies associated to the data in table A-1

Class	Commission (Percent)	Omission (Percent)	Commission (Pixels)	Omission (Pixels)	Prod. Acc. (%)	User Acc. (%)	Prod. Acc. (Pixels)	User Acc. (Pixels)
water	0.07	0.00	205/282627	10/282432	100.00	99.93	282422/282432	282422/282627
vegetation	0.01	0.70	11/87960	621/88570	99.30	99.99	87949/88570	87949/87960
Bare Soil	0.74	0.50	1814/246553	1239/245978	99.50	99.26	244739/245978	244739/246553
Asphalt	21.06	37.65	558/2650	1263/3355	62.35	78.94	2092/3355	2092/2650
Shadows	29.93	13.87	679/2269	256/1846	86.13	70.07	1590/1846	1590/2269
Red Roof	47.20	32.16	362/767	192/597	67.84	52.80	405/597	405/767
Buildings	34.62	35.92	817/2360	865/2408	64.08	65.38	1543/2408	1543/2360

Appendix B

IDM file for the master scene

```
Version = "23.2";
generationTime = 2011-04-19T01:12:57.000000Z;
productOrderId = "052487923030_01_P002";
productCatalogId = "2030010075559400";
imageDescriptor = "ORStandard2A";
bandId = "Multi";
panSharpenAlgorithm = "None";
numRows = 5348;
numColumns = 5650;
productLevel = "LV2A";
productType = "Standard";
numberOfLooks = 1;
radiometricLevel = "Corrected";
radiometricEnhancement = "Off";
bitsPerPixel = 16;
compressionType = "None";
BEGIN_GROUP = BAND_C
        ULLon =   32.21541943;
        ULLat =   30.63334663;
        ULHAE =    28.00;
        URLon =   32.33330738;
        URLat =   30.63400453;
        URHAE =    28.00;
        LRLon =   32.33396743;
        LRLat =   30.53751054;
        LRHAE =    28.00;
        LLLon =   32.21619617;
        LLLat =   30.53685515;
        LLHAE =    28.00;
        absCalFactor = 9.295654e-03;
        effectiveBandwidth = 4.730000e-02;
        TDILevel = 24;
END_GROUP = BAND_C
BEGIN_GROUP = BAND_B
        ULLon =   32.21541943;
        ULLat =   30.63334663;
        ULHAE =    28.00;
        URLon =   32.33330738;
        URLat =   30.63400453;
        URHAE =    28.00;
        LRLon =   32.33396743;
```

LRLat = 30.53751054;
LRHAE = 28.00;
LLLon = 32.21619617;
LLLat = 30.53685515;
LLHAE = 28.00;
absCalFactor = 1.783568e-02;
effectiveBandwidth = 5.430000e-02;
TDILevel = 10;
END_GROUP = BAND_B
BEGIN_GROUP = BAND_G
ULLon = 32.21541943;
ULLat = 30.63334663;
ULHAE = 28.00;
URLon = 32.33330738;
URLat = 30.63400453;
URHAE = 28.00;
LRLon = 32.33396743;
LRLat = 30.53751054;
LRHAE = 28.00;
LLLon = 32.21619617;
LLLat = 30.53685515;
LLHAE = 28.00;
absCalFactor = 1.364197e-02;
effectiveBandwidth = 6.300000e-02;
TDILevel = 10;
END_GROUP = BAND_G
BEGIN_GROUP = BAND_Y
ULLon = 32.21541943;
ULLat = 30.63334663;
ULHAE = 28.00;
URLon = 32.33330738;
URLat = 30.63400453;
URHAE = 28.00;
LRLon = 32.33396743;
LRLat = 30.53751054;
LRHAE = 28.00;
LLLon = 32.21619617;
LLLat = 30.53685515;
LLHAE = 28.00;
absCalFactor = 6.810718e-03;
effectiveBandwidth = 3.740000e-02;
TDILevel = 18;
END_GROUP = BAND_Y
BEGIN_GROUP = BAND_R
ULLon = 32.21541943;

ULLat = 30.63334663;
ULHAE = 28.00;
URLon = 32.33330738;
URLat = 30.63400453;
URHAE = 28.00;
LRLon = 32.33396743;
LRLat = 30.53751054;
LRHAE = 28.00;
LLLon = 32.21619617;
LLLat = 30.53685515;
LLHAE = 28.00;
absCalFactor = 1.103623e-02;
effectiveBandwidth = 5.740000e-02;
TDILevel = 10;
END_GROUP = BAND_R
BEGIN_GROUP = BAND_RE
ULLon = 32.21541943;
ULLat = 30.63334663;
ULHAE = 28.00;
URLon = 32.33330738;
URLat = 30.63400453;
URHAE = 28.00;
LRLon = 32.33396743;
LRLat = 30.53751054;
LRHAE = 28.00;
LLLon = 32.21619617;
LLLat = 30.53685515;
LLHAE = 28.00;
absCalFactor = 6.063145e-03;
effectiveBandwidth = 3.930000e-02;
TDILevel = 18;
END_GROUP = BAND_RE
BEGIN_GROUP = BAND_N
ULLon = 32.21541943;
ULLat = 30.63334663;
ULHAE = 28.00;
URLon = 32.33330738;
URLat = 30.63400453;
URHAE = 28.00;
LRLon = 32.33396743;
LRLat = 30.53751054;
LRHAE = 28.00;
LLLon = 32.21619617;
LLLat = 30.53685515;
LLHAE = 28.00;

```
        absCalFactor = 1.224380e-02;
        effectiveBandwidth = 9.890000e-02;
        TDILevel = 10;
END_GROUP = BAND_N
BEGIN_GROUP = BAND_N2
        ULLon =   32.21541943;
        ULLat =   30.63334663;
        ULHAE =    28.00;
        URLon =   32.33330738;
        URLat =   30.63400453;
        URHAE =    28.00;
        LRLon =   32.33396743;
        LRLat =   30.53751054;
        LRHAE =    28.00;
        LLLon =   32.21619617;
        LLLat =   30.53685515;
        LLHAE =    28.00;
        absCalFactor = 9.042234e-03;
        effectiveBandwidth = 9.960000e-02;
        TDILevel = 24;
END_GROUP = BAND_N2
outputFormat = "GeoTIFF";
BEGIN_GROUP = IMAGE_1
        satId = "WV02";
        mode = "FullSwath";
        scanDirection = "Forward";
        CatId = "1030010009920300";
        firstLineTime = 2011-04-16T08:42:36.001090Z;
        avgLineRate = 5000.01;
        exposureDuration = 0.0002;
        minCollectedRowGSD =   2.183;
        maxCollectedRowGSD =   2.189;
        meanCollectedRowGSD =   2.186;
        minCollectedColGSD =   2.433;
        maxCollectedColGSD =   2.433;
        meanCollectedColGSD =   2.433;
        meanCollectedGSD =   2.306;
        rowUncertainty =   36.75;
        colUncertainty =   64.12;
        minSunAz = 138.4;
        maxSunAz = 138.6;
        meanSunAz = 138.5;
        minSunEl =  64.1;
        maxSunEl =  64.2;
        meanSunEl =  64.2;
```

minSatAz = 62.5;
maxSatAz = 63.2;
meanSatAz = 62.9;
minSatEl = 58.7;
maxSatEl = 58.9;
meanSatEl = 58.8;
minInTrackViewAngle = 15.4;
maxInTrackViewAngle = 15.7;
meanInTrackViewAngle = 15.6;
minCrossTrackViewAngle = 23.0;
maxCrossTrackViewAngle = 23.1;
meanCrossTrackViewAngle = 23.0;
minOffNadirViewAngle = 27.6;
maxOffNadirViewAngle = 27.6;
meanOffNadirViewAngle = 27.6;
PNIIRS = 2.8;
cloudCover = 0.000;
resamplingKernel = "CC";
positionKnowledgeSrc = "R";
attitudeKnowledgeSrc = "R";
revNumber = 7965;
END_GROUP = IMAGE_1
BEGIN_GROUP = MAP_PROJECTED_PRODUCT
earliestAcqTime = 2011-04-16T08:42:36.572473Z;
latestAcqTime = 2011-04-16T08:42:36.572473Z;
datumName = "WE";
semiMajorAxis = 6378137.0000;
inverseFlattening = 298.257223563;
datumOffset = (0.000, 0.000, 0.000);
mapProjName = "UTM";
mapProjCode = 1;
mapZone = 36;
mapHemi = "N";
mapProjParam = (0.000000000, 0.000000000, 0.000000000, 0.000000000, 0.000000000, 0.000000000, 0.000000000, 0.000000000, 0.000000000, 0.000000000, 0.000000000, 0.000000000, 0.000000000, 0.000000000);
productUnits = "M";
originX = 424812.99999997;
originY = 3389230.99999930;
orientationAngle = 0.0;
colSpacing = 2.00;
rowSpacing = 2.00;
productGSD = 2.00;
ULX = 424812.99999997;
ULY = 3389230.99999930;

ULH = 28.00;
URX = 436110.99999999;
URY = 3389230.99999931;
URH = 28.00;
LRX = 436110.99999999;
LRY = 3378536.99999929;
LRH = 28.00;
LLX = 424812.99999997;
LLY = 3378536.99999928;
LLH = 28.00;
DEMCorrection = "Base Elevation";
terrainHae = 28.00;
numGCP = 0;
END_GROUP = MAP_PROJECTED_PRODUCT
END;

IDM file for the slave scene:

Version = "23.2";
generationTime = 2011-04-19T01:16:03.000000Z;
productOrderId = "052487923040_01_P001";
productCatalogId = "2030010075559800";
imageDescriptor = "ORStandard2A";
bandId = "MS1";
panSharpenAlgorithm = "None";
numRows = 5349;
numColumns = 5702;
productLevel = "LV2A";
productType = "Standard";
numberOfLooks = 1;
radiometricLevel = "Corrected";
radiometricEnhancement = "Off";
bitsPerPixel = 16;
compressionType = "None";
BEGIN_GROUP = BAND_B
ULLon = 32.21433412;
ULLat = 30.63335813;
ULHAE = 28.00;
URLon = 32.33330725;
URLat = 30.63402258;
URHAE = 28.00;
LRLon = 32.33396743;
LRLat = 30.53751054;
LRHAE = 28.00;
LLLon = 32.21511208;

LLLat = 30.53684862;
LLHAE = 28.00;
absCalFactor = 1.783568e-02;
effectiveBandwidth = 5.430000e-02;
TDILevel = 10;
END_GROUP = BAND_B
BEGIN_GROUP = BAND_G
ULLon = 32.21433412;
ULLat = 30.63335813;
ULHAE = 28.00;
URLon = 32.33330725;
URLat = 30.63402258;
URHAE = 28.00;
LRLon = 32.33396743;
LRLat = 30.53751054;
LRHAE = 28.00;
LLLon = 32.21511208;
LLLat = 30.53684862;
LLHAE = 28.00;
absCalFactor = 1.364197e-02;
effectiveBandwidth = 6.300000e-02;
TDILevel = 10;
END_GROUP = BAND_G
BEGIN_GROUP = BAND_R
ULLon = 32.21433412;
ULLat = 30.63335813;
ULHAE = 28.00;
URLon = 32.33330725;
URLat = 30.63402258;
URHAE = 28.00;
LRLon = 32.33396743;
LRLat = 30.53751054;
LRHAE = 28.00;
LLLon = 32.21511208;
LLLat = 30.53684862;
LLHAE = 28.00;
absCalFactor = 1.103623e-02;
effectiveBandwidth = 5.740000e-02;
TDILevel = 10;
END_GROUP = BAND_R
BEGIN_GROUP = BAND_N
ULLon = 32.21433412;
ULLat = 30.63335813;
ULHAE = 28.00;
URLon = 32.33330725;

```
        URLat =   30.63402258;
        URHAE =    28.00;
        LRLon =   32.33396743;
        LRLat =   30.53751054;
        LRHAE =    28.00;
        LLLon =   32.21511208;
        LLLat =   30.53684862;
        LLHAE =    28.00;
        absCalFactor = 1.224380e-02;
        effectiveBandwidth = 9.890000e-02;
        TDILevel = 10;
END_GROUP = BAND_N
outputFormat = "GeoTIFF";
BEGIN_GROUP = IMAGE_1
        satId = "WV02";
        mode = "FullSwath";
        scanDirection = "Reverse";
        CatId = "103001000A1C9300";
        firstLineTime = 2011-04-16T08:44:19.001008Z;
        avgLineRate = 5000.01;
        exposureDuration = 0.0002;
        minCollectedRowGSD =   2.812;
        maxCollectedRowGSD =   2.870;
        meanCollectedRowGSD =   2.836;
        minCollectedColGSD =   2.480;
        maxCollectedColGSD =   2.505;
        meanCollectedColGSD =   2.490;
        meanCollectedGSD =   2.658;
        rowUncertainty =   81.53;
        colUncertainty =   56.70;
        minSunAz = 139.2;
        maxSunAz = 139.4;
        meanSunAz = 139.3;
        minSunEl =  64.4;
        maxSunEl =  64.5;
        meanSunEl =  64.4;
        minSatAz = 155.4;
        maxSatAz = 155.8;
        meanSatAz = 155.6;
        minSatEl =  50.7;
        maxSatEl =  51.0;
        meanSatEl =  50.9;
        minInTrackViewAngle = -28.5;
        maxInTrackViewAngle = -27.7;
        meanInTrackViewAngle = -28.0;
```

minCrossTrackViewAngle = 20.2;
maxCrossTrackViewAngle = 20.3;
meanCrossTrackViewAngle = 20.2;
minOffNadirViewAngle = 34.1;
maxOffNadirViewAngle = 34.1;
meanOffNadirViewAngle = 34.1;
PNIIRS = 2.6;
cloudCover = 0.000;
resamplingKernel = "MTF";
positionKnowledgeSrc = "R";
attitudeKnowledgeSrc = "R";
revNumber = 7965;
END_GROUP = IMAGE_1
BEGIN_GROUP = MAP_PROJECTED_PRODUCT
earliestAcqTime = 2011-04-16T08:44:20.327011Z;
latestAcqTime = 2011-04-16T08:44:20.327011Z;
datumName = "WE";
semiMajorAxis = 6378137.0000;
inverseFlattening = 298.257223563;
datumOffset = (0.000, 0.000, 0.000);
mapProjName = "UTM";
mapProjCode = 1;
mapZone = 36;
mapHemi = "N";
mapProjParam = (0.000000000, 0.000000000, 0.000000000, 0.000000000, 0.000000000, 0.000000000, 0.000000000, 0.000000000, 0.000000000, 0.000000000, 0.000000000, 0.000000000, 0.000000000, 0.000000000, 0.000000000, 0.000000000);
productUnits = "M";
originX = 424708.99999997;
originY = 3389232.99999930;
orientationAngle = 0.0;
colSpacing = 2.00;
rowSpacing = 2.00;
productGSD = 2.00;
ULX = 424708.99999997;
ULY = 3389232.99999930;
ULH = 28.00;
URX = 436110.99999999;
URY = 3389232.99999930;
URH = 28.00;
LRX = 436110.99999999;
LRY = 3378536.99999929;
LRH = 28.00;
LLX = 424708.99999997;
LLY = 3378536.99999928;

```
        LLH =      28.00;
        DEMCorrection = "Base Elevation";
        terrainHae =   28.00;
        numGCP = 0;
END_GROUP = MAP_PROJECTED_PRODUCT
END;
```